NASA/CR-2006-214283

Finite and Boundary Element Modeling of the NASA Langley Aluminum Testbed Cylinder (ATC)

Ferdinand W. Grosveld
Lockheed Martin Engineering and Sciences Company, Hampton, Virginia

March 2006

The NASA STI Program Office . . . in Profile

Since its founding, NASA has been dedicated to the advancement of aeronautics and space science. The NASA Scientific and Technical Information (STI) Program Office plays a key part in helping NASA maintain this important role.

The NASA STI Program Office is operated by Langley Research Center, the lead center for NASA's scientific and technical information. The NASA STI Program Office provides access to the NASA STI Database, the largest collection of aeronautical and space science STI in the world. The Program Office is also NASA's institutional mechanism for disseminating the results of its research and development activities. These results are published by NASA in the NASA STI Report Series, which includes the following report types:

- TECHNICAL PUBLICATION. Reports of completed research or a major significant phase of research that present the results of NASA programs and include extensive data or theoretical analysis. Includes compilations of significant scientific and technical data and information deemed to be of continuing reference value. NASA counterpart of peer-reviewed formal professional papers, but having less stringent limitations on manuscript length and extent of graphic presentations.

- TECHNICAL MEMORANDUM. Scientific and technical findings that are preliminary or of specialized interest, e.g., quick release reports, working papers, and bibliographies that contain minimal annotation. Does not contain extensive analysis.

- CONTRACTOR REPORT. Scientific and technical findings by NASA-sponsored contractors and grantees.

- CONFERENCE PUBLICATION. Collected papers from scientific and technical conferences, symposia, seminars, or other meetings sponsored or co-sponsored by NASA.

- SPECIAL PUBLICATION. Scientific, technical, or historical information from NASA programs, projects, and missions, often concerned with subjects having substantial public interest.

- TECHNICAL TRANSLATION. English-language translations of foreign scientific and technical material pertinent to NASA's mission.

Specialized services that complement the STI Program Office's diverse offerings include creating custom thesauri, building customized databases, organizing and publishing research results ... even providing videos.

For more information about the NASA STI Program Office, see the following:

- Access the NASA STI Program Home Page at ***http://www.sti.nasa.gov***

- E-mail your question via the Internet to help@sti.nasa.gov

- Fax your question to the NASA STI Help Desk at (301) 621-0134

- Phone the NASA STI Help Desk at (301) 621-0390

- Write to:
  NASA STI Help Desk
  NASA Center for AeroSpace Information
  7121 Standard Drive
  Hanover, MD 21076-1320

NASA/CR-2006-214283

Finite and Boundary Element Modeling of the NASA Langley Aluminum Testbed Cylinder (ATC)

Ferdinand W. Grosveld
Lockheed Martin Engineering and Sciences Company, Hampton, Virginia

National Aeronautics and
Space Administration

Langley Research Center
Hampton, Virginia 23681-2199

Prepared for Langley Research Center
under Contract NAS1-00135B

March 2006

Available from:

NASA Center for AeroSpace Information (CASI)
7121 Standard Drive
Hanover, MD 21076-1320
(301) 621-0390

National Technical Information Service (NTIS)
5285 Port Royal Road
Springfield, VA 22161-2171
(703) 605-6000

TABLE OF CONTENTS

LIST OF TABLES

LIST OF FIGURES

ABSTRACT

The NASA Langley Aluminum Testbed Cylinder (ATC) was designed to serve as a universal structure for evaluating structural acoustic codes, modeling techniques and optimization methods used in the prediction of aircraft interior noise. Finite element models were developed for the components of the ATC based on the geometric, structural and material properties of the physical test structure. Numerically predicted modal frequencies for the longitudinal stringer, ring frame and dome component models, and six assembled ATC arrangements (Configurations I-VI) were compared with experimental modal survey data. The finite element models were updated and enhanced, using physical parameters, to increase correlation with the measured modal data. Excellent agreement, within an average 1.5% to 2.9%, was obtained between the predicted and measured modal frequencies of the stringer, frame and dome components. The predictions for the modal frequencies of the assembled component Configurations I through V were within an average 2.9% and 9.1%. Finite element modal analyses were performed for comparison with 3 psi (pounds/inch^2) and 6 psi internal pressurization conditions in Configuration VI. The modal frequencies were predicted by applying differential stiffness to the elements with pressure loading and creating reduced matrices for beam elements with offsets inside external superelements. The average disagreement between the measured and predicted differences for the 0 psi and 6 psi internal pressure conditions was less than 0.5%. Similar agreement was obtained between the 0 psi and 3 psi measured and predicted internal pressure conditions. Acoustic cylinder modes for the interior of the ATC were calculated with an acoustic finite element model and compared with measured results. Experimental frequencies correlated well with thirty-four predicted acoustic modal frequencies. Frequency transfer functions between a unit force on the structure and the acoustic response inside the ATC cylinder were measured and predicted using a boundary element model of the cylinder. Reasonable agreement was obtained between the predicted and measured acoustic responses at low-order acoustic or structural modal frequencies. At higher frequencies the modal densities increase, the predicted and measured modal frequencies compare less favorably, and predicting the measured structural-acoustic response becomes increasingly more difficult.

1 INTRODUCTION

The NASA Langley Research Center has agency responsibility for aircraft interior noise control in both subsonic and supersonic aircraft. Active control of noise and vibration has been shown to be a viable noise control technology to meet objectives in a lightweight, cost-effective manner. Active noise control technology has been successfully demonstrated using loudspeakers to achieve overall noise reduction inside an aircraft cabin.[1] Alternative methods have been studied where appreciable sound attenuation was achieved across double wall structures by placing acoustic control sources in the space between the walls (loudspeakers between the fuselage and trim panel, for example).[2] In other work, active structural acoustic control was investigated where force inputs were applied directly to the primary aircraft structure, thus eliminating the need to place acoustic control sources in the cabin. Such control forces might be produced by piezoelectric patches bonded to the structure. This approach has the potential to produce a global interior noise reduction with a limited number of control actuators.[3,4] Additional reductions in the number of control actuators may be achieved by grouping the actuators to reduce control spillover into the structure.[5,6] Amplitude and phase of the control forces can be optimized to maximize the noise reduction.[7] In recent studies, the active structural acoustic control characteristics of a double wall cylinder with ring stiffeners were evaluated numerically using finite element and boundary element techniques.[7-10] In an experimental analysis, the effectiveness of optimized actuator/sensor architectures and controller algorithms was determined for the active control of harmonic interior noise.[11] A combinatorial optimization technique was employed to select the optimum transducer arrays. The feasibility of reducing the interior noise levels of an aircraft passenger cabin through an optimization of the composite lay-up of the fuselage was demonstrated in Reference 12. In another study, a computational scheme, using finite element and boundary element methods, was developed to minimize noise transmission into an aircraft fuselage by optimizing selected structural parameters.[13]

Many of these and similar studies require accurate structural-acoustic prediction methods and experimental validation of component structures up to complete fuselage configurations. The Structural Acoustics Branch at NASA Langley Research Center initiated the design and construction of an Aluminum Testbed Cylinder (ATC) to

create a universal structure for evaluating structural acoustic codes, modeling techniques and optimization methods used in the prediction of aircraft interior noise. The purpose of the current program is to develop high fidelity, manageable ATC numerical models based on accurate geometric, structural and material properties of the participating components. The component structures, up to complete fuselage configurations, require experimental validation performed on the physical model. Recent numerical modeling and vibro-acoustic modal testing pursued at NASA Langley is listed in References 14-22. This report discusses the finite element model development and validation of three isolated components and six assembled configurations through comparison with modal response data from experimental modal surveys. Updated and refined finite element models that exhibit increased correlation with the measured modal data are discussed. An acoustic boundary element model is developed to compute the interior acoustic response for the fully assembled ATC when excited by a unit force on the structure. The results are compared with measurements.

2 ALUMINUM TESTBED CYLINDER

The Aluminum Testbed Cylinder (ATC) was designed as a simplified model of an aircraft fuselage structure. Six configurations of component assemblies were considered (Table 1). The bare frame substructure of Configuration I includes longitudinal stringers, ring frames and end rings (Figure 1). The cylindrical section of the testbed with the longitudinal stringers is 144 inches long with a diameter of 48 inches. Nine aluminum ring frames are evenly spaced over the length of the cylinder and twenty-four stringers are equally distributed around the circumference. The aluminum end rings have a 2-inch by 1.5-inch cross-section. A photograph of the Configuration I assembly is shown in Figure 2. Configuration II (Figure 3) adds a plate to each end of the bare frame cylinder section (Table 1). Each end plate consists of a two-inch-thick particleboard with a half-inch-thick piece of plywood attached. Configuration III in Table 1 constitutes the bare frame, without the end plates, but covered with a 0.040-inch thick aluminum skin (Figure 4). The skin is assembled from four 144-inch-long overlapping aluminum sheets. Configuration IV includes the bare frame, the skin and the end plates. One-quarter inch thick fiberglass-reinforced epoxy composite domes, featuring pressure release devices and access plates, are installed in Configuration V (Figure 5) to facilitate pressurization up to 7 psi (pounds/inch^2). The domes also enable potential wind tunnel testing. A drawing of Configuration V is presented in Figure 6. Pressure differential loadings are applied to the ATC in Configuration VI.

3 EXPERIMENTAL MODAL ANALYSIS

3.1 Component Surveys

Modal survey measurements were conducted on an isolated longitudinal stringer, a ring frame and a pressure dome. Each component was suspended from bungee chords to simulate free-free conditions. The modal parameters were obtained from a modal analysis of the frequency response functions between a hammer impact force and the output from reference accelerometers. Several impact locations were used to capture the modal properties for the first ten to sixteen modes. The polyreference curevefitter in the Spectral Dynamics STAR software was used to determine the modal properties from the frequency response data. The modal results were used to validate the finite element models of the components.

3.2 Configuration Surveys

Experimental modal surveys were performed[16,21,22] by the NASA Langley Structural Dynamics Branch on the six ATC configurations listed in Table 1. Bungee chords were used to simulate free-free boundary conditions for the first three ATC configurations. The ATC was supported on four airbag isolators for the other configurations to accommodate the increased weight of the test structure and provide more stability to the setup. Four shakers were used simultaneously for all tests. The shaker locations for Configuration II are shown in Figure 7. One shaker, at

location 1 on the starboard side, was used to apply a tangential side force at a 45-degree angle, primarily exciting the torsional and axial modes of the structure. The other three shakers (locations 2-4) excited the cylinder in the radial direction to force participation of the bending and shell modes of the structure. Figure 8 shows the setup for the modal tests on the fully assembled ATC (Configuration V). Figure 9 shows one of the shakers used in the measurements. Another shaker is located in the background. The remaining two shakers in the experiment are on the opposite side of the cylinder. Figure 10 shows a close-up of an impedance head attached to the cylinder skin. Continuous random signals were used as input to the four shakers. A data acquisition system (DAS) was employed to record two hundred twenty-eight response measurements and four signals of the excitation inputs. The force and acceleration time histories were recorded on several analog-to-digital converter throughput disks in the DAS, where anti-aliasing and autoranging capabilities ensured high-quality measurements. The frequency response functions featured 12,800 lines over a frequency range from 0 to 1000 Hz, resulting in a resolution of 0.078 Hz. The functions were generated using seventy-five ensemble averages. Mode Indicator Functions (MIF) were calculated from the frequency response functions to provide an estimate of the natural vibration frequencies of the structure. The Eigensystem Realization Algorithm (ERA) was used to identify the modal parameters (natural frequencies, damping factors, and mode shapes) for each test configuration. [16,21,22] Damping factors were obtained for all modes.

4 COMPONENT FINITE ELEMENT MODELS

Geometry and finite element models, including material properties, element properties and boundary conditions were developed and pre-processed in MSC/PATRAN. The ATC finite element models were assembled from component models of the longitudinal stringers, ring frames, end rings, end plates, shell, and domes (including end cap rings and access plates). The finite element models were equivalenced to remove redundant nodes. A structural damping factor of 0.01 was employed for all frequencies. Spherical coordinate systems were used in the analyses of the dome assemblies and cylindrical coordinate systems were used for the analyses of all other components. Normal mode studies were performed in MSC/NASTRAN up to 400 Hz to obtain the structural modal parameters. The modal data were analyzed in the post-processor MSC/PATRAN. Global cylinder beam modes included torsion, shearing, axial and bending modes. The circumferential-axial modal frequencies were identified by mode shape and mode number. The index 'i' indicated the number of circumferential waves in the mode shape while the index 'j' specified the number of axial half-waves.

4.1 Longitudinal Stringers

4.1.1 Beam Model

Each of the twenty-four aluminum longitudinal hat stringers measured 143.5 inches long with a 0.1515 in^2 cross-sectional area. The stringers were initially modeled[1] by eighty CBEAM tapered beam elements. PBEAM cross-sectional properties included area, moments of inertia, inertia product, the torsional constant, angle to the primary axis of bending, shear center and neutral axis location offsets, shear stiffness and warp coefficients. Aluminum material properties included an elasticity modulus $E=9.9\ 10^6$ psi, a shear modulus $G=3.8\ 10^6$ psi, a Poisson's ratio $\nu=0.33$ and a specific weight $g\rho_s=0.0978$ pci (pounds/$inch^3$). These material properties were used consistently for all aluminum substructures. Vectors were defined for the beam elements on each stringer to define their proper orientation. The elements of the beam model were offset to position the base of each stringer flush with the 24-inch radius of the cylinder.

Analytical validation - Mode shapes were identified at different modal frequencies for the x-z and the y-z planes as the moments of inertia for the hat stringers are different in the x and y directions. The x-direction was defined parallel to the base of the hat stringer. The y-direction was perpendicular to the x-direction in the cross-sectional plane and the z-axis was along the longitudinal stringer. The numerically calculated modal frequencies for the beam model were compared with analytical natural frequencies of a free-free beam[23] in Reference 14. Rigid body modes at or around zero Hz were ignored. Excellent agreement was obtained for the first nineteen modes (within 1% for the first five modes), validating the numerical results.

Experimental validation - The tapered beam elements of the stringer model contained 81 nodes for 486 degrees of freedom (DOF). The 0.032-inch fillet radiuses rounding all the corners in the stringer cross-section were not included in the analysis. The computed modal frequencies (below 200 Hz) for the beam model are compared with the values from the experimental modal analysis in Table 2. Good agreement was obtained for the first five modes (2.2%-4.0%). Modal frequencies were overpredicted by an average of 7.5% and a maximum of 16.4% for the first twelve modes, indicating that modeling with beam elements yields a finite element model stiffer than the physical structure. Only the flexural modes were considered since no torsional modes were identified in the experimental analysis.

4.1.2 Solid model

A solid finite element model was developed by the NASA Langley Engineering Analysis Branch for comparison with the experimental and beam model frequencies. The solid element model of the stringer was created in Pro/MECHANICA STRUCTURE version 18.0 and consisted of 500 solid P-elements. The model was produced using solid geometry generated from Pro/ENGINEER version 18.0. A modal analysis was performed to determine the modal frequencies up to 200 Hz. The analysis converged to within 1% on frequency. The calculated frequencies and mode shapes for this model are compared with the measured and beam model frequencies in Table 2. The percentage of error is relative to the experimental values. For the first five modes the beam and the solid models compare similarly to the measured modal frequencies. The solid model also shows good agreement with the higher experimental modes below 200 Hz (within 3.5%). This suggests less fidelity of the beam finite element model at those higher frequencies. The finite element solid model of the stringer is large and complex and involved solving 120,738 equations generated for elements having a maximum edge order of 7 in Pro/MECHANICA STRUCTURE. Despite the good agreement with the measurements the solid model was not deemed practical for the ATC model development. However, the beam model did not produce reasonable agreement and consists of one-dimensional elements. This will cause modeling difficulties later when attaching the stringers to the two-dimensional shell elements of the skin. As the stringers do not have a dimension in the plane of the cylinder skin, the bays between stringers and ring frames will be larger with associated lower modal frequencies. The ring frames have U-shaped cutouts to allow the stringers to go through. When the stringers are modeled as beam elements they do not have a dimension perpendicular to the direction of the stringer. There will not be a straightforward way to connect them to the ring frames, since they would be modeled in the center of the U-shaped cutout. These concerns were addressed by updating the beam model to a plate model.

4.1.3 Updated (plate) model

The beam model was updated to a plate element model, which had been proven to be less stiff for a ring frame model in Reference 1. The two-dimensional plate elements (Figure 11) represent the width of the stringers, yielding the same bay areas between stringers in the finite element and physical models. By modeling the stringers with two-dimensional plate elements the connectivity issues with the skin and the ring frames were resolved while the complexity and size of the solid element stringer models were avoided. Each updated hat-shaped stringer finite element model consisted of 434 CQUAD4 elements with 504 nodes and 2520 degrees of freedom. The plate elements were 0.060 inch thick and had aluminum material properties. The numerically calculated modal frequencies are compared with the experimental and previous model data in Table 2. Good agreement was obtained within an average ±2.8% and a maximum 4.3% of the measured modal frequencies.

4.2 Ring Frames

The nine aluminum J-section ring frames had a cross-sectional area of 0.3537 in^2 and an outer radius of 24 inches. Each of the frames was modeled[14] by 96 CBEAM tapered beam elements. Tapered beams were used to include shear center offsets, neutral axis offsets and warping coefficients. The elements of the beam model were offset to position the outer radius of each frame flush with the 24-inch cylinder radius. Vectors were defined for the proper orientation of the beam elements.

Analytical validation - The curvature of the ring frame introduces geometric coupling between the extensional, torsional and flexural modes resulting in two- and three-dimensional mode shapes. The in-plane and out-of-plane ring inextensional vibrations (flexural) are of the most practical importance as the fundamental natural frequencies of the extensional and torsional modes are generally higher. The analytical in-plane, flexural natural frequencies were compared with numerically calculated natural frequencies below 450 Hz[14]. Differences up to 4.4% were found with the larger discrepancies occurring at the lowest frequencies. The out-of-plane inextensional modes, which are coupled to torsional vibrations, resulted in differences up to 5.3% with the maximum at the natural frequency closest to 450 Hz. These percentages were considered small enough (the formulas yield only approximate values) to affirm confidence in the finite element beam models.

Experimental validation - Structural dynamic parameters were obtained from a modal analysis of the accelerometer response due to a hammer impact force at several locations on an isolated ring frame. The ring frame out-of-plane and in-plane mode shapes and modal frequencies are listed in Table 3. Beam, solid, plate and hybrid models were developed and results were compared with the experimental data.

4.2.1 Beam Model

The finite element beam model of the isolated ring frame was updated to include the twenty-four evenly-spaced cutouts of 0.853 by 0.550 inches along the perimeter (Figure 12). The cutouts in the J-section ring fames (Figure 13) are used to provide space for the longitudinal stringers. Also included were 0.37-inch wide by 0.063-inch deep offsets alongside each cutout to accommodate the 0.6-inch thick flanges of the stringers. The stringer cross-sections feature fillet radii of 0.25 inches, which were included in the calculation of the cross-sectional properties. The model contained 168 one-dimensional CBEAM tapered beam elements and 1008 degrees of freedom. The properties of the ring frame cross-section, the ring frame cross-section with the 0.063-inch deep offset and the ring frame section with the cutouts were provided in Reference 14. The 0.125-inch radii in the bottom corners of the U-shaped cutout were not included in the calculation of the cross-sectional properties leaving a rectangular-shaped cutout. The shear center offset corresponded to the distance between the nodal points of each beam element and its cross-section shear center. The neutral axis offset was taken as the distance to the shear center. The cross-sectional y-axis corresponded to the radial axis of a cylindrical coordinate system in the center of the ring frame. An experimental modal analysis of the ring frame was performed up to 250 Hz producing the out-of-plane and in-plane modal frequencies listed in Table 3. The measured and computed modal frequencies in Table 3 reflect the average value of each modal pair. Frequencies of modal pairs were measured not more than 0.5 Hz apart. The part of the ring frame within the cutout was modeled as a beam at the frame perimeter with an offset to its actual location. Since offset vectors in MSC/NASTRAN are treated like rigid elements the numerical model acted stiffer than the actual structure. This is evidenced by the calculated frequencies in Table 3, which are 32.0% to 43.8% higher than the experimental values. Alternative finite element models were developed to address the continuity of the stiffness properties around the ring frame cutouts and improve the poor agreement with the test data.

4.2.2 Solid Element Model

A solid element model was developed and analyzed by the NASA Langley Engineering Analysis Branch to compare resulting modal frequencies with those from the beam model and the modal analysis tests. The solid element model was created in Pro/MECHANICA STRUCTURE version 18.0 and consisted of 1,080 solid P-elements. This model used solid geometry generated from Pro/ENGINEER version 18.0 and included the 24 cutouts in the ring frame. The 0.063-inch offsets and the R.125-fillet radiuses in the bottom of the cutouts were not included due to the added complexity of modeling and the significantly increased time and disk space needed to run the analysis software. A numerical modal analysis was performed to determine all modes up to 200 Hertz (Hz). This analysis converged to within 1% on frequency. The calculated average of the modal pair frequencies are listed in Table 3 for the mode shapes of the solid ring frame model. Excellent agreement was obtained comparing the predicted modal frequencies for the in-plane mode shapes with the frequencies from the experimental modal analysis (within 1.7%-2.4%). Good agreement was also obtained for the out-of-plane modal frequencies (Table 3) suggesting that the modal survey data were reliable. The solid element model underpredicted the modal frequencies. It was hypothesized that inclusion of the R.125-fillet radiuses in the cutouts would make the ring frame stiffer resulting in somewhat higher modal frequencies. The solid element models are complex and sizeable making them prohibitive for the current ATC model development effort.

4.2.3 Plate Model

A simple, four-node quadrilateral plate model was developed which included rectangular ring frame cutouts but not the 0.063 offsets and the R.25 fillet radiuses. The finite element model contained 168 plate elements and 289 nodes for a total 1734 degrees of freedom. The calculated modal frequencies were 15%-35% lower than the measured frequencies. To improve on these results, the Langley Structural Dynamics Branch remeshed the model and used 2640 CQUAD8 plate elements and 9072 nodes with more than 45000 degrees of freedom. The modified plate model produced better correlation with the experimental modal frequencies than the simple plate and the beam models but still underpredicted the out-of-plane modal frequencies by 16.2%-18.7% and for the in-plane modal frequencies by 8.7%-9.9%[14]. These lower predicted modal frequencies indicate that the finite element model is less stiff than the actual test structure.

4.2.4 Hybrid Model

Although the modified plate model produced better results than the simple plate and beam models, it still yielded poor comparison with the measured data. Since the beam model was stiffer than the actual ring frame and the plate model did not provide enough stiffness, a hybrid model was developed combining the one- and two-dimensional models. The web of the J-section ring frame was modeled with plate elements while beam elements were used for the flanges of the ring frame. Tapered beams were used to include shear center offsets, neutral axis offsets and warping coefficients. The elements of the beam model were offset to position the outer radius of each frame flush with the 24-inch cylinder radius. Vectors were defined for the proper orientation of the beam elements. The hybrid model consisted of 216 CQUAD4 and 288 CBEAM elements with 458 nodes for 2472 degrees of freedom. The hybrid model compared well with measured out-of-plane modal frequencies (within 2.5%-2.9% error) as shown in Table 3. The calculated in-plane modal frequencies were too high by a margin of 6.4%-7.6%. All modal frequencies for the hybrid model were predicted[1] within an average 4.3% of the measured modal data.

4.2.5 Updated Hybrid Model

The two-dimensional hybrid model does not have a geometrical thickness. When the ring frames are attached to the longitudinal stringers and the cylinder shell, the bay area bounded by the stringers and the frames will thus be larger, resulting in higher bay panel modal frequencies. In the updated hybrid model plate elements were introduced for the flanges atop the J-section and along the cylinder shell to ensure the proper dimensions of the bay area. These CQUAD4 elements were 0.125-inch thick except for a length of 0.35 inch on either side of the U-shaped cutouts where the thickness is 0.063 inch to accommodate the 0.06-inch thick longitudinal stringers. CQUAD4 elements were also used to model the 0.1-inch thick web of the J-stiffener down to the bottom line of the U-shaped cut-outs. The L-shaped part of the ring frame below the cut-out was modeled with tapered beam elements. These CBEAM elements had a 0.116 in^2 cross-sectional area. The total number of 432 CQUAD4 elements and 168 CBEAM elements combined to an estimated 3,033 degrees of freedom for each ring frame. Aluminum material properties were assumed for all elements. Although comparison with the measured out-of-plane modal frequencies was less favorable (2.4%-6.7%) as for the initial hybrid model, the agreement with the measured in-plane modal frequencies was improved (3.1%-3.9%). All modal frequencies for the hybrid model were predicted[14] within an average 4.7% of the measured modal data.

4.3 End Rings

The ring frame at each end of the cylinder was initially modeled[14] using CBAR elements with a cross-sectional area of 3.0 in^2. The simpler CBAR elements instead of CBEAM elements could be used as the shear center axis and neutral axis for rectangular cross-sections coincide. The one-dimensional bar elements, however, do not have a geometrical thickness yielding a wider bay area between the ring frames and the end frames of the cylinder. Solid elements for the end ring frames were introduced in an updated model to ensure the proper width of the bay area and to more accurately model the cross-sectional geometry. No modal testing was performed on the end ring as a single component.

4.4 Shell

The mesh representing the cylinder shell consisted of 40 CQUAD8 curved quadrilateral elements in the longitudinal direction and 48 CQUAD8 shell elements in the circumferential direction[14]. The shell bays bounded by the stringers and frames contained a four by two matrix of CQUAD8 elements. The shell was made of aluminum and had a thickness of 0.040 inch. The shell was not tested as an individual component.

4.5 End Plates

The end plates consisted of a half-inch thick plywood panel mounted onto two-inch thick particleboard. The particleboard was chosen for its high density, high rigidity and low cost. Two circular patterns of twenty-four equidistant half-inch holes were drilled at radii of 7.5 and 9 inches from the center. The openings allow the pressure on both sides of the end plates in Configuration VI to equalize during the pressurization tests. The end plates were initially modeled as one panel using 1184 CTRIA3 elements[14] with the nodes along the outer edge coinciding with the nodes of the shell CQUAD8 elements. The panel had particleboard material properties and the thickness of the particleboard end plate was increased by 0.31 inches to account for the specific weight ($g\rho_{pb}$=0.0177 pci) of the plywood panel. The particleboard had an elasticity modulus E_{pb}=2.1755 10^6 psi, a Poisson's ratio ν_{pb}=0.33 and a specific weight $g\rho_{pb}$=0.0284 pci. No experimental modal data were available for comparison.

4.6 Domes

The S-fiberglass composite end domes have a high stiffness-to-weight ratio and were designed to be sufficiently strong to safely carry the pressure loading during pressure testing. End cap rings supported and strengthened the rim of each dome. Access ports with a 10-inch diameter were installed in the center of each dome to accommodate devices that will regulate the interior pressure conditions. The end cap rings and access ports were initially considered part of the dome and were not individually modeled[14]. The fiberglass composite material consisted of an eleven-ply S-glass laminate with fibers alternately in the 0 and 45 degrees directions for a total thickness of $t_{(dome)}$=0.242 inches. PCOMP properties were entered for a composite laminate with two-dimensional orthotropic layer material properties. The domes were modeled with 8448 CTRIA6 curved triangular shell elements[14]. The nodes of these triangular elements coincided with the nodes of the CQUAD8 elements at each end of the cylinder shell. A micro-mechanical analysis for the composite laminate produced elasticity moduli in the 0 and 90 degrees directions $E_{(dome)x}$=6.301x10^6 psi, $E_{(dome)y}$=2.557x10^6 psi, a shear modulus $G_{(dome)xy}$=1.279x10^6 psi, and a Poisson's ratio of ν_{dome}=0.276. The specific weight of $g\rho_{(dome)}$=0.067 pci was obtained by assuming that the epoxy resin occupies half of the volume of the composite. No experimental modal data was available at the time the initial dome finite element models were created.

5 INITIAL ATC CYLINDER FINITE ELEMENT CONFIGURATIONS

5.1 Bare Frame Configuration I

Experimental modal parameters were extracted for frequencies up to 148 Hz for the bare frame cylinder Configuration I, which included the longitudinal stringers, the ring frames and the end rings (Figure 2). The measured modal frequencies and associated damping values are listed in Table 4. An initial ATC finite element model was developed for Configuration I by assembling the substructure models. The resulting finite element model was equivalenced to remove redundant nodes. A structural damping of 0.01 was used for all frequencies. Post-processing and identification analysis of the MSC/NASTRAN generated normal mode data yielded the structural cylinder modes, which are listed in Table 4 for comparison with the measured data. Zero- and first-order circumferential cylinder beam modes included torsion, shearing, axial and bending modes. The circumferential-axial modal frequencies were identified by mode shape and mode number. The index 'i' indicates the number of

circumferential waves in the mode shape while the index 'j' specifies the number of axial half-waves. The measured modal frequencies were overpredicted by an average 9.6% with discrepancies as high as 16.7% for the first 61 modes. The predicted and measured frequencies for the first seventeen modes are compared in Figure 14.

5.2 Frame and Skin Configuration III

The measured modal frequencies and modal damping of Configuration III (Figure 4), consisting of the longitudinal stringers, the ring frames, the end rings and the skin, are listed in Table 5. A finite element model of this configuration was developed for comparison with the experimental results. The components of Configuration III were assembled and the model was equivalenced. A normal mode analysis up to 400 Hz was performed in MSC/NASTRAN. Post-processing in MSC/PATRAN yielded the structural mode shapes. In addition to the cylinder modes, twenty-nine different modes of the fundamental resonance of the subpanels, bounded by the stringers and ring frames, were calculated in the finite element normal mode analysis. Each of these fundamental subpanel modes was related to a different global mode shape of the cylinder structure. The subpanels were therefore subjected to different boundary conditions for each circumferential-axial cylinder mode shape. Subpanel mode shapes were identified at frequencies above 367 Hz. Although the agreement between the predicted and measured modal frequencies was generally better for Configuration III than for Configuration I, discrepancies up to 13.7% were encountered for the first 61 modes. The subpanel modes identified by the finite element model computations were not extracted from the experimental modal analysis due to the limited excitation and response locations and the associated lack of mode shape resolution.

Although the modal predictions for each of the component finite element models were in reasonable agreement with the results of the experimental modal surveys, the assemblies of these components showed poor agreement. It was concluded that the component finite element models needed to be improved to obtain better agreement between predictions and measurements for the assembled configurations.

6 ENHANCEMENT OF THE COMPONENT FINITE ELEMENT MODELS

6.1 Longitudinal Stringers

Several approaches were investigated to increase the fidelity of the finite element model for the longitudinal stringer including the use of eight-node quadrilateral plate elements, employing a combination of plate elements and beam elements and increasing the number of CQUAD4 plate elements. Only doubling the number of the CQUAD4 plate elements noticeably improved the fidelity of the finite element model. Differences between the predicted modal frequencies of the enhanced model and the measured results were within an average of 2.1% and a maximum of 3.7% as shown in Table 6. The predicted frequencies for the updated stringer model (Table 2) are also listed in Table 6. The consequence of increasing the number of elements was that not only the stringer model became larger but also that the models of the connecting components needed to be updated with a higher number of elements. A total of 32,592 CQUAD4 plate elements were used to model the twenty-four longitudinal stringers.

6.2 Ring Frames

Enhancement studies to improve the predicted and experimental agreement for the individual ring frames focused on the modeling around the twenty-four U-shaped cutouts. Several approaches were attempted, using rigid RBE1, RBE2 or RBE3 elements, incorporating multi-point constraints (MPCs) and modeling plate elements around the cutouts. The enhanced finite element models showed improvement in the results for the in-plane or out-of-plane mode shapes and related modal frequencies, but not for both. The initial modeling of the hybrid ring frame had indicated that the beam elements were too stiff while the plate elements did not provide enough stiffness to the ring frame. Correlation with the experimental modal frequencies was improved by optimizing the J-stringer areas for

which plate elements and beam elements were used. The beam elements were modeled at different distances from the base of the U-shaped cutouts. Modal frequencies were computed for each configuration and compared with the measured modal data. Best agreement was obtained for the beam elements modeled 0.2 inches below the U-shaped cutouts. The number of elements was doubled in the enhanced ring frame model to match the number of nodes at the junction points with the longitudinal stringers (Figure 15). The nine ring frames were modeled with a total of 3,024 CBEAM and 2,304 CQUAD4 elements. The predicted modal frequencies of the enhanced ring frame models were within an average 1.5% and within a maximum 2.6% of the measured modal frequencies (Table 7). The predicted frequencies for the updated ring frame model (Table 3) are also listed in Table 7.

6.3 End Rings

The number of elements for the enhanced end rings was increased to match the number of nodes at the junction points of the shell and the longitudinal stringers. The 3840 CHEXA solid elements were assigned aluminum material properties and yielded an approximate 36,000 degrees of freedom for each end ring.

6.4 Shell

The number of the quadrilateral CQUAD4 plate elements for the enhanced shell was doubled in two directions to match the increased number of nodes at the junction points with the longitudinal stringers and the ring frames. The mesh representing the cylinder shell was modeled with 56,064 CQUAD4 elements for the skin along with 432 CTRIA3 elements for connectivity to the end rings.

6.5 End Plates

The end plates were remodeled with separate subcomponents for the particleboard and plywood panels. The number of elements for the enhanced end plates was increased to match the number of nodes at the junction points with the longitudinal stringers, the shell and the end rings. No experimental modal data was available for the particleboard and plywood panels to compare modal predictions with measured data. CTRIA3 elements were replaced with CQUAD4 elements. The two-inch thick particleboard had an elasticity modulus $E_{pb}=2.1755\ 10^6$ psi, a Poisson's ratio $\nu_{pb}=0.33$ and a specific weight $g\rho_{pb}=0.0284$ pci. The half-inch thick plywood featured an elasticity modulus $E_{pw}=1.2\ 10^6$ psi, a Poisson's ratio $\nu_{pw}=0.33$ and a specific weight $g\rho_{pw}=0.0191$ pci. The particleboard panels were modeled with a total of 3,072 CHEXA elements while 2,304 CHEXA elements were used for the plywood panels.

6.6 Domes

The domes were remodeled with separate subcomponents for the dome shells, the dome rings and the access plates (Figure 16). The two 0.5-inch thick aluminum access plates were modeled with 864 CQUAD4 plate elements. The two dome shells consisted of a total of 9,408 CQUAD4 elements. Plate element offsets were applied to account for the proper center plane locations. The dome material properties were updated to reflect the lay-up indicated by the original engineering drawings of the ATC. The S-fiberglass and epoxy matrix mechanical properties are listed in Table 8. The lamina composite properties were obtained by proportioning the S-fiberglass and epoxy matrix mechanical properties with respect to relative volume. The composite elasticity moduli for one layer were calculated from $E_{11}=E_fV_f+E_mV_m$ and $E_{22}=E_m(1+2\eta V_f)/(1-\eta V_f)$, where the composite modulus factor η is given by $\eta=(E_f/E_m-1)/(E_f/E_m+2)$. The shear modulus was determined from $G_{12}=G_fG_m/(G_fV_f+G_mV_m)$ and the specific weight from $g\rho_c=g\rho_fV_f+g\rho_mV_m$. The lamina composite mechanical properties are tabulated in Table 8. The new laminate stacking sequence is shown in Table 9. The laminate mechanical properties were computed in MSC/PATRAN for the stacking sequence in Table 9 resulting in $E_{xx}=4.55\ 10^6$ psi, $E_{yy}=2.10\ 10^6$ psi, $G_{xy}=1.20\ 10^6$ psi and $\nu_{xy}=0.432$. The dome end frames were modeled with 384 HEX8 solid elements. The solid elements reflected both the aluminum properties of the 0.375 inch-thick dome end frame itself and the material properties of the 0.25-inch thick fiberglass dome edge material. The mechanical properties for the composite of the two materials was calculated

using volume proportionality (V_a=0.6 and V_e=0.4) resulting in E_{ae}=7.26 10^6 psi, G_{ae}=2.74 10^6 psi and ν_{ae}=0.322. Modal frequencies and mode shapes were computed for finite element models of the enhanced isolated fiberglass domes with the dome end frames and access plates installed. Modal hammer impact survey measurements were conducted on one of the domes with simulated free-free boundary conditions. Good agreement (within 5.6%) was obtained between the measured and the predicted modal frequencies for the first six circumferential modal pairs. The results are shown in Table 10.

7 REFINEMENT AND VALIDATION OF THE ATC CONFIGURATION MODELS

7.1 Configurations I and III

Agreement between predicted and measured modal frequencies for the longitudinal stringers and ring frames was improved by doubling the number of plate elements. These enhanced stringer, frame and end ring models were assembled to form the ATC Configuration 1 shown in Figure 17. Table 4 listed the Configuration I measured modal frequencies and the percentage of error made with the predictions for the assembly of the unenhanced components. This data is compared in Table 11 with the predicted modal frequencies for the enhanced component assembly. The enhanced assembly was weaker at the junctions between the stringers and the frames and underpredicts the measured modal frequencies by an average of 10.6% and a maximum of 23.9%. A schematic of the junction of the unenhanced hat-section longitudinal stringer and the J-section ring frame is shown in Figure 18a. The plate elements of the two bottom hat-section stringers were modeled to line up with the two element rows at the top of the J-section ring frames. The stringers and ring frames are thus connected by a total of twelve nodes at each junction. By doubling the number of elements for the enhanced stringers and frames the number of common nodes at the junctions increased from twelve to thirty as illustrated in the schematic of Figure 18b. The thirty-node junctions exhibit less rigidity and the modal frequencies of the softer cylinder frame occur at lower frequencies. The lower modal frequencies for the thirty-node configuration are listed in Table 11 where they are also compared with the measured modal frequencies. The longitudinal stringers and ring frames were subsequently remodeled to merge elements at the junctions in such a way that connections were only made at six node locations (Figure 18c). Comparison between the predicted modal frequencies for these six-node junction configurations and the measured modal frequencies improved considerably as listed in Table 11. The predicted modal frequencies were within an average 4.4% and a maximum of 7.5% of the measured data. Figure 19 shows the prediction/measurement errors as function of mode number for the different node junctions of Configuration I. It was concluded that a lower number of common nodes at the junctions of the longitudinal stringers and the ring frames resulted in stiffer substructure assemblies with associated higher modal frequencies. It should be noted that for the three configurations in Figure 18a, Figure 18b and Figure 18c not only the number of common junction nodes changes but also the layout of the node connections, which also affects the rigidity of the junction.

ATC Configuration III adds the skin to the stringer/ring frame/end ring structure of Configuration I (Figure 20). This configuration was investigated for the three different junctions in Figure 18a, Figure 18b and Figure 18c with similar results. The predicted modal frequencies for the thirty-node and six node junctions for the enhanced components are compared with the measured modal frequencies in Table 12. The errors between predictions and measurements are also listed in Table 12 for both cases along with the error for the twelve-node junction assembly of the unenhanced stringers and frames, which had been previously listed in Table 5.

The data in Table 11 and Table 12 show that the thirty-node junctions yield lower modal frequencies than measured in the modal surveys and the six-node junctions result in higher modal frequencies. To improve the comparison between predictions and measurements the plate elements at the junctions of the longitudinal stringers and ring frames of Configuration 1 were refined to have twelve common nodes. The twelve nodes were implemented at approximately the same locations as the rivets that connect the stringers and the frames in the hardware model. The modal frequencies predicted for the refined Configuration I model with the enhanced components and the twelve-node junctions are compared with the measured data from the modal surveys in Table 13. Sixty-one measured modal frequencies below 150 Hz were compared. Excellent agreement was obtained (75% of the data had less than 6%

error and all data had less than 9.3% error). The errors between measurements and predictions of the unrefined Configuration I with the unenhanced components (Table 4) are also listed in Table 13 to show the improvements of the refined twelve-node model. Figure 19 illustrates the prediction/measurement errors as function of mode number for all the different node configurations of Configuration I.

Predictions were also made for the refined Configuration III with the enhanced components and the twelve common nodes. Thirty-nine predicted modes up to a frequency of 352 Hz were identified from the MSC/PATRAN post-processed results. Twenty-nine modal frequencies up to 315 Hz were obtained from the experimental modal analysis and are compared with the predicted modal frequencies in Table 15. Good agreement was obtained for the refined configuration with modal frequencies predicted within an average 4.3% and a maximum of 9.9% of the measured data. The errors between measurements and predictions of the unrefined Configuration I with the unenhanced components (Table 4) are also listed in Table 15 to show the improvements of the refined twelve-node model. The refined finite element models of Configurations II, IV and V, featuring the enhanced components and the twelve-node junctions are depicted in Figure 21, Figure 22 and Figure 23, respectively, and will be discussed in the following sections.

7.2 Configuration II

ATC Configuration II consists of the same longitudinal stringer/ring frame/end ring structure as Configuration I but end plates are added (Figure 21). Predicted modal frequencies of the refined Configuration II were identified by mode shape for seventy-seven measured modal frequencies up to a frequency of 245 Hz. Measured and predicted modal frequencies are listed in Table 15 along with the errors. All errors were within an average 6.0% and a maximum of 10.9%.

7.3 Configuration IV

Numerical and experimental modal parameters up to 400 Hz were compared for the refined ATC Configuration IV, which included the ring frames, longerons, skin, end rings and end caps (Figure 22). The finite element model had predicted up to 15 % higher modal frequencies for the unrefined model (before increasing the number of elements of the stringer, frame, end rings and skin) than were obtained from the experimental modal analysis. Twenty-three measured modal frequencies below 325 Hz. were compared with predictions. The results and error values are tabulated in Table 16. Reasonable agreement was obtained with all the data within an average agreement of 5.2% and a maximum of 15.2%. The ATC Configuration IV structural mode numbers, modal frequencies and mode shapes are illustrated in Figure 24 for seventy-two modes.

7.4 Configuration V

Adding the domes to Configuration IV to obtain Configuration V (Figure 23) significantly increased the predicted modal frequencies for all modes. The predicted modal frequencies for the refined Configuration V are compared with the measured modal parameters in Table 17. More than one-third of the predicted modal frequencies were more than 10% higher than the experimental values. The lowest order circumferential modes exhibited the highest discrepancies when compared with the experimental data. This suggested that the end boundary conditions of the cylinder were too stringent and needed to be relaxed to obtain better agreement. Detailed inspection of the test article showed that the dome rings were attached to the cylinder end rings in a radial direction and not in the axial direction. The finite element model was modified to incorporate this design by leaving a small, 0.09 inch thick, radial gap between the dome ring and the cylinder end rings. This gap was larger than the equivalencing tolerance used in MSC/PATRAN to prevent two opposite nodes from being merged when using the equivalencing feature. Predicted modal frequencies up to 450 Hz of the Configuration V with gap are listed in Table 18 and are compared with the measured modal frequencies for the same hardware configuration. Error values between predicted and measured data for Configuration V with and without the gap are also shown in Table 18. The agreement between predicted and measured modal frequencies was improved for the two i=2, j=1 circumferential-axial modes by more

than 5%. However, disagreement for the first bending modes and the circumferential-axial modes i=2, j=2 and i=2, j=3 remained well above 10%. Zero- and first-order circumferential cylinder beam modes included the torsion, axial and bending modes. The Configuration V structural mode numbers, modal frequencies and mode shapes are illustrated in Figure 25 for eighteen structural modes. Predictions were also made for the fundamental modes of the cylinder subpanels bounded by the ring frames and longerons. The subpanels are subjected to different boundary conditions for each circumferential-axial cylinder mode shape. The panel modes occur therefore at a multitude of frequencies, each of which is related to a specific global circumferential-axial mode shape of the ATC cylinder structure.[14] An example is shown in Figure 26 where the fundamental panel modes are superimposed on a 0,2 global cylinder mode shape at 351.75 Hz. Post-processing and identification analysis of the MSC/NASTRAN generated normal mode data also yielded stringer modes that were related to the vibration of the cylinder as a single structure. Figure 27 shows a stringer mode superimposed on a 1,3 global cylinder mode shape. Longitudinal stringer and subpanel/stringer modes of the tenth order have nodal points that coincide with the axial locations of the ring frames. These mode shapes were easily identified and are tabulated in Table 18. Several more panel and stringer modes superimposed on global cylinder modes are shown in Figure 24 for the Configuration IV and in Figure 25 for Configuration V. Differences between predicted and measure circumferential-axial modal frequencies for each of the refined Configurations I-V are illustrated in Figure 28.

7.5 Configuration VI

Pressure differential loadings of 3 psi and 6 psi were incorporated in the finite element model of Configuration VI. The MSC/NASTRAN 'STATSUB' command was used for the computation of the normal modes. The command selects the static solution to form the differential stiffness for the elements with the pressure loads. However, MSC/NASTRAN does not allow the processing of models with beam element offsets. The nine ring frames of the ATC were modeled with beam element offsets to position the shear center axis at the appropriate location relative to element grid points. These offsets were an integral part of the modeling of the ring frames and were key for obtaining good comparison between the measured and the numerically calculated modal frequencies. The beam offset vectors are treated like rigid elements in MSC/NASTRAN and remain parallel to their original locations making them not suitable for differential stiffness calculations. Even when the pressure loading is applied to only the shell and not the beam elements, the beam elements are still part of the MSC/NASTRAN run and cause a fatal error. An alternative approach was considered creating superelements for the ring frames that would contain the offsets but would be analyzed separately from the residual structure. Superelements are normally used as Main Bulk Data Superelements or PARTS, which allow partitioned input files. However, MSC/NASTRAN would still attempt to do an analysis of the upstream superelement when using the 'STATSUB' command and thus encounter the same incompatibility with the offsets of the beam elements. The solution was found in the implementation of external superelements. The initial normal mode calculations of the ring frames superelement were performed outside the main finite element program and the resulting matrices were then stored in an '.op2' output file. Modal frequencies obtained for the external superelement were verified to be identical as for the individual ring frame modal frequencies. The superelement output file was subsequently used as input to the bulk data file of the residual structure. Modal frequencies for the combination of residual structure and external superelement were confirmed to be the same as for the original ATC cylinder with the ring frames. The pressure differential loadings of 3 psi and 6 psi were applied only to the shell elements of the ATC. The model was prepared in MSC/PATRAN for a linear static analysis and an input bulk data file was compiled. The bulk data file was manually modified to perform the normal mode analysis with the calculated differential stiffness by adding a new subcase with the STATSUB command. The predicted numerical modal frequencies of the ATC Configuration VI are compared with measured modal survey data in Table 19 for 3 psi pressurization and in Table 20 for the case of 6 psi pressurization. Figure 29 shows the differences between the measured and predicted modal frequencies for 6psi and zero pressurization. Differences between the numerical and experimental modal frequencies are of the same order as the differences for the unpressurized cylinder. This is also illustrated in Table 21 where the measured differences are compared with the predicted differences of the modal frequencies due to the 3 psi pressurization. The average disagreement between the measured and predicted differences was less than 1.0% while the maximum disagreement was 5.2%. The measured and predicted differences in modal frequencies due to the 6 psi pressurization are shown in Table 22. The average disagreement between the measured and predicted differences was 0.5% and the maximum disagreement was only 1.2%. When pressure differential loadings were applied to the dome elements, in addition to the shell elements, only a negligible shift (less than 0.3%) in the predicted modal frequencies was observed.

8 ACOUSTIC NORMAL MODES

The interior of the ATC was modeled by 5184 solid finite elements in MSC/PATRAN. The neutral file of the model was imported into COMET/Vision for pre-processing. The resulting file was executed in COMET/Acoustics to calculate fifty acoustic modes up to a frequency of 600 Hz. Post-processing was performed in COMET/Vision to identify the modal frequencies by mode shape. The first forty-eight predicted modes are listed in Table 23 along with half-wavelength mode numbers in axial, circumferential and radial directions. The mode numbers, the modal frequencies and the mode shapes are depicted in Figure 30. The first axial (1,0,0) acoustic mode was predicted at 46.9 Hz, the first circumferential (0,1,0) mode at 165.2 Hz and the first radial (0,0,1) acoustic mode was calculated to occur at 345.1 Hz. An acoustic survey was conducted with a loudspeaker and a cross-sectional array of sixteen microphones. An amplified white noise signal was used as input to a loudspeaker located at the center of one end plate. The cylinder interior acoustic space was scanned in the axial direction with the microphone array to identify acoustic modal frequencies and categorize their mode shapes. The measured modal frequencies are listed alongside the predicted results in Table 23. Reasonably good agreement was obtained for 34 predicted modes which, on the average, were within 2% of the measurements. The predicted first acoustic (axial) mode at 46.9 Hz was 6.6% lower than the measured frequency 50.6 Hz. The maximum discrepancy between predictions and measurement for the other measured acoustic modes (33) was 3.8%. The acoustic predictions were made for a hard-walled cavity and no damping was applied.

9 FREQUENCY TRANSFER FUNCTIONS

Frequency transfer functions between a unit force on the structure and the acoustic response inside the ATC configuration V cylinder were measured, predicted and compared.

9.1 Measurements

An array of sixteen microphones was used to measure the acoustic response inside the cylinder. The microphones were distributed over four perpendicular radial shafts supporting four microphones each (Figure 31). The microphones on each shaft were located at radial distances of 7, 12, 16.5, and 21 inches from the cylinder center. The four shafts were mounted on a traverse mechanism with rotation capabilities. Measurements were taken at six angular positions 15 degrees apart. After the acoustic data acquisition was completed at the starting location the traverse was stepped to the next axial position and measurements were acquired for the same six angular positions. This process was repeated for fifteen axial locations of the microphone array in the cylinder. The parameters defining all the microphone measurement locations of the acoustic survey are listed in Table 24. Random excitation was applied to the cylinder by an electrodynamic shaker mounted on the second cylinder ring frame in a radial direction at an angle of -7.5 degrees with the horizontal centerline. The input force, drive point acceleration, and microphone array measurements were recorded for each of the traverse positions. The acoustic response measurements were normalized by the input force.

9.2 Predictions

A structural-acoustic analysis was performed in COMET/Acoustics to calculate the interior acoustic response due to a unit force input on the structural model of the ATC configuration V. The unit force drives the structure into vibration which subsequently interacts with the interior acoustic medium. COMET/Acoustics provides a coupled analysis using the indirect boundary element method. Coupled analysis is a three step process. First, the structural normal modes in a vacuum are computed by MSC/NASTRAN. Next COMET/Vision transforms the structural modes into a format readable by COMET/Acoustics. The modal basis is then combined with the acoustic boundary element model to calculate the combined structural/acoustic response and the resulting acoustic responses. The

displacement vector results from a normal mode analysis performed in MSC/NASTRAN were output to a punch (.pch) file. The modal analysis included thirty-two participating modes which are listed in Table 25. Structural damping factors measured at the experimental modal frequencies were used as the damping factors for the equivalent modes in the numerical analysis and are also indicated in Table 25. The finite element model of the ATC Configuration V was used for the structural acoustic modal analysis and is depicted in Figure 32. An acoustic boundary element model (BEM), fully enclosing the interior acoustic space of the ATC cylinder, was developed in MSC/PATRAN. The acoustic model, consisting of 2400 QUAD4 elements and 2402 nodes, is 142 inches long and has a diameter of 48 inches (Figure 33). Acoustic data recovery meshes were defined in MSC/PATRAN and consist of four cross-sectional surfaces and a surface for which the length coordinate is parallel to the cylinder centerline. Each cross-sectional surface has a 23.795 inch radius and is constructed of 240 QUAD4 elements and 265 nodes. Cross-sectional data recovery mesh (DRM) surfaces were located at distances of 47.33, 94.67, 106.50, 113.60, 118.33 inches from the ATC cylinder end plate (Table 24) to coincide with the measurement surfaces. The planar surface with its length coordinate along the cylinder centerline is oriented at a 7.5 degree from the vertical y-axis perpendicular to the unit force applied to the cylinder surface. The rectangular data recovery surface is 131.35 inches long, 47.59 inches wide and consists of 592 QUAD4 elements and 688 nodes. The assembled DRM for the acoustic cylinder interior is shown in Figure 34. The assembled DRM inside the acoustic BEM is depicted in Figure 35. The DRM is 10.65 inches shorter than the BEM to replicate the measurement surfaces as illustrated by the side view of the DRM in Figure 36. In COMET/Vision a group was created for the acoustic interface elements consisting of the entire BEM. Material properties for air were assigned and views for comparison with experimental results were created. Parameters for a coupled indirect boundary element analysis were set and a COMET/Acoustics data deck was written and saved. The MSC/NASTRAN model of the ATC Configuration V bulk data file was imported. A unit force was applied to a structural node located 28.8 inches down the z-axis at a 7.5 degrees angle with the x-axis (Figure 37). This is the same location where the electrodynamic shaker was mounted in the experimental set-up. The associated finite element results of the modal basis contained in the MSC/NASTRAN punch file were identified and the structural interface information was written to the end of the COMET/Acoustic data file. The COMET/Acoustic analysis was executed and the resulting acoustic response database was post-processed in COMET/Vision.

9.3 Comparison of Results

Comparisons of the experimental and numerical results are illustrated in Figure 38 through Figure 52. A unit force was applied to the structural model at 46.9 Hz, the frequency at which the first axial acoustic mode was predicted (Table 23 and Figure 30). Figure 38 shows the predicted interior acoustic response projected onto the Data Recovery Mesh (DRM). The interior acoustic data are compared with the results of the measurements taken inside the ATC when excited by a unit force at a frequency of 50.625 Hz, the frequency at which the first axial acoustic mode previously had been measured (Table 23). The first structural modes of the ATC were measured and predicted at much higher frequencies (Table 18) and do not substantially affect the response of the first acoustic mode. Please note that he scales for the predictions and measurements have different minimum and maximum values and feature a slightly different color gradation. Good agreement is obtained between the analytical and experimental results.

The first structural mode (i=2, j=1) was predicted at 86.6 Hz and was measured at 79.13 Hz (Table 18). The i-index refers to the circumferential mode shape while the j-index describes the mode shape in axial direction. The excitation frequency for the measurements was determined from the peak response in the structural frequency response function. Since the ATC had been moved to a different location for these measurements the structural modal frequencies occur at a slightly different frequency (80.625 Hz) than measured before (79.13 in Table 18). Other structural modal frequencies also had changed somewhat in value. The predicted and measured interior acoustic responses are compared in the isometric view of Figure 39. The color bars for the analytical and experimental results are again similar but not identical. The side view in Figure 40 shows good agreement between the predicted and measured responses in the axial direction. Figure 41 presents a rear view of the predicted DRM and measured cross-sectional acoustic response. The rear view shows the left-most DRM in Figure 39 (at 47.33 inches from the left end plate in Table 24) as the acoustic response is being viewed from the left hand side of the figure. The second (i=2) circumferential mode is clearly defined in the predicted as well as in the measured acoustic response. The cross section at 118.33 inches from the left endplate (Figure 39) is shown as the front view of the

acoustic response in Figure 42. The excitation of the second circumferential mode is well defined in the predicted as well as in the measured acoustic response.

Excitation at the measured (3,1) structural mode (145.625 Hz) shows the structural mode shape in the measured acoustic response of Figure 43. However, the predicted (3,1) structural mode (144.22 Hz in Table 18) is obscured in the predicted acoustic response by the first x- and y- bending modes predicted at 146.76 and 147.59 Hz, respectively (Table 18). These predicted bending modes were measured at 123.17 and 124.19 Hz, well separated from the experimental excitation frequency at 145.625 Hz and thus do not show in the measured response.

The acoustic response due to the predicted excitation at the (3,2) structural modal frequency (177.6 Hz in Table 18) is compared with excitation at the measured (3,2) structural mode (173.125 Hz) in the isometric view of Figure 44. The color bars for the predicted and measured results show different minimum and maximum values, feature a different color gradient and should be interpreted accordingly. Figure 45 shows the second axial structural mode in the predicted as well as the measured acoustic response. The three diagonal nodal lines of the third circumferential mode also show in the predicted and measured acoustic responses as shown in the rear views of Figure 46. This cross section is located 47.33 inches from the left end plate, not too far from the excitation point on the structure (28.8 inches from the left end plate). The front view shown in Figure 47 is at the cross-sectional location 118.33 inches from the left end plate and much farther from the excitation point. At this location the measured acoustic response is dominated by the (1,1,0) acoustic mode at 171 Hz (Table 23) showing only one diagonal nodal line. The predicted interior acoustic response, however, is still dominated by the (3,2) structural mode at which modal frequency it was excited. This is conceivable since the predicted structural frequency at 177.6 Hz is not as close to the predicted acoustic mode (171.8 Hz in Table 18) as the measured structural modal frequency at 173.25 Hz is to the measured acoustic mode (171 Hz in Table 18).

Comparison of the predicted and measured interior acoustic responses in Figure 48 shows that, when excited at the (4,2) structural modal frequency, the cross-sectional pattern is a combination of the (4,2) structural mode shape and the (0,2,0) acoustic mode shape. The structural and acoustic modal frequencies are approximately 6 Hz apart in both the measurements as in the predictions. The axial pattern is dominated by the second axial structural mode shape excitation as the (0,2,0) acoustic mode does not have an axial shape parameter.

Excitation at the (3,4) structural modal frequency is shown in the isometric view of Figure 49. The (3,4) structural mode was predicted to occur at 313.6 Hz (Table 18). An acoustic modal response with a mode shape of (3,2,0) at 308.8 Hz (Table 23) is predicted close to the 313.6 Hz structural excitation frequency. The fourth axial mode shape (Figure 25) of the structural mode couples well with the third acoustic axial mode shape since both have three nodal lines. This is depicted in Figure 50 for the predicted axial acoustic response. A similar acoustic distribution is observed in the measured acoustic response of Figure 50. The (3,4) structural mode was measured at 285 Hz and the (3,2,0) acoustic mode shapes was measured at 303.8 Hz. Figure 51 and Figure 52 show a predicted composite of the third circumferential structural mode due to excitation at the predicted (3,4) structural modal frequency and a possible second circumferential acoustic mode. A similar interior acoustic pattern, but more dominated by the measured second circumferential acoustic mode is shown for the excitation at the measured (3,4) structural modal frequency.

10 SUMMARY

Finite element modal analyses for free boundary conditions were performed on a longitudinal stringer, a ring frame, a pressure dome, and six component assembly configurations of the Aluminum Testbed Cylinder (ATC) for comparison with experimental modal frequencies. The stringers were updated from beam to plate element models and enhanced by doubling the number of elements. Excellent agreement was obtained within an average 2.1% and a maximum 3.7% of the measured modal frequencies. The hybrid ring frames were optimized by adjusting the area represented by the plate elements and remodeling the relocated beam elements. The frames were enhanced by doubling the number of elements. The predicted modal frequencies were within an average 1.5% and within a maximum 2.6% of the measured modal frequencies. The fiberglass composite domes, the dome end cap rings and

the dome access ports were individually modeled with appropriate material properties to increase model fidelity. Predicted modal frequencies were within an average 2.9% and a maximum of 5.6% of the measured data.

The end rings, shell and end plates were remodeled to reflect the increase in elements of the enhanced stringers, frames and domes. The increased number of grid points at the junctions of the enhanced stringers and frames resulted in less stiff component assemblies with associated lower modal frequencies. The junctions were remodeled to have only twelve instead of thirty common nodes at approximately the same locations as the rivets in the hardware model. Good agreement was obtained for Configurations I, II and III as predicted modal frequencies were within an average 2.9%-4.4% and a maximum 5.1%-9.9% of the measured data. The experimental boundary conditions for configurations IV through VI were simulated by a four air-bag isolator support. Predictions for Configurations IV and V were within an average 5.3%-9.1% and a maximum 13.9%-25.3% of the measured modal frequencies. Modal frequencies were predicted for 3 psi and 6 psi internal pressurization conditions in Configuration VI. The predictions were accomplished by applying differential stiffness to the elements with pressure loading and shielding beam elements with offsets from direct calculation by external superelements. The average disagreement between the measured and predicted differences for the 0 psi and 6 psi internal pressure conditions was less than 0.5% and the maximum disagreement was 1.2%. Similar agreement was obtained for the differences between the 0 psi and 3 psi internal pressure conditions.

Acoustic modal frequencies were predicted for the ATC interior as a hard-walled cavity with no damping applied. The predicted modal frequencies were compared with the results of an experimental acoustic survey of the interior cylinder. Reasonably good agreement was obtained for the thirty-four measured modes which, on the average, were within 2% of the predictions with a maximum discrepancy of 6.6% for the first acoustic mode.

Reasonable agreement was obtained when comparing the predicted and measured acoustic interior response due to force excitation at an acoustic or structural modal frequency. Comparisons were made for interior axial and cross-sectional data recovery meshes showing that the interior acoustic response is a composite of the participating structural and acoustic modal responses. Since the predicted and measured structural and acoustic modal frequencies sometimes vary by more than 10% the resulting interior predicted and measured acoustic responses was a manifestation of these variations.

11 ACKNOWLEDGEMENTS

The development and analysis in this study was performed under Contract NAS1-00135, Task Order 13RBF, "Structural Acoustic Modeling and Laboratory Support," Dr. Richard J. Silcox, Technical Monitor, National Aeronautics & Space Administration, Langley Research Center, Hampton, Virginia. Acknowledgments are extended to Dr. Ralph D. Buehrle (NASA Langley Structural Acoustics Branch), Jocelyn I. Pritchard and Richard S. Pappa (NASA Langley Structural Dynamics Branch) for conducting the experimental modal analyses, performing the interior acoustic survey, and post-processing the measured data.

12 REFERENCES

1. Elliott, S. J., Nelson, P. A., Stothers, I. M., and Boucher, C. C., "In-flight Experiments on the Active Control of Propeller-Induced Cabin Noise," *J. Sound and Vibration*, (140), 1990, pp. 219-238.
2. Grosveld, F. W., and Shepherd, K. P., "Active Sound Attenuation Across a Double Wall Structure," *Journal of Aircraft*, vol. 31, no. 1, January-February 1994, pp. 223-228.
3. Fuller, C. R., Snyder, S., Hansen C., and Silcox, R. J., "Active Control of Interior Noise in Model Aircraft Fuselages using Piezoceramic Actuators," *AIAA Journal*, vol. 30, no. 11, 1992, pp. 2613-2617.
4. Silcox, R. J., Lefebvre, S., Metcalf, V. L., Beyer, T. B., and Fuller, C. R., "Evaluation of Piezoceramic Actuators for Control of Aircraft Interior Noise," AIAA Paper No. 92-02-091, Proceedings of DGLR/AIAA 14th Aeroacoustics Conference, May 11-14, 1992, Aachen, Germany, Vol. II, pp. 542-551.

5. Lester, H. C. and Lefebvre, S., "Piezoelectric Actuators Models for Active Sound and Vibration Control of Cylinders," Proceedings of Recent Advances in Active Control of Sound and Vibration, Blacksburg, VA, April 15-17, 1991, pp. 3-26.
6. Cabell, R. H., Lester, H. C., and Silcox, R. J., "The Optimization of Force Inputs for Active Structural Acoustic Control using a Neural Network," Proceedings of Inter-Noise 92, Toronto, Ontario, Canada, vol. I, July 20-22, 1992, pp. 401-404.
7. Coats, T., Silcox, R. J., and Lester, H. C., "Numerical Study of Active Structural Acoustic Control in a Double-Walled Cylinder," Proceedings of Recent Advances in Active Control of Sound and Vibration, Blacksburg, VA, April 28-30, 1993.
8. Grosveld, F. W., Coats, T. J., Lester, H. C., and Silcox, R. J., "A Numerical Study of Active Structural Acoustic Control in a Stiffened, Double Wall Cylinder," Proceedings of NOISE-CON 94, National Conference on Noise Control Engineering, Ft. Lauderdale, FL, May 1-5, 1994, pp. 404-408.
9. Grosveld, Ferdinand W. and Lester, Harold C., "Numerical Study of Active Sound Transmission Control for Stiffened Double Wall Cylinders," 1995 International Symposium on Active Control of Sound and Vibration, ACTIVE 95, Newport Beach, California, July 06-08, 1995.
10. Grosveld, F. W., "Numerical Comparison of Active Acoustic and Structural Noise Control in a Stiffened Double Wall Cylinder," AIAA Paper 96-1722, 2nd AIAA/CEAS Aeroacoustics Conference, State College, PA, May 6-8, 1996.
11. Palumbo, D. L., Padula, S. L., Lyle, K. H., Cline, J. H., and Cabell, R. H., "Performance of Optimized Actuator and Sensor Arrays in an Active Noise Control System," AIAA Paper 96-1724, 2nd AIAA/CEAS Aeroacoustics Conference, State College, PA, May 6-8, 1996.
12. Fernholz, Christian M. and Robinson, Jay H., "Fully-Coupled Fluid/Structure Vibration Analysis Using MSC/NASTRAN," NASA TM 110215.
13. Cunefare, K., Crane, S., Engelstad, S., and Powell, E., "A Tool for Design Minimization of Aircraft Interior Noise," AIAA Paper 96-1702, 2nd AIAA/CEAS Aeroacoustics Conference, State College, PA, May 6-8, 1996.
14. Grosveld, F. W., "Structural Normal Mode Analysis of the Aluminum Testbed Cylinder," AIAA Paper 98-1949, Proceedings of the 39th AIAA/ASME/ASCE Structures, Structural Dynamics, and Materials Conference, Long Beach, CA, April 1998.
15. Fleming, G. A., Buehrle, R. D., and Storaasli, O. L., "Modal Analysis of an Aircraft Fuselage Panel Using Experimental and Finite Element Techniques," Proceedings of the 3rd International Conference on Vibration Measurements by Laser Techniques, Ancona, Italy, June 1998.
16. Pappa, R. S., Pritchard, J. I., and Buehrle, R. D., "Vibro-Acoustics Modal Testing at NASA Langley Research Center," NASA/TM-1999-209319, May 1999.
17. Buehrle, R. D., Fleming, G. A., Pappa, R. S., and Grosveld, F. W., "Finite Element Model Development and Validation for Aircraft Fuselage Structures," Proceedings of the 18th International Modal Analysis Conference, San Antonio, Texas, February 7-10, 2000.
18. Buehrle, R. D., Fleming, G. A., Pappa, R. S., and Grosveld, F. W., "Finite Element Model Development for Aircraft Fuselage Structures," Sound and Vibration Magazine, January 2001, Acoustical Publications, Inc.
19. Buehrle, Ralph D., Robinson, Jay H. and Grosveld, Ferdinand W., "Vibro-Acoustic Model Validation for a Curved Honeycomb Composite Panel," AIAA Paper 2001-1587, 42nd AIAA/ASME/ASCE/AHS/ASC Structures, Structural Dynamics, and Materials Conference, Seattle, WA, 16-19 April 2001.
20. Grosveld, Ferdinand W., Buehrle, Ralph D. and Robinson, Jay H., "Numerical and Acoustic Modeling of a Curved Composite Honeycomb Panel," AIAA Paper 2001-2277, 7th AIAA/CEAS Aeroacoustics Conference, Maastricht, Netherlands, 28-30 May, 2001.
21. Pritchard, Jocelyn, Pappa, Richard, and Buehrle, Ralph and Grosveld, Ferdinand, "Comparison of Modal Analysis Methods Applied to a Vibro-Acoustic Test Article," Proceedings of the International Modal Analysis Conference in Los Angeles, California, February 4-7, 2002.
22. Grosveld, Ferdinand W., Pritchard, Jocelyn, Buehrle, Ralph D. and Pappa, Richard S., "Finite Element Modeling of a the NASA Langley Aluminum Testbed Cylinder." AIAA Paper, 8th AIAA/CEAS Aeroacoustics Conference, Breckenridge, Colorado, 17-19 June, 2002.
23. Blevins, Robert D., "Formulas for Natural Frequency and Mode Shape," Krieger Publishing Company, Malabar, Florida, 1984.

13 TABLES

Table 1. Aluminum Testbed Cylinder configurations

Configuration	Stringers	Frames	End Rings	End Plates	Skin	Domes	Internal Pressure
I Bare Frame	●	●	●				
II Configuration I + End Plates	●	●	●	●			
III Configuration I + Skin	●	●	●		●		
IV Configuration III + End Plates	●	●	●	●	●		
V Configuration IV + Domes	●	●	●	●	●	●	
VI Configuration V + Pressure Loading	●	●	●	●	●	●	●

Table 2. Experimental modal frequencies of the ATC longitudinal stringer compared with predictions

Stringer Mode Shape	Measured Frequency	Beam Model Frequency	Beam Model Error	Solid Model Frequency	Solid Model Error	Updated Model Frequency	Updated Model Error
	[Hz]	[Hz]	[%]	[Hz]	[%]	[Hz]	[%]
x-z plane; j=1	8.8	9.09	3.2	9.10	3.4	9.15	3.9
y-z plane; j=1	9.4	9.77	4.0	9.70	3.2	9.72	3.4
x-z plane; j=2	24.5	25.03	2.2	25.07	2.3	25.20	2.9
y-z plane; j=2	26.0	26.90	3.5	26.12	0.5	25.89	-0.4
x-z plane; j=3	47.6	49.04	3.0	49.11	3.2	49.38	3.7
y-z plane; j=3	48.3	52.63	9.0	49.50	2.5	48.62	0.7
x-z plane; j=4	78.5	86.77	10.5	81.10	3.3	81.58	3.9
y-z plane; j=4	76.2	81.01	6.3	78.35	2.8	75.96	-0.3
x-z plane; j=5	117.2	129.19	10.2	120.98	3.2	121.79	3.9
y-z plane; j=5	109.0	120.91	10.9	111.53	2.3	106.60	-2.2
x-z plane; j=6	163.0	179.12	10.3	168.64	3.5	169.96	4.3
y-z plane; j=6	145.0	168.72	16.4	148.53	2.4	139.83	-3.6

Table 3. Experimental modal frequencies of the ATC ring frame compared with predictions

Ring frame Mode shape	Measured Frequency	Beam Model Frequency	Beam Model Error	Solid Model Frequency	Solid Model Error	Hybrid Model Frequency	Hybrid Model Error	Updated Model Frequency	Updated Model Error
	[Hz]	[Hz]	[%]	[Hz]	[%]	[Hz]	[%]	[Hz]	[%]
Out-of-Plane	9.8	14.0	42.4	9.6	-2.1	10.1	2.9	10.5	6.7
n=2	9.8	14.0	42.4	9.6	-2.1	10.1	2.9	10.5	6.7
Out-of-Plane	31.5	45.3	43.8	30.9	-1.8	32.3	2.7	33.2	5.6
n=3	31.5	45.3	43.8	30.9	-1.8	32.3	2.7	33.2	5.6
Out-of-Plane	63.5	91.0	43.4	62.4	-1.7	65.2	2.7	66.4	4.7
n=4	63.5	91.0	43.4	62.4	-1.7	65.2	2.7	66.4	4.7
Out-of-Plane	104.8	147.6	40.8	102.6	-2.1	107.4	2.5	108.4	3.5
n=5	104.8	147.6	40.8	102.6	-2.1	107.4	2.5	108.4	3.5
Out-of-Plane	153.7	211.2	37.4	150.0	-2.4	157.8	2.6	157.5	2.4
n=6	153.7	211.2	37.4	150.0	-2.4	157.8	2.6	157.5	2.4
In-Plane	34.3	45.5	32.7	32. 8	-4.4	36. 9	7.6	35.6	3.9
i=2	34.3	45.5	32.7	32. 8	-4.4	36. 9	7.6	35.6	3.9
In-Plane	98.0	129.3	32.0	93. 7	-4.4	104. 8	7.0	101.4	3.6
i=3	98.0	129.3	32.0	93. 7	-4.4	104. 8	7.0	101.4	3.6
In-Plane	186.3	246.4	32.3	178.4	-4.2	198.2	6.4	192.1	3.1
i=4	186.3	246.4	32.3	178.4	-4.2	198.2	6.4	192.1	3.1

Table 4. Experimental and numerical modal frequencies of the ATC Configuration I

Mode Number	Mode Shape	Measured Frequency	Measured Damping	Predicted Frequency	Error
[-]		[Hz]	[%]	[Hz]	[%]
1	First torsion mode	9.92		11.02	11.1
2	First x bending mode	16.29	0.35	18.72	14.9
3	First y bending mode	16.75	0.63	18.72	11.8
4	First x shearing mode	21.95	1.10	25.30	15.2
5	First y shearing mode	22.55	1.60	25.30	12.2
6	Second torsion mode	22.80		25.58	12.2
7	i=2, j=1 circumferential-axial mode (1 of 2)	29.36	0.19	29.69	1.1
8	i=2, j=1 circumferential-axial mode (2 of 2)	29.42	0.29	29.69	1.0
9	Second x bending mode	31.49	0.38	36.15	14.8
10	Second y bending mode	31.75	0.31	36.15	13.9
11	i=2, j=2 circumferential-axial mode (1 of 2)	34.21	0.31	35.56	4.0
12	i=2, j=2 circumferential-axial mode (2 of 2)	34.43	0.24	35.56	3.3
13	Third torsion mode	38.54	0.32	44.35	15.1
14	i=2, j=3 circumferential-axial mode (1 of 2)	42.66	0.19	46.16	8.2
15	i=2, j=3 circumferential-axial mode (2 of 2)	42.97	0.24	46.17	7.4
16	i=2, j=4 circumferential-axial mode (1 of 2)	48.44	0.24	53.27	10.0
17	i=2, j=4 circumferential-axial mode (2 of 2)	49.68	0.26	53.27	7.2
18	Third x bending mode	47.30		53.93	14.0
19	Third y bending mode	47.82		53.93	12.8
20	i=2, j=5 circumferential-axial mode (1 of 2)	53.96		59.57	10.4
21	i=2, j=5 circumferential-axial mode (2 of 2)	55.12		59.57	8.1
22	Fourth torsion mode	59.16		67.31	13.8
23	i=2, j=6 circumferential-axial mode (1 of 2)	61.88		69.31	12.0
24	i=2, j=6 circumferential-axial mode (2 of 2)	62.97		69.31	10.1
???23	i=2, j=6 circumferential-axial mode (1 of 2)	72.55		69.31	
?????24	i=2, j=6 circumferential-axial mode (2 of 2)	73.23		69.31	
25	i=3, j=1 circumferential-axial mode (1 of 2)	77.91	0.35	78.00	0.1
26	i=3, j=1 circumferential-axial mode (2 of 2)	78.742	0.32	78.00	-0.9
27	Fourth x bending mode	69.51		79.16	13.9
28	Fourth y bending mode	70.09		79.17	12.9
29	i=3, j=2 circumferential-axial mode (1 of 2)	81.06	0.38	80.64	-0.5
30	i=3, j=2 circumferential-axial mode (2 of 2)	82.18	0.31	80.64	-1.9
31				81.26	
32				81.26	
33	i=3, j=3 circumferential-axial mode (1 of 2)	85.64	0.28	87.22	1.8
34	i=3, j=3 circumferential-axial mode (2 of 2)	86.40		87.22	1.0
35	Fifth torsion mode	83.19		94.73	13.9

Table 4. Experimental and numerical modal frequencies of the ATC Configuration I (continued)

Mode Number	Mode Shape	Measured Frequency	Measured Damping	Predicted Frequency	Error
[-]		[Hz]	[%]	[Hz]	[%]
36	i=3, j=4 circumferential-axial mode (1 of 2)	95.64		99.824	4.4
37	i=3, j=4 circumferential-axial mode (2 of 2)	96.75		99.824	3.2
38		90.15	0.23	102.72	14.0
39		90.57	0.21	102.72	13.4
40	Fifth x bending mode	93.62		108.68	16.1
41	Fifth y bending mode	94.14		108.68	15.4
42	i=3, j=5 circumferential-axial mode (1 of 2)	110.99		120.12	8.2
43	i=3, j=5 circumferential-axial mode (2 of 2)	113.15		120.12	6.2
44	Sixth torsion mode	108.52		126.64	16.7
45	i=2, j=8 circumferential-axial mode (1 of 2)	119.98		137.17	14.3
46	i=2, j=8 circumferential-axial mode (2 of 2)	120.17		137.17	14.2
47	i=3, j=6 circumferential-axial mode (1 of 2)	129.40		139.91	8.1
48	i=3, j=6 circumferential-axial mode (2 of 2)	129.87		139.91	7.7
49	i=4, j=1 circumferential-axial mode (1 of 2)	143.53		142.55	-0.7
50	i=4, j=1 circumferential-axial mode (2 of 2)	144.41		142.55	-1.3
51	Sixth x bending mode	123.94	0.18	143.38	15.7
52	Sixth y bending mode	124.62	0.19	143.38	15.1
53	i=4, j=2 circumferential-axial mode (1 of 2)	145.96		144.46	-1.0
54	i=4, j=2 circumferential-axial mode (2 of 2)	147.64		144.46	-2.2
55				148.47	
56				148.47	
57	i=3, j=7 circumferential-axial mode (1 of 2)	140.48		156.10	11.1
58	i=3, j=7 circumferential-axial mode (2 of 2)	140.48		156.10	11.1
59				157.09	
60				157.09	
61	Seventh torsion mode	139.42		162.33	16.4

Table 5. Experimental and numerical modal frequencies of the ATC Configuration III

Mode Number	Mode Shape	Measured Frequency	Measured Damping	Predicted Frequency	Error
[-]		[Hz]	[%]	[Hz]	[%]
1	i=2, j=0 Rayleigh mode (1 of 2)	50.82	0.43	54.648	7.5
2	i=2, j=0 Rayleigh mode (2 of 2)	51.18	0.11	54.648	6.8
3	i=2, j=0 Love mode (1 of 2)	53.46	0.79	57.688	7.9
4	i=2, j=0 Love mode (2 of 2)	54.29	0.18	57.688	6.3
5	i=2, j=1 circumferential-axial mode (1 of 2)	100.15	0.57	110.73	10.6
6	i=2, j=1 circumferential-axial mode (2 of 2)	102.12	0.27	110.73	8.4
7	i=3, j=1 circumferential-axial mode (1 of 2)	141.38	0.28	148.59	5.1
8	i=3, j=1 circumferential-axial mode (2 of 2)	142.35	0.34	148.59	4.4
9	i=3, j=2 circumferential-axial mode (1 of 2)	152.39	0.49	161.92	6.3
10	i=3, j=2 circumferential-axial mode (2 of 2)	152.41	0.23	161.92	6.2
11	i=3, j=3 circumferential-axial mode (1 of 2)	160.10	0.29	172.43	7.7
12	i=3, j=3 circumferential-axial mode (2 of 2)	161.83	0.15	172.43	6.6
13	i=3, j=4 circumferential-axial mode (1 of 2)	183.55	0.32	198.93	8.4
14	i=3, j=4 circumferential-axial mode (2 of 2)			198.93	
15	i=2, j=2 circumferential-axial mode (1 of 2)	204.34	1.56	230.12	12.6
16	i=2, j=2 circumferential-axial mode (2 of 2)	207.15	1.26	230.12	11.1
17	First x bending mode (1 of 2)	224.56	0.65	232.13	3.4
18	First x bending mode (2 of 2)			232.13	
19	First breathing mode			241.79	
20	i=3, j=5 circumferential-axial mode (1 of 2)	233.72	0.69	260.51	11.5
21	i=3, j=5 circumferential-axial mode (2 of 2)	235.01	1.10	260.51	10.9
22	i=4, j=1 circumferential-axial mode (1 of 2)	261.19	0.50	267.71	2.5
23	i=4, j=1 circumferential-axial mode (2 of 2)	263.97	0.65	267.71	1.4
24	i=4, j=2 circumferential-axial mode (1 of 2)	267.89	0.44	276.21	3.1
25	i=4, j=2 circumferential-axial mode (2 of 2)	270.69	0.63	276.21	2.0
26	i=4, j=3 circumferential-axial mode (1 of 2)	282.51	0.49	296.03	4.8
27	i=4, j=3 circumferential-axial mode (2 of 2)	284.90	0.55	296.03	3.9
28	i=4, j=4 circumferential-axial mode (1 of 2)	299.60	0.57	319.63	6.7
29	i=4, j=4 circumferential-axial mode (2 of 2)	301.95	0.43	319.63	5.9
30	i=4, j=5 circumferential-axial mode (1 of 2)	313.02	0.32	332.83	6.3
31	i=4, j=5 circumferential-axial mode(2 of 2)			332.83	
32	i=3, j=6 circumferential-axial mode (1 of 2)	294.04	1.11	334.28	13.7
33	i=3, j=6 circumferential-axial mode (2 of 2)	296.09	0.75	334.28	12.9
34	i=4, j=6 circumferential-axial mode (1 of 2)	380.35	0.35	349.50	
35	i=4, j=6 circumferential-axial mode (2 of 2)			349.50	

Table 5. Experimental and numerical modal frequencies of the ATC Configuration III (continued)

Mode Number	Mode Shape	Measured Frequency	Measured Damping	Predicted Frequency	Error
[-]		[Hz]	[%]	[Hz]	[%]
36	i=2, j=3 radial-axial mode (1 of 2)			356.05	
37	i=2, j=3 radial-axial mode (2 of 2)			356.05	
38	First panel mode on i=1, j=1			367.33	
39	First panel mode on i=1, j=2			370.98	
40	First panel mode on i=2, j=1 (1 of 2)			371.30	
41	First panel mode on i=2, j=1 (2 of 2)			371.30	
42	First panel mode on i=2, j=2 (1 of 2)			374.80	
43	First panel mode on i=2, j=2 (2 of 2)			374.80	
44	First panel mode on i=1, j=3			376.92	
45	First panel mode on i=2, j=3 (1 of 2)			380.51	
46	First panel mode on i=2, j=3 (2 of 2)			380.51	
47	First panel mode on i=4, j=1 (1 of 2)			382.49	
48	First panel mode on i=4, j=1 (2 of 2)			382.49	
49	i=4, j=7 radial-axial mode (1 of 2)			383.38	
50	i=4, j=7 radial-axial mode (2 of 2)			383.38	
51	First panel mode on i=1, j=4			384.81	
52	First panel mode on i=4, j=2 (1 of 2)			386.02	
53	First panel mode on i=4, j=2 (2 of 2)			386.02	
54	First panel mode on i=2, j=4 (1 of 2)			388.15	
55	First panel mode on i=2, j=4 (2 of 2)			388.15	
56	First panel mode on first breathing mode			388.31	
57	First panel mode on i=1, j=5 (1 of 2)			390.44	
58	First panel mode on i=1, j=5 (2 of 2)			390.44	
59	First panel mode on i=4, j=3 (1 of 2)			391.19	
60	First panel mode on i=4, j=3 (2 of 2)			391.19	
61	First panel mode on i=1, j=6			394.11	
62	First panel mode on i=3, j=1 (1 of 2)			395.79	
63	First panel mode on i=3, j=1 (2 of 2)			395.79	
64	First panel mode on i=2, j=5 (1 of 2)			397.20	
65	First panel mode on i=2, j=5 (2 of 2)			397.20	
66	First panel mode on i=5, j=1 (1 of 2)			397.55	
67	First panel mode on i=5, j=1 (2 of 2)			397.55	
68	i=5, j=1 radial-axial mode (1 of 2)			397.94	
69	i=5, j=1 radial-axial mode (2 of 2)			397.94	
70	First panel mode on i=4, j=4 (1 of 2)			398.12	

Table 6. Experimental modal frequencies of the longitudinal stringer compared with predictions for the updated finite element model (Table 2) and the enhanced model

Stringer Mode shape	Measured Frequency	Predicted Frequency Updated Stringer Model	Error	Predicted Frequency Enhanced Model	Error
	(Hz)	(Hz)	%	(Hz)	%
x-z plane; j=1	8.8	9.15	3.9	9.05	2.8
y-z plane; j=1	9.4	9.72	3.4	9.75	3.7
x-z plane; j=2	24.5	25.20	2.9	24.94	1.8
y-z plane; j=2	26	25.89	-0.4	26.01	0.0
x-z plane; j=3	47.6	49.38	3.7	48.86	2.6
y-z plane; j=3	48.3	48.62	0.7	48.78	1.0
x-z plane; j=4	78.5	81.58	3.9	80.69	2.8
y-z plane; j=4	76.2	75.96	-0.3	76.26	0.1
x-z plane; j=5	117.2	121.79	3.9	120.39	2.7
y-z plane; j=5	109	106.60	-2.2	107.22	-1.6
x-z plane; j=6	163	169.96	4.3	167.87	3.0
y-z plane; j=6	145	139.83	-3.6	141.03	-2.7

Table 7. Experimental modal frequencies of the ring frame compared with predictions for the updated finite element model (Table 3) and the enhanced model

Ring Frame Mode Shape	Measured Frequency	Predicted Frequency Updated Ring Frame Model	Error	Predicted Frequency Enhanced Model	Error
	[Hz]	[Hz]	[%]		[%]
Out-of-Plane, n=2	9.84	10.50	6.7	9.79	-0.5
	9.84	10.50	6.7	9.79	-0.5
Out-of-Plane, n=3	31.47	33.22	5.6	31.24	-0.7
	31.47	33.22	5.6	31.24	-0.7
Out-of-Plane, n=4	63.49	66.44	4.7	62.81	-1.1
	63.49	66.44	4.7	62.81	-1.1
Out-of-Plane, n=5	104.81	108.44	3.5	102.8	-1.9
	104.81	108.44	3.5	102.8	-1.9
Out-of-Plane, n=6	153.73	157.46	2.4	149.71	-2.6
	153.73	157.46	2.4	149.73	-2.6
In-Plane, i=2	34.3	35.64	3.9	33.81	-1.4
	34.3	35.64	3.9	33.81	-1.4
In-Plane, i=3	97.95	101.44	3.6	96.26	-1.7
	97.95	101.44	3.6	96.26	-1.7
In-Plane, i=4	186.29	192.11	3.1	182.65	-2.0
	186.29	192.11	3.1	182.65	-2.0

Table 8. S-fiberglass, epoxy matrix and lamina composite mechanical properties

Property	Units	S-fiberglass		Epoxy matrix		Lamina composite	
Elasticity modulus	[psi]	E_f =	12,398,000	E_m =	500,000	E_{11} =	6,449,000
Elasticity modulus	[psi]					E_{22} =	1,698,000
Shear modulus	[psi]	G_f =	7,947,000	G_m =	357,100	G_{12} =	683,600
Poisson's ratio	[-]	v_f =	0.22	v_m =	0.30	v_{12} =	0.276
Volume percentage	[-]	V_f =	0.5	V_m =	0.5	V_c =	1.0
Specific weight	[pci]	$g\rho_f$ =	0.090	$g\rho_m$ =	0.045	$g\rho_c$ =	0.067

Table 9. Dome fiberglass laminate stacking sequence

Sequence	Material	Thickness	Orientation
[-]		[in]	[deg]
1	Fiberglass	0.004	0
2	Fiberglass	0.004	45
3	Fiberglass	0.026	0
4	Fiberglass	0.026	45
5	Fiberglass	0.026	0
6	Fiberglass	0.026	45
7	Fiberglass	0.026	0
8	Fiberglass	0.026	45
9	Fiberglass	0.026	0
10	Fiberglass	0.026	45
11	Fiberglass	0.026	0

Table 10. Experimental modal frequencies of the ATC dome compared with predictions

Mode Number	Mode Shape	Measured Frequency	Predicted Frequency	Error
[-]		[Hz]	[Hz]	[%]
1	i=2 circumferential mode (1 of 2)	21.6	21.34	-1.2
2	i=2 circumferential mode (2 of 2)	21.6	21.40	-0.9
3	i=3 circumferential mode (1 of 2)	68.7	64.82	-5.6
4	i=3 circumferential mode (2 of 2)	68.7	64.83	-5.6
5	i=4 circumferential mode (1 of 2)	135.5	129.30	-4.6
6	i=4 circumferential mode (2 of 2)	135.5	129.42	-4.5
7	i=5 circumferential mode (1 of 2)	224.0	213.50	-4.7
8	i=5 circumferential mode (2 of 2)	224.0	213.54	-4.7
9	i=6 circumferential mode (1 of 2)	321.6	315.95	-1.8
10	i=6 circumferential mode (2 of 2)	321.6	315.98	-1.7

Table 11. Experimental and numerical modal frequencies of the Configuration I for stringer/ring frame connected by various number of nodes and different node locations

Mode Number	Mode Shape	Measured Modal Frequency	Error Predicted Unenhanced (12 nodes)	Predicted Modal Frequency Enhanced (30-node)	Error	Predicted Modal Frequency Enhanced (6-node)	Error
[-]		[Hz]	[%]	[Hz]	[%]	[Hz]	[%]
1	First torsion mode	9.92	11.1	7.55	-23.9	10.12	2.0
2	First x bending mode	16.29	14.9	14.14	-13.2	17.51	7.5
3	First y bending mode	16.75	11.8	14.14	-15.6	17.51	4.5
4	First x shearing mode	21.95	15.2	17.5	-20.3	23.44	6.8
5	First y shearing mode	22.55	12.2	17.5	-22.4	23.44	3.9
6	Second torsion mode	22.80	12.2	18.63	-18.3	23.74	4.1
7	i=2, j=1 circumferential-axial mode (1 of 2)	29.36	1.1	26.65	-9.2	28.18	-4.0
8	i=2, j=1 circumferential-axial mode (2 of 2)	29.42	1.0	26.65	-9.4	28.18	-4.2
9	Second x bending mode	31.49	14.8	29.36	-6.8	34.08	7.4
10	Second y bending mode	31.75	13.9	29.36	-7.5	34.08	6.5
11	i=2, j=2 circumferential-axial mode (1 of 2)	34.21	4.0	31.54	-7.8	33.82	-1.1
12	i=2, j=2 circumferential-axial mode (2 of 2)	34.43	3.3	31.54	-8.4	33.82	-1.8
13	Third torsion mode	38.54	15.1	34.28	-11.1	41.44	7.5
14	i=2, j=3 circumferential-axial mode (1 of 2)	42.66	8.2	42.29	-0.9	44.1	3.4
15	i=2, j=3 circumferential-axial mode (2 of 2)	42.97	7.4	42.29	-1.6	44.1	2.6
16	i=2, j=4 circumferential-axial mode (1 of 2)	48.44	10.0	49.89	3.0	51.09	5.5
17	i=2, j=4 circumferential-axial mode (2 of 2)	49.68	7.2	49.89	0.4	51.09	2.8

Table 12. Experimental and numerical modal frequencies of the Configuration III for stringer/ring frame connected by various number of nodes and different node locations

Mode Number	Mode Shape	Measured Modal Frequency	Error Predicted Unenhanced (12 nodes)	Predicted Modal Frequency Enhanced (30-node)	Error	Predicted Modal Frequency Enhanced (6-node)	Error
[-]		[Hz]	[%]	[Hz]	[%]	[Hz]	[%]
1	First bending (1 of 2)	14.03	7.5	11.82	-12.6	14.56	7.7
2	First bending (2 of 2)	14.03	6.8	11.82	-14.1	14.56	5.8
3	Second bending ? (1 of 2)	18.40	7.9	14.40	-22.7	19.32	3.8
4	Second bending ? (2 of 2)	18.40	6.3	14.40	-23.4	19.32	2.8
5	First torsion	19.84	10.6	16.32	-16.7	20.69	5.6
6	Second bending (1 of 2)	29.63	8.4	26.40	-5.7	30.47	8.9
7	Second bending (2 of 2)	29.63	5.1	26.40	-6.1	30.47	8.4
8	i=2, j=1 circumferential-axial mode (1 of 2)	28.12	4.4	26.73	-9.3	28.31	-3.9
9	i=2, j=1 circumferential-axial mode (2 of 2)	28.12	6.3	26.73	-9.5	28.31	-4.1
10	i=2, j=2 circumferential-axial mode (1 of 2)	34.29	6.2	32.33	-7.0	34.62	-0.4
11	i=2, j=2 circumferential-axial mode (2 of 2)	34.29	7.7	32.33	-7.7	34.62	-1.1
12	Second torsion	37.54	6.6	32.19	-11.0		
13	i=2, j=3 circumferential-axial mode (1 of 2)	47.64	8.4	45.44	-1.8	48.1	4.0
14	i=2, j=3 circumferential-axial mode (2 of 2)	47.64		45.44	-2.0	48.1	3.8
15	Third torsion	59.24	12.6	51.81	-9.3	61.08	7.0
16	i=2, j=4 circumferential-axial mode (1 of 2)	66.63	11.1	64.14	2.9	67.24	7.9

Table 13. Experimental and numerical modal frequencies of the refined and unrefined 12-node Configuration I

Mode Number	Mode Shape	Measured Modal Frequency	Predicted Modal Frequency Refined (12-node)	Error	Error ((Table 4) Unrefined (12-node)
[-]		[Hz]	[Hz]	[%]	[%]
1	First torsion mode	9.92	9.66	-2.6	11.1
2	First x bending mode	16.29	16.86	3.5	14.9
3	First y bending mode	16.75	16.86	0.7	11.8
4	First x shearing mode	21.95	22.33	1.7	15.2
5	First y shearing mode	22.55	22.33	-1.0	12.2
6	Second torsion mode	22.80	22.73	-0.3	12.2
7	i=2, j=1 circumferential-axial mode (1 of 2)	29.36	28.00	-4.6	1.1
8	i=2, j=1 circumferential-axial mode (2 of 2)	29.42	28.00	-4.8	1.0
9	Second x bending mode	31.49	33.11	5.1	14.8
10	Second y bending mode	31.75	33.11	4.3	13.9
11	i=2, j=2 circumferential-axial mode (1 of 2)	34.21	33.49	-2.1	4.0
12	i=2, j=2 circumferential-axial mode (2 of 2)	34.43	33.49	-2.7	3.3
13	Third torsion mode	38.54	39.96	3.7	15.1
14	i=2, j=3 circumferential-axial mode (1 of 2)	42.66	43.82	2.7	8.2
15	i=2, j=3 circumferential-axial mode (2 of 2)	42.97	43.82	2.0	7.4
16	i=2, j=4 circumferential-axial mode (1 of 2)	48.44	50.91	5.1	10.0
17	i=2, j=4 circumferential-axial mode (2 of 2)	49.68	50.91	2.5	7.2
18	Third x bending mode	47.30	50.05	5.8	14.0
19	Third y bending mode	47.82	50.05	4.7	12.8
20	i=2, j=5 circumferential-axial mode (1 of 2)	53.96	56.89	5.4	10.4
21	i=2, j=5 circumferential-axial mode (2 of 2)	55.12	56.89	3.2	8.1
22	Fourth torsion mode	59.16	61.42	3.8	13.8
23	i=2, j=6 circumferential-axial mode (1 of 2)	61.88	65.16	5.3	12.0
24	i=2, j=6 circumferential-axial mode (2 of 2)	62.97	65.16	3.5	10.1
23	i=2, j=6 circumferential-axial mode (1 of 2)	72.55			
24	i=2, j=6 circumferential-axial mode (2 of 2)	73.23			
25	i=3, j=1 circumferential-axial mode (1 of 2)	77.91	73.75	-5.3	0.1
26	i=3, j=1 circumferential-axial mode (2 of 2)	78.742	73.75	-6.3	-0.9
27	Fourth x bending mode	69.51	74.18	6.7	13.9
28	Fourth y bending mode	70.09	74.18	5.8	12.9
29	i=3, j=2 circumferential-axial mode (1 of 2)	81.06	76.36	-5.8	-0.5
30	i=3, j=2 circumferential-axial mode (2 of 2)	82.18	76.36	-7.1	-1.9
31					
32					
33	i=3, j=3 circumferential-axial mode (1 of 2)	85.64	82.58	-3.6	1.8
34	i=3, j=3 circumferential-axial mode (2 of 2)	86.40	82.58	-4.4	1.0
35	Fifth torsion mode	83.19	87.32	5.0	13.88

Table 13. Experimental and numerical modal frequencies of the refined and unrefined 12-node Configuration I (continued)

Mode Number	Mode Shape	Measured Modal Frequency	Predicted Modal Frequency Refined (12-node)	Error	Error (Table 4) Unrefined (12-node)
[-]		[Hz]	[Hz]	[%]	[%]
36	i=3, j=4 circumferential-axial mode (1 of 2)	95.64	94.78	-0.9	4.4
37	i=3, j=4 circumferential-axial mode (2 of 2)	96.75	94.79	-2.0	3.2
38		90.15	97.86	8.6	14.0
39		90.57	97.86	8.0	13.4
40	Fifth x bending mode	93.62	102.31	9.3	16.1
41	Fifth y bending mode	94.14	102.32	8.7	15.4
42	i=3, j=5 circumferential-axial mode (1 of 2)	110.99	114.28	3.0	8.2
43	i=3, j=5 circumferential-axial mode (2 of 2)	113.15	114.28	1.0	6.2
44	Sixth torsion mode	108.52	117.53	8.3	16.7
45	i=2, j=8 circumferential-axial mode (1 of 2)	119.98	130.57	8.8	14.3
46	i=2, j=8 circumferential-axial mode (2 of 2)	120.17	130.57	8.7	14.2
47	i=3, j=6 circumferential-axial mode (1 of 2)	129.40	134.19	3.7	8.1
48	i=3, j=6 circumferential-axial mode (2 of 2)	129.87	134.19	3.3	7.7
49	i=4, j=1 circumferential-axial mode (1 of 2)	143.53	134.88	-6.0	-0.7
50	i=4, j=1 circumferential-axial mode (2 of 2)	144.41	134.88	-6.6	-1.3
51	Sixth x bending mode	123.94	135.22	9.1	15.7
52	Sixth y bending mode	124.62	135.22	8.5	15.1
53	i=4, j=2 circumferential-axial mode (1 of 2)	145.96	136.64	-6.4	-1.0
54	i=4, j=2 circumferential-axial mode (2 of 2)	147.64	136.65	-7.4	-2.2
55	i=4, j=3 circumferential-axial mode (1 of 2)		140.47		
56	i=4, j=3 circumferential-axial mode (2 of 2)		140.48		
57	i=4, j=4 circumferential-axial mode (1 of 2)		148.77		
58	i=4, j=4 circumferential-axial mode (2 of 2)		148.78		
59	i=3, j=7 circumferential-axial mode (1 of 2)	140.48	149.70	6.6	11.1
60	i=3, j=7 circumferential-axial mode (2 of 2)	140.48	149.70	6.6	11.1
61	Seventh torsion mode	139.42	149.86	7.5	16.4

Table 14. Experimental and numerical modal frequencies of the refined and unrefined 12-node Configuration III

Mode Number	Mode Shape	Measured Modal Frequency	Predicted Modal Frequency Refined (12-node)	Error	Error (Table 5) Unrefined (12-node)
[-]		[Hz]	[Hz]	[%]	[%]
1	i=2, j=0 Rayleigh mode (1 of 2)	50.82	52.43	3.2	7.5
2	i=2, j=0 Rayleigh mode (2 of 2)	51.18	52.43	2.4	6.8
3	i=2, j=0 Love mode (1 of 2)	53.46	56.26	5.2	7.9
4	i=2, j=0 Love mode (2 of 2)	54.29	56.26	3.6	6.3
5	i=2, j=1 circumferential-axial mode (1 of 2)	100.15	108.09	7.9	10.6
6	i=2, j=1 circumferential-axial mode (2 of 2)	102.12	108.09	5.8	8.4
7	i=3, j=1 circumferential-axial mode (1 of 2)	141.38	141.76	0.3	5.1
8	i=3, j=1 circumferential-axial mode (2 of 2)	142.35	141.76	-0.4	4.4
9	i=3, j=2 circumferential-axial mode (1 of 2)	152.39	157.15	3.1	6.3
10	i=3, j=2 circumferential-axial mode (2 of 2)	152.41	157.15	3.1	6.2
11	i=3, j=3 circumferential-axial mode (1 of 2)	160.10	169.00	5.6	7.7
12	i=3, j=3 circumferential-axial mode (2 of 2)	161.83	169.00	4.4	6.6
13	i=3, j=4 circumferential-axial mode (1 of 2)	183.55	192.89	5.1	8.4
14	i=3, j=4 circumferential-axial mode (2 of 2)		192.89		
15	i=2, j=2 circumferential-axial mode (1 of 2)	204.34	224.65	9.9	12.6
16	i=2, j=2 circumferential-axial mode (2 of 2)	207.15	224.66	8.5	11.1
17	First x bending mode (1 of 2)	224.56	228.73	1.9	3.4
18	First x bending mode (2 of 2)		228.73		
19	First breathing mode		237.07		
20	i=3, j=5 circumferential-axial mode (1 of 2)	233.72	251.09	7.4	11.5
21	i=3, j=5 circumferential-axial mode (2 of 2)	235.01	251.09	6.8	10.9
22	i=4, j=1 circumferential-axial mode (1 of 2)	261.19	258.44	-1.1	2.5
23	i=4, j=1 circumferential-axial mode (2 of 2)	263.97	258.45	-2.1	1.4
24	i=4, j=2 circumferential-axial mode (1 of 2)	267.89	266.50	-0.5	3.1
25	i=4, j=2 circumferential-axial mode (2 of 2)	270.69	266.51	-1.5	2.0
26	i=4, j=3 circumferential-axial mode (1 of 2)	282.51	285.72	1.1	4.8
27	i=4, j=3 circumferential-axial mode (2 of 2)	284.90	285.73	0.3	3.9
28	i=4, j=4 circumferential-axial mode (1 of 2)	299.60	310.88	3.8	6.7
29	i=4, j=4 circumferential-axial mode (2 of 2)	301.95	310.89	8.1	5.9
30	i=4, j=5 circumferential-axial mode (1 of 2)	313.02	326.48	4.3	6.3
31	i=4, j=5 circumferential-axial mode(2 of 2)		326.49		
32	i=3, j=6 circumferential-axial mode (1 of 2)	294.04	321.82	9.4	13.7
33	i=3, j=6 circumferential-axial mode (2 of 2)	296.09	321.82	8.7	12.9
34	i=4, j=6 circumferential-axial mode (1 of 2)		340.41		
35	i=4, j=6 circumferential-axial mode (2 of 2)		340.42		
36	i=2, j=3 circumferential-axial mode (1 of 2)		346.92		
37	i=2, j=3 circumferential-axial mode (2 of 2)		346.93		
38	First panel mode on i=1, j=1 global		348.18		
39	First panel mode on i=1, j=2 global		351.53		

Table 15. Experimental and numerical modal frequencies of the refined ATC Configuration II

Mode Number	Mode Shape	Measured Frequency	Measured Damping	Predicted Frequency	Error
[-]		[Hz]	[%]	[Hz]	[%]
1	First bending (1 of 2)	13.52	0.31	14.03	3.6
2	First bending (2 of 2)	13.76	0.29	14.03	2.0
3	Second bending ? (1 of 2)	18.62	0.58	18.40	-1.2
4	Second bending ? (2 of 2)	18.79	0.37	18.40	-2.1
5	First torsion	19.60	0.44	19.84	1.2
6	Second bending (1 of 2)	27.99	0.24	29.63	5.6
7	Second bending (2 of 2)	28.11	0.32	29.63	5.1
8	i=2, j=1 circumferential-axial mode (1 of 2)	29.46	0.21	28.12	-4.8
9	i=2, j=1 circumferential-axial mode (2 of 2)	29.53	0.28	28.12	-5.0
10	i=2, j=2 circumferential-axial mode (1 of 2)	34.77	0.33	34.29	-1.4
11	i=2, j=2 circumferential-axial mode (2 of 2)	35.02	0.25	34.29	-2.1
12	Second torsion	36.17	0.31	37.54	3.7
13	i=2, j=3 circumferential-axial mode (1 of 2)	46.26	0.26	47.64	2.9
14	i=2, j=3 circumferential-axial mode (2 of 2)	46.35	0.23	47.64	2.7
15	Third bending (1 of 2)			47.93	
16	Third bending (2 of 2)			47.93	
17	Third torsion	57.10	0.3	59.24	3.6
18	i=2, j=4 circumferential-axial mode (1 of 2)	62.32	0.32	66.63	6.5
19	i=2, j=4 circumferential-axial mode (2 of 2)	62.94	0.29	66.63	5.5
20	Fourth bending (1 of 2)	67.02	0.25	72.06	7.0
21	Fourth bending (2 of 2)	67.69	0.24	72.06	6.0
22	i=3, j=1 circumferential-axial mode (1 of 2)	78.02	0.37	73.88	-5.6
23	i=3, j=1 circumferential-axial mode (2 of 2)	78.84	0.36	73.88	-6.7
24	i=3, j=2 circumferential-axial mode (1 of 2)	81.06	0.39	76.32	-6.2
25	i=3, j=2 circumferential-axial mode (2 of 2)	82.15	0.32	76.32	-7.6
26	i=3, j=3 circumferential-axial mode (1 of 2)	85.83	0.33	82.79	-3.7
27	i=3, j=3 circumferential-axial mode (2 of 2)	86.48	0.28	82.79	-4.5
28	i=2, j=5 circumferential-axial mode (1 of 2)	87.02	0.22	94.74	8.2
29	i=2, j=5 circumferential-axial mode (2 of 2)	87.27	0.19	94.74	7.9
30	Fifth bending (1 of 2)	91.42	0.18	100.56	9.1
31	Fifth bending (2 of 2)	91.96	0.2	100.56	8.6
32	i=3, j=4 circumferential-axial mode (1 of 2)	96.20	0.35	95.66	-0.6
33	i=3, j=4 circumferential-axial mode (2 of 2)	97.45	0.26	95.66	-1.9
34	Axial mode	103.87	1.27	96.36	-7.8
35	Fifth torsion	106.60	0.19	115.62	7.8
36	i=3, j=5 circumferential-axial mode (1 of 2)	112.31	0.38	116.31	3.4
37	i=3, j=5 circumferential-axial mode (2 of 2)	114.95	0.38	116.31	1.2
38	i=2, j=6 circumferential-axial mode (1 of 2)	117.16	0.22	128.24	8.6
39	i=2, j=6 circumferential-axial mode (2 of 2)	117.57	0.19	128.24	8.3

Table 15. Experimental and numerical modal frequencies of the refined ATC Configuration II (continued)

Mode Number	Mode Shape	Measured Frequency	Measured Damping	Predicted Frequency	Error
[-]		[Hz]	[%]	[Hz]	[%]
40	Sixth bending (1 of 2)	121.86	0.18	133.72	8.9
41	Sixth bending (2 of 2)	122.62	0.19	133.72	8.3
42	i=3, j=6 circumferential-axial mode (1 of 2)	135.97	0.3	143.86	5.5
43	i=3, j=6 circumferential-axial mode (2 of 2)	138.16	0.31	143.86	4.0
44	i=4, j=1 non-symmetric mode (1 of 2)	143.72	0.38	135.04	-6.4
45	i=4, j=1 non-symmetric mode (2 of 2)	144.53	0.49	135.05	-7.0
46	i=4, j=2 non-symmetric mode (1 of 2)	145.84	0.49	136.66	-6.7
47	i=4, j=2 non-symmetric mode (2 of 2)	147.63	0.44	136.67	-8.0
48	i=2, j=7 circumferential-axial mode (1 of 2)	149.36	0.21	163.51	8.7
49	i=2, j=7 circumferential-axial mode (2 of 2)	149.55	0.17	163.51	8.5
50	i=4, j=3 non-symmetric mode (1 of 2)	150.55	0.44	140.54	-7.1
51	i=4, j=3 non-symmetric mode (2 of 2)	152.51	0.4	140.54	-8.5
52	Seventh bending (1 of 2)	154.80	0.17	169.45	8.7
53	Seventh bending (2 of 2)	155.57	0.16	169.45	8.2
54	i=4, j=4 circumferential-axial mode (1 of 2)	157.00	0.45	148.92	-5.4
55	i=4, j=4 circumferential-axial mode (2 of 2)	157.23	0.38	148.94	-5.6
56	i=3, j=7 circumferential-axial mode (1 of 2 ?)	164.33	0.44	178.52	8.0
57	i=4, j=5 circumferential-axial mode (1 of 2)	167.84	0.44	163.66	-2.6
58	i=3, j=7 circumferential-axial mode (2 of 2 ?)	169.94	0.28	178.52	4.8
59	i=4, j=5 circumferential-axial mode (2 of 2)	171.19	0.62	163.68	-4.6
60	i=2, j=8 circumferential-axial mode ?	184.45	0.15	202.56	8.9
61	i=4, j=6 circumferential-axial mode ?	188.78	0.47	185.95	-1.5
62	Eighth torsion	198.68	0.13	216.92	8.4
63	i=3, j=8 circumferential-axial mode (1 of 2)	201.12	0.27	189.83	-6.0
64	i=3, j=8 circumferential-axial mode (2 of 2)	204.22	0.21	189.83	-7.6
65	i=4, j=7 circumferential-axial mode (1 of 2)	210.96	0.31	215.79	2.2
66	i=4, j=7 circumferential-axial mode (2 of 2)	211.78	0.44	215.79	1.9
67	Ninth bending ?	212.32	0.23	235.60	9.9
68	i=2, j=9 circumferential-axial mode ? (1 of 2)	213.70	0.17	235.91	9.4
69	i=2, j=9 circumferential-axial mode ? (2 of 2)	215.26	0.16	235.91	8.8
70	i=5, j=1 circumferential-axial mode ?	216.97	0.43	205.36	-5.7
71	i=5, j=1 non-symmetric mode	222.45	0.63	205.36	-8.3
72	i=5, j=2 circumferential-axial mode ?	224.54	0.6	206.84	-8.6
73	i=5, j=2 non-symmetric mode ?	226.44	0.54	206.85	-9.4
74	i=5, j=3 non-symmetric mode ?	228.49	0.43	209.51	-9.0
75	i=5, j=4 circumferential-axial mode	233.90	0.47	215.45	-8.6
76	i=3, j=9 circumferential-axial mode ?	234.51	0.23	217.93	-7.6
77	i=5, j=5 circumferential-axial mode (1 of 2)	239.06	0.51	215.45	-10.9
78	i=5, j=5 circumferential-axial mode (2 of 2)	242.21	0.57	226.45	-7.0
79	i=5, j=5 circumferential-axial mode ?	244.58	0.49	226.45	-8.0

Table 16. Experimental and numerical modal frequencies of the refined ATC Configuration IV

Mode Number	Mode Shape	Measured Frequency	Measured Damping	Predicted Frequency	Error
[-]		[Hz]	[%]	[Hz]	[%]
1	i=2, j=1 circumferential-axial mode (1 of 2)	73.58	0.28	80.41	9.3
2	i=2, j=1 circumferential-axial mode (2 of 2)	74.64	2.15	80.41	7.7
3	First axial	97.05	1.90		
4	i=3, j=1 circumferential-axial mode (1 of 2)	142.19	0.27	143.15	0.7
5	i=3, j=1 circumferential-axial mode (2 of 2)	143.27	0.72	143.16	-0.1
6	First x-bending	152.94	0.96	176.20	15.2
7	First y-bending			176.20	
8	i=3, j=2 circumferential-axial mode (1 of 2)	167.85	0.32	175.42	4.5
9	i=3, j=2 circumferential-axial mode (2 of 2)	169.91	0.76	175.42	3.2
10	First torsion			180.49	
11	i=2, j=2 circumferential-axial mode (1 of 2)	174.75	1.41	195.41	11.8
12	i=2, j=2 circumferential-axial mode (2 of 2)			195.41	
13	First xy-bending	195.66	0.41		
14	i=3, j=3 circumferential-axial mode (1 of 2)	219.34	0.67	238.71	8.8
15	i=3, j=3 circumferential-axial mode (2 of 2)	221.67	0.79	238.71	7.7
16	i=4, j=1 circumferential-axial mode (1 of 2)	261.30	0.64	258.69	-1.0
17	i=4, j=1 circumferential-axial mode (2 of 2)	264.04	0.44	258.69	-2.0
18	i=4, j=2 circumferential-axial mode (1 of 2)	268.20	0.55	267.57	-0.2
19	i=4, j=2 circumferential-axial mode (2 of 2)	271.36	0.49	267.57	-1.4
20	i=3, j=4 circumferential-axial mode (1 of 2)	280.33	1.23	312.30	11.4
21	i=3, j=4 circumferential-axial mode (2 of 2)	283.55	2.33	312.30	10.1
22	i=4, j=3 circumferential-axial mode (1 of 2)	285.68	0.72	288.98	1.2
23	i=4, j=3 circumferential-axial mode (2 of 2)	288.21	0.57	288.98	0.3
24	Second x-bending			321.63	
25	Second y-bending			321.63	
26	i=2, j=3 circumferential-axial mode (1 of 2)	307.18	0.34	323.15	5.2
27	i=2, j=3 circumferential-axial mode (2 of 2)			323.15	
28	i=4, j=4 circumferential-axial mode (1 of 2)	312.82	0.62	322.34	3.0
29	i=4, j=4 circumferential-axial mode (2 of 2)	314.14	0.42	322.34	2.6
30	First panel mode on i=1, j=1 global			348.22	
31	First panel mode on i=1, j=2 global			351.68	
32	First panel mode on i=2, j=1 (1 of 2)			352.00	
33	First panel mode on i=2, j=1 (2 of 2)			352.00	
34	First panel mode on i=2, j=2 (1 of 2)			355.37	
35	First panel mode on i=2, j=2 (2 of 2)			355.37	
36	First panel mode on i=1, j=3 global			357.04	
37	First panel mode on i=2, j=3 (1 of 2)			360.56	
38	First panel mode on i=2, j=3 (2 of 2)			360.56	
39	i=4, j=4 circumferential-axial mode (1 of 2)			361.74	
40	i=4, j=4 circumferential-axial mode (2 of 2)			361.74	
41	First panel mode on i=4, j=1 (1 of 2)			362.67	
42	First panel mode on i=4, j=1 (2 of 2)			362.67	

Table 16. Experimental and numerical modal frequencies of the refined ATC Configuration IV (continued)

Mode Number	Mode Shape	Measured Frequency	Measured Damping	Predicted Frequency	Error
[-]		[Hz]	[%]	[Hz]	[%]
43	First panel mode on i=1, j=4 global			363.77	
44	First panel mode on i=4, j=2 (1 of 2)			366.07	
45	First panel mode on i=4, j=2 (2 of 2)			366.07	
46	First panel mode on i=2, j=4 (1 of 2)			367.06	
47	First panel mode on i=2, j=4 (2 of 2)			367.06	
48				367.83	
49				367.83	
50	First panel mode on i=4, j=3 (1 of 2)			370.93	
51	First panel mode on i=4, j=3 (2 of 2)			370.95	
52	First panel mode on i=1, j=5 global			371.20	
53	First panel mode on i=2, j=5 (1 of 2)			374.27	
54	First panel mode on i=2, j=5 (2 of 2)			374.27	
55	First panel mode on i=6, j=1 (1 of 2)			376.71	
56	First panel mode on i=6, j=1 (2 of 2)			376.71	
57	First panel mode on i=4, j=4 (1 of 2)			376.87	
58	First panel mode on i=4, j=4 (2 of 2)			376.89	
59	First panel mode on i=1, j=6 global			378.68	
60	First stringer mode on i=1, j=1 global			379.05	
61	i=3, j=5 circumferential-axial mode (1 of 2)			379.62	
62	i=3, j=5 circumferential-axial mode (2 of 2)			379.63	
63	First stringer mode on i=2, j=1 (1 of 2)			381.27	
64	First stringer mode on i=2, j=1 (2 of 2)			381.28	
65	First panel mode on i=2, j=6 (1 of 2)			381.54	
66	First panel mode on i=2, j=6 (2 of 2)			381.54	
67	First panel mode on i=6, j=2 (1 of 2)			381.69	
68	First panel mode on i=6, j=2 (2 of 2)			381.69	
69	First panel mode on i=2, j=7 (1 of 2)			383.42	
70	First panel mode on i=2, j=7 (2 of 2)			383.43	
71	First panel mode on i=1, j=7 global			385.59	
72	i=5, j=1 circumferential-axial mode (1 of 2)			386.48	
73	i=5, j=1 circumferential-axial mode (2 of 2)			386.49	
74				387.15	
75				387.15	
76				388.27	
77				388.27	
78				388.94	
79				388.97	
80				389.83	
81				389.86	
82	i=5, j=2 circumferential-axial mode (1 of 2)			389.95	
83	i=5, j=2 circumferential-axial mode (2 of 2)			389.95	
84				390.05	
85				390.07	

Table 16. Experimental and numerical modal frequencies of the refined ATC Configuration IV (continued)

Mode Number	Mode Shape	Measured Frequency	Measured Damping	Predicted Frequency	Error
[-]		[Hz]	[%]	[Hz]	[%]
86				391.40	
87				392.72	
88				392.73	
89				393.94	
90				393.94	
91				395.75	
92				396.07	
93				396.26	
94				396.28	
95				397.45	
96				397.49	
97	i=5, j=3 circumferential-axial mode (1 of 2)			398.04	
98	i=5, j=3 circumferential-axial mode (2 of 2)			398.04	
99				398.13	
100				398.13	
101				398.22	
102				398.22	
103				398.43	
104				398.44	
105				398.44	
106				399.52	
107				399.56	
108				400.85	
109				400.85	
110				401.52	
111				401.54	
112				402.62	
113				402.62	
114				404.12	
115				404.12	
116				404.96	
117				404.98	
118				405.56	
119				405.57	
120				405.93	
121				405.96	
122				406.58	
123				406.59	
124				408.06	
125				408.08	
126				408.52	
127				408.53	
128				409.46	
129				409.46	

Table 17. Experimental and numerical modal frequencies of the refined ATC Configuration V

Mode Number	Mode Shape	Measured Frequency	Measured Damping	Predicted Frequency	Error
[-]		[Hz]	[%]	[Hz]	[%]
1	i=2, j=1 circumferential-axial mode (1 of 2)	79.13	0.66	90.98	15.0
2	i=2, j=1 circumferential-axial mode (2 of 2)	79.91	0.71	91.06	14.0
3	First axial	92.92	1.14		
4	First x bending	123.17	0.89	137.59	11.7
5	First y bending	124.19	0.79	150.51	21.2
6	First torsion	141.57	1.01	149.75	5.8
7	i=3, j=1 circumferential-axial mode (1 of 2)	143.87	0.28	145.6	1.2
8	i=3, j=1 circumferential-axial mode (2 of 2)	145.06	0.60	145.6	0.4
9		148.41	1.00		
10	First xy-bending	151.99	0.69	264.53 ?	
11		158.15	1.13	264.55 ?	
12	i=2, j=2 circumferential-axial mode (1 of 2)	166.28	1.15	199.49	20.0
13	i=2, j=2 circumferential-axial mode (2 of 2)			199.56	
14	i=3, j=2 circumferential-axial mode (1 of 2)	170.47	0.35	179.99	5.6
15	i=3, j=2 circumferential-axial mode (2 of 2)	171.87	0.89	180	4.7
16	i=3, j=3 circumferential-axial mode (1 of 2)	220.34	1.01	242.15	9.9
17	i=3, j=3 circumferential-axial mode (2 of 2)	221.37	0.74	242.18	9.4
18	i=2, j=3 circumferential-axial mode (1 of 2)	259.34	1.26	321.46	24.0
19	i=2, j=3 circumferential-axial mode (2 of 2)			321.55	
20	i=4, j=1 circumferential-axial mode (1 of 2)	261.54	0.58	259.18	-0.9
21	i=4, j=1 circumferential-axial mode (2 of 2)	264.12	0.55	259.2	-1.9
22				264.53	
23				264.55	
24	i=4, j=2 circumferential-axial mode (1 of 2)	269.09	0.56	269.06	0.0
25	i=4, j=2 circumferential-axial mode (2 of 2)	272.20	0.67	269.08	-1.1
26	Second axial			282.35	
27	i=3, j=4 circumferential-axial mode (1 of 2)	280.25	1.35	314	12.0
28	i=3, j=4 circumferential-axial mode (2 of 2)			314.03	
29	i=4, j=3 circumferential-axial mode (1 of 2)	286.77	0.59	291.02	1.5
30	i=4, j=3 circumferential-axial mode (2 of 2)	289.28	0.67	291.04	0.6
31	i=4, j=4 circumferential-axial mode (1 of 2)			324.21	
32	i=4, j=4 circumferential-axial mode (2 of 2)			324.23	
33	Second y bending			328.25	
34	Second x bending			330.52	
35	First panel mode on i=1, j=1 global			348.31	
36	First panel mode on i=1, j=2			352.05	
37	First panel mode on i=2, j=1 (1 of 2)			352.09	
38	First panel mode on i=2, j=1 (2 of 2)			352.09	
39	First panel mode on i=, j= (1 of 2)			355.72	
40	First panel mode on i=, j= (1 of 2)			355.72	

Table 18. Experimental and numerical modal frequencies of the refined ATC Configuration V with gap

Mode Number	Mode Shape	Measured Frequency	Measured Damping	Predicted Frequency	Error	Previous Error
[-]		[Hz]	[%]	[Hz]	[%]	[%]
1	i=2, j=1 circumferential-axial mode (1 of 2)	79.13	0.66	86.55	9.2	15.0
2	i=2, j=1 circumferential-axial mode (2 of 2)	79.91	0.71	86.98	8.7	14.0
3	First axial	92.92	1.14			
4	First x bending	123.17	0.89	146.76	19.2	11.7
5	First y bending	124.19	0.79	147.59	18.9	21.2
6	First torsion	141.57	1.01	150.55	6.6	5.8
7	i=3, j=1 circumferential-axial mode (1 of 2)	143.87	0.28	144.22	0.2	1.2
8	i=3, j=1 circumferential-axial mode (2 of 2)	145.06	0.60	144.27	-0.6	0.4
9		148.41	1.00			
10	First xy-bending	151.99	0.69			
11				155.06		
12		158.15	1.13			
13	i=2, j=2 circumferential-axial mode (1 of 2)	166.28	1.15	199.40	19.8	20.0
14	i=2, j=2 circumferential-axial mode (2 of 2)			199.70		
15	i=3, j=2 circumferential-axial mode (1 of 2)	170.47	0.35	177.56	4.1	5.6
16	i=3, j=2 circumferential-axial mode (2 of 2)	171.87	0.89	177.67	3.3	4.7
17				198.44		
18	i=3, j=3 circumferential-axial mode (1 of 2)	220.34	1.01	240.56	9.1	9.9
19	i=3, j=3 circumferential-axial mode (2 of 2)	221.37	0.74	240.66	8.7	9.4
20				234.54		
21				238.52		
22				250.49		
23	i=2, j=3 circumferential-axial mode (1 of 2)	259.34	1.26	324.98	25.3	24.0
24	i=2, j=3 circumferential-axial mode (2 of 2)			325.08		
25	i=4, j=1 circumferential-axial mode (1 of 2)	261.54	0.58	258.89	-1.0	-0.9
26	i=4, j=1 circumferential-axial mode (2 of 2)	264.12	0.55	258.90	-2.0	-1.9
27				264.53		
28				264.55		
29	i=4, j=2 circumferential-axial mode (1 of 2)	269.09	0.56	268.17	-0.3	0.0
30	i=4, j=2 circumferential-axial mode (2 of 2)	272.20	0.67	268.19	-1.5	-1.1
31	second axial					
32				279.77		
33	i=3, j=4 circumferential-axial mode (1 of 2)	280.25	1.35	313.50	11.9	
34	i=3, j=4 circumferential-axial mode (2 of 2)			313.58		
35	i=4, j=3 circumferential-axial mode (1 of 2)	286.77	0.59	289.63	1.0	
36	i=4, j=3 circumferential-axial mode (2 of 2)	289.28	0.67	289.83	0.2	
37				292.21		
38	i=4, j=4 circumferential-axial mode (1 of 2)			323.16		
39	i=4, j=4 circumferential-axial mode (2 of 2)			323.19		
40	panel mode on i=0, j=1 global mode			348.23		
41	panel mode on i=0, j=2 global mode			351.75		

Table 18. Experimental and numerical modal frequencies of the refined ATC Configuration V with gap (continued 1)

Mode Number	Mode Shape	Measured Frequency	Measured Damping	Predicted Frequency	Error	Previous Error
[-]		[Hz]	[%]	[Hz]	[%]	[%]
42	panel mode on i=1, j=1 global mode (1 of 2)			352.02		
43	panel mode on i=1, j=1 global mode (2 of 2)			352.02		
44	panel mode on i=1, j=2 global mode (1 of 2)			355.44		
45	panel mode on i=1, j=2 global mode (1 of 2)			355.44		
46	panel mode on i=0, j=3 global mode (1 of 2)			357.19		
47	panel mode on i=0, j=3 global mode (2 of 2)			357.71		
48	panel mode on i=1, j=3 global mode (1 of 2)			360.70		
49	panel mode on i=1, j=3 global mode (2 of 2)			360.71		
50	i=4, j=5 circumferential-axial mode (1 of 2)			362.36		
51	i=4, j=5 circumferential-axial mode (2 of 2)			362.39		
52	panel mode on i=2, j=1 global mode (1 of 2)			362.68		
53	panel mode on i=2, j=1 global mode (2 of 2)			362.69		
54	panel mode on i=0, j=4 global mode			364.00		
55				365.84		
56	panel mode on i=2, j=2 global mode (1 of 2)			366.13		
57	panel mode on i=2, j=2 global mode (2 of 2)			366.14		
58	panel mode on i=1, j=4 global mode (1 of 2)			367.30		
59	panel mode on i=1, j=4 global mode (2 of 2)			367.31		
60	panel mode on i=2, j=3 global mode (1 of 2)			371.08		
61	panel mode on i=2, j=3 global mode (2 of 2)			371.09		
62	panel mode on i=0, j=5 global mode			371.52		
63	panel mode on i=1, j=5 global mode (1 of 2)			374.58		
64	panel mode on i=1, j=5 global mode (2 of 2)			374.60		
65				376.23		
66	panel mode on i=3, j=1 global mode (1 of 2)			376.72		
67	panel mode on i=3, j=1 global mode (2 of 2)			376.72		
68	panel mode on i=2, j=4 global mode (1 of 2)			377.12		
69	panel mode on i=2, j=4 global mode (2 of 2)			377.12		
70	panel mode on first torsion global mode			379.00		
71	panel mode on i=0, j=6 global mode			379.04		
72	stringer mode on i=0, j=1 global mode			379.07		
73	i=3, j=5 circumferential-axial mode (1 of 2)			380.30		
74	i=3, j=5 circumferential-axial mode (2 of 2)			380.34		
75	stringer mode on i=1, j=1 global mode (1 of 2)			381.29		
76	stringer mode on i=1, j=1 global mode (2 of 2)			381.30		
77	panel mode on i=3, j=2 global mode (1 of 2)			381.72		
78	panel mode on i=3, j=2 global mode (2 of 2)			381.73		
79	panel mode on i=1, j=6 global mode (1 of 2)			381.90		
80	panel mode on i=1, j=6 global mode (2 of 2)			381.91		
81				383.32		

Table 18. Experimental and numerical modal frequencies of the refined ATC Configuration V with gap (continued 2)

Mode Number	Mode Shape	Measured Frequency	Measured Damping	Predicted Frequency	Error	Previous Error
[-]		[Hz]	[%]	[Hz]	[%]	[%]
82	panel mode on i=2, j=5 global mode (1 of 2)			383.75		
83	panel mode on i=2, j=5 global mode (2 of 2)			383.76		
84	panel mode on i=0, j=7 global mode			385.94		
85	i=5, j=1 circumferential-axial mode (1 of 2)			386.54		
86	i=5, j=1 circumferential-axial mode (2 of 2)			386.54		
87	panel mode on i=3, j=3 global mode (1 of 2)			387.25		
88	panel mode on i=3, j=3 global mode (2 of 2)			387.26		
89	panel mode on i=1, j=7 global mode (1 of 2)			388.62		
90	panel mode on i=1, j=7 global mode (2 of 2)			388.64		
91	stringer mode on i=2, j=1 global mode (1 of 2)			388.97		
92	stringer mode on i=2, j=1 global mode (2 of 2)			389.00		
93	panel mode on i=4, j=1 global mode (1 of 2)			389.83		
94	panel mode on i=4, j=1 global mode (2 of 2)			389.87		
95	i=5, j=2 circumferential-axial mode (1 of 2)			390.13		
96	i=5, j=2 circumferential-axial mode (2 of 2)			390.15		
97	panel mode on i=2, j=6 global mode (1 of 2)			390.45		
98	panel mode on i=2, j=6 global mode (2 of 2)			390.46		
99	panel mode on i=0, j=8 global mode			391.68		
100	panel mode on i=3, j=4 global mode (1 of 2)			392.92		
101	panel mode on i=3, j=4 global mode (2 of 2)			392.93		
102	panel mode on i=1, j=8 global mode (1 of 2)			394.22		
103	panel mode on i=1, j=8 global mode (2 of 2)			394.24		
104	panel mode on i=0, j=9 global mode			395.91		
105	stringer mode on i=0, j=2 global mode			396.04		
106				396.30		
107	panel mode on i=2, j=7 global mode (1 of 2)			396.66		
108	panel mode on i=2, j=7 global mode (2 of 2)			396.72		
109	panel mode on i=4, j=2 global mode (1 of 2)			397.47		
110	panel mode on i=4, j=2 global mode (2 of 2)			397.50		
111	stringer mode on i=0, j=2 global mode (1 of 2)			398.20		
112	stringer mode on i=0, j=2 global mode (2 of 2)			398.21		
113	panel mode on i=1, j=9 global mode (1 of 2)			398.38		
114				398.38		
115	panel mode on i=1, j=9 global mode (2 of 2)			398.39		
116	panel mode on i=0, j=10			398.48		
117				398.54		
118	panel mode on i=3, j=5 global mode (1 of 2)			398.76		
119	panel mode on i=3, j=5 global mode (2 of 2)			398.77		
120				399.94		

Table 19. Experimental and numerical modal frequencies of the ATC Configuration VI (3 psi)

Mode Number	Mode Shape	Measured Frequency	Measured Damping	Predicted Frequency	Error
[-]		[Hz]	[%]	[Hz]	[%]
1	First z rotation	1.87	7.53		
2	First z rotation	9.53	4.48		
3		11.15	0.71		
4		28.23	0.36		
5	i=2, j=1 circumferential-axial mode (1 of 2)	81.46	0.52	88.66	8.8
6	i=2, j=1 circumferential-axial mode (2 of 2)			89.08	
7	First x bending	122.60	0.85	146.93	19.8
8	i=3, j=1 circumferential-axial mode (1 of 2)	147.41	0.38	147.93	0.4
9	i=3, j=1 circumferential-axial mode (2 of 2)	148.57	0.58	148.12	-0.3
10	First torsional			150.61	
11	i=3, j=2 circumferential-axial mode (1 of 2)	168.78	1.74	180.93	7.2
12	i=3, j=2 circumferential-axial mode (2 of 2)	173.68	0.56	181.03	4.2
13	i=2, j=2 circumferential-axial mode (1 of 2)			200.92	
14	i=2, j=2 circumferential-axial mode (2 of 2)			201.16	
15	i=3, j=3 circumferential-axial mode (1 of 2)	223.42	0.19	244.06	9.2
16	i=3, j=3 circumferential-axial mode (2 of 2)			244.07	
17	i=4, j=1 circumferential-axial mode (1 of 2)	265.38	0.70	262.90	-0.9
18	i=4, j=1 circumferential-axial mode (2 of 2)	268.51	0.67	262.91	-2.1
19	i=4, j=2 circumferential-axial mode (1 of 2)	273.18	0.93	272.23	-0.3
20	i=4, j=2 circumferential-axial mode (2 of 2)	276.45	0.63	272.24	-1.2
21	i=3, j=4 circumferential-axial mode (1 of 2)	284.09	1.59	318.62	11.8
22	i=3, j=4 circumferential-axial mode (2 of 2)			318.70	
23	i=4, j=3 circumferential-axial mode (1 of 2)	293.62	0.83	294.14	0.2
24	i=4, j=3 circumferential-axial mode (2 of 2)			294.51	
25	i=4, j=4 circumferential-axial mode (1 of 2)	318.43	0.68	328.44	3.1
26	i=4, j=4 circumferential-axial mode (2 of 2)	321.13	0.83	328.48	2.3
27	i=2, j=3 circumferential-axial mode (1 of 2)			328.05	
28	i=2, j=3 circumferential-axial mode (2 of 2)			328.13	
29	i=4, j=5 circumferential-axial mode	353.67	0.71		
30	i=5, j=6 circumferential-axial mode	383.38	0.58		
31	i=4, j=6 circumferential-axial mode	391.35	0.92		

Table 20. Experimental and numerical modal frequencies of the ATC Configuration VI (6 psi)

Mode Number	Mode Shape	Measured Frequency	Measured Damping	Predicted Frequency	Error
[-]		[Hz]	[%]	[Hz]	[%]
1	i=2, j=1 circumferential-axial mode (1 of 2)	82.25	0.59	90.52	10.1
2	i=2, j=1 circumferential-axial mode (2 of 2)	82.93	0.65	90.93	9.6
3	First z translation	92.66	1.21		
4	First x bending	121.47	0.89	146.95	21.0
5	First y bending	122.97	0.96	147.76	20.2
6	First torsion	141.09	0.65	150.61	6.7
7	i=3, j=1 circumferential-axial mode (1 of 2)	150.57	0.28	151.24	0.4
8	i=3, j=1 circumferential-axial mode (2 of 2)	151.85	0.47	151.31	-0.4
9	i=2, j=2 circumferential-axial mode (1 of 2)			202.04	
10	i=2, j=2 circumferential-axial mode (2 of 2)	169.51	1.94	202.26	19.2
11	i=3, j=2 circumferential-axial mode (1 of 2)	176.12	0.37	183.81	4.4
12	i=3, j=2 circumferential-axial mode (2 of 2)	177.41	0.60	183.91	3.7
13	First xy bending	192.43	0.20		
14				198.83	
15	i=3, j=2 circumferential-axial mode (1 of 2)	217.88	0.30		
16	i=3, j=2 circumferential-axial mode (2 of 2)	218.13	0.22		
17	i=3, j=3 circumferential-axial mode (1 of 2)	225.68	1.22	246.65	9.3
18	i=3, j=3 circumferential-axial mode (2 of 2)	226.35	0.85	246.70	9.0
19				235.17	
20				239.20	
21				251.12	
22	i=2, j=3 circumferential-axial mode (1 of 2)	261.59	1.37	332.15	27.0
23	i=2, j=3 circumferential-axial mode (2 of 2)			332.18	
24	i=4, j=1 circumferential-axial mode (1 of 2)	268.77	0.69	266.47	-0.9
25	i=4, j=1 circumferential-axial mode (2 of 2)	272.09	0.65	266.48	-2.1
26					
27					
28	i=4, j=2 circumferential-axial mode (1 of 2)	276.59	0.81	275.74	-0.3
29	i=4, j=2 circumferential-axial mode (2 of 2)	279.74	0.60	275.75	-1.4
30				280.60	
31	i=3, j=4 circumferential-axial mode (1 of 2)	283.56	0.45	321.81	13.5
32	i=3, j=4 circumferential-axial mode (2 of 2)	285.48	0.39	321.88	12.8
33	i=4, j=3 circumferential-axial mode (1 of 2)	294.61	0.80	297.62	1.0
34	i=4, j=3 circumferential-axial mode (2 of 2)	297.24	0.65	297.77	0.2

Table 21. Experimental and numerical modal frequencies of ATC Configuration VI for 0 and 3 psi pressurization

Mode Number	Mode Shape	Measured Frequency 0 psi	Measured Frequency 3 psi	Measured Difference	Predicted Difference	Predicted Frequency 0 psi	Predicted Frequency 3 psi
[-]		[Hz]	[Hz]	[%]	[%]	[Hz]	[Hz]
1	i=2, j=1 circumferential-axial mode (1 of 2)	79.13	81.46	1.3	1.2	86.42	88.66
2	i=2, j=1 circumferential-axial mode (2 of 2)	79.91				86.85	89.08
3	First axial	92.92					
4	First x bending	123.17	122.60	-1.6	-0.8	146.78	146.93
5	First y bending	124.19				147.62	
6	First torsion	141.57				150.92	150.61
7	i=3, j=1 circumferential-axial mode (1 of 2)	143.87	147.41	2.5	2.8	144.18	147.93
8	i=3, j=1 circumferential-axial mode (2 of 2)	145.06	148.57	2.5	2.9	144.22	148.12
9		148.41					
10	First xy-bending	151.99					
11	i=2, j=2 circumferential-axial mode (1 of 2)	166.28				199.20	200.92
12	i=2, j=2 circumferential-axial mode (2 of 2)					199.42	201.16
13	i=3, j=2 circumferential-axial mode (1 of 2)	170.47	168.78	-2.7	2.5	177.46	180.93
14	i=3, j=2 circumferential-axial mode (2 of 2)	171.87	173.68	0.8	2.5	177.56	181.03
15	i=3, j=3 circumferential-axial mode (1 of 2)	220.34	223.42	2.1	2.6	240.45	244.06
16	i=3, j=3 circumferential-axial mode (2 of 2)	221.37				240.52	244.07
17	i=2, j=3 circumferential-axial mode (1 of 2)	259.34				324.98	
18	i=2, j=3 circumferential-axial mode (2 of 2)					325.08	
19	i=4, j=1 circumferential-axial mode (1 of 2)	261.54	265.38	2.8	3.0	258.87	262.90
20	i=4, j=1 circumferential-axial mode (2 of 2)	264.12	268.51	3.4	3.0	258.89	262.91
21	i=4, j=2 circumferential-axial mode (1 of 2)	269.09	273.18	3.1	3.1	268.17	272.23
22	i=4, j=2 circumferential-axial mode (2 of 2)	272.20	276.45	3.3	3.1	268.19	272.24
23	i=3, j=4 circumferential-axial mode (1 of 2)	280.25	284.09	2.8	4.1	313.50	318.62
24	i=3, j=4 circumferential-axial mode (2 of 2)					313.58	318.70
25	i=4, j=3 circumferential-axial mode (1 of 2)	286.77	293.62	5.9	3.5	289.63	294.14
26	i=4, j=3 circumferential-axial mode (2 of 2)	289.28			3.7	289.83	294.51
27	i=4, j=4 circumferential-axial mode (1 of 2)		318.43		4.3	323.16	328.44
28	i=4, j=4 circumferential-axial mode (2 of 2)		321.13		4.3	323.19	328.48
29	i=2, j=3 circumferential-axial mode (1 of 2)						328.05
30	i=2, j=3 circumferential-axial mode (2 of 2)						328.13
31	i=4, j=5 circumferential-axial mode		353.67				
32	i=5, j=6 circumferential-axial mode		383.38				
33	i=4, j=6 circumferential-axial mode		391.35				

Table 22. Experimental and numerical modal frequencies of ATC Configuration VI for 0 and 6 psi pressurization

Mode Number	Mode Shape	Measured Frequency 0 psi	Measured Frequency 6 psi	Measured Difference	Predicted Difference	Predicted Frequency 0 psi	Predicted Frequency 6 psi
[-]		[Hz]	[Hz]	[%]	[%]	[Hz]	[Hz]
1	i=2, j=1 circumferential-axial mode (1 of 2)	79.13	82.25	3.9	4.7	86.42	90.52
2	i=2, j=1 circumferential-axial mode (2 of 2)	79.91	82.93	3.8	4.7	86.85	90.93
3	First axial	92.92	92.66	-0.3			
4	First x bending	123.17	121.47	-1.4	0.1	146.78	146.95
5	First y bending	124.19	122.97	-1.0	0.1	147.62	147.76
6	First torsion	141.57	141.09	-0.3	-0.2	150.92	150.61
7	i=3, j=1 circumferential-axial mode (1 of 2)	143.87	150.57	4.7	4.9	144.18	151.24
8	i=3, j=1 circumferential-axial mode (2 of 2)	145.06	151.85	4.7	4.9	144.22	151.31
9		148.41					
10	First xy-bending	151.99					
11					0.7	154.23	155.24
12		158.15					
13	i=2, j=2 circumferential-axial mode (1 of 2)	166.28	169.51	1.9	1.4	199.20	202.04
14	i=2, j=2 circumferential-axial mode (2 of 2)				1.4	199.42	202.26
15	i=3, j=2 circumferential-axial mode (1 of 2)	170.47	176.12	3.3	3.6	177.46	183.81
16	i=3, j=2 circumferential-axial mode (2 of 2)	171.87	177.41	3.2	3.6	177.56	183.91
17					1.1	196.66	198.83
18	i=3, j=3 circumferential-axial mode (1 of 2)	220.34	225.68	2.4	2.6	240.45	246.65
19	i=3, j=3 circumferential-axial mode (2 of 2)	221.37	226.35	2.3	2.6	240.52	246.70
20					0.3	234.36	235.17
21					0.4	238.19	239.20
22					0.6	249.73	251.12
23	i=2, j=3 circumferential-axial mode (1 of 2)	259.34	261.59	0.9	2.2	324.98	332.15
24	i=2, j=3 circumferential-axial mode (2 of 2)				2.2	325.08	332.18
25	i=4, j=1 circumferential-axial mode (1 of 2)	261.54	268.77	2.8	2.9	258.87	266.47
26	i=4, j=1 circumferential-axial mode (2 of 2)	264.12	272.09	3.0	2.9	258.89	266.48
27						264.53	
28						264.55	
29	i=4, j=2 circumferential-axial mode (1 of 2)	269.09	276.59	2.8	2.8	268.17	275.74
30	i=4, j=2 circumferential-axial mode (2 of 2)	272.20	279.74	2.8	2.8	268.19	275.75
31	second axial						
32					0.3	279.77	280.60
33	i=3, j=4 circumferential-axial mode (1 of 2)	280.25	283.56	1.2	2.7	313.5	321.81
34	i=3, j=4 circumferential-axial mode (2 of 2)		285.48		2.6	313.58	321.88
35	i=4, j=3 circumferential-axial mode (1 of 2)	286.77	294.61	2.7	2.8	289.63	297.62
36	i=4, j=3 circumferential-axial mode (2 of 2)	289.28	297.29	2.8	2.7	289.83	297.77
37					0.2	292.21	292.88
38	i=4, j=4 circumferential-axial mode (1 of 2)				2.1	323.16	329.83
39	i=4, j=4 circumferential-axial mode (2 of 2)				2.1	323.19	329.92
40	panel mode on i=0, j=1 global mode				3.0	348.23	358.71
41	panel mode on i=0, j=2 global mode				3.0	351.75	367.13

Table 23. Predicted and measured modal frequencies of the ATC interior acoustic space

Mode Number	Axial	Circum-ferential	Radial	Frequency		Error	Mode Number	Axial	Circum-ferential	Radial	Frequency		Error
				Predicted	Measured						Predicted	Measured	
[-]	[-]	[-]	[-]	[Hz]	[Hz]	%	[-]	[-]	[-]	[-]	[Hz]	[Hz]	%
1	1	0	0	46.9	50.0	6.6	25	3	2	0	308.8	303.8	-1.6
2	2	0	0	94.0	95.0	1.1	26	3	2	0	309.9	303.8	-2.0
3	3	0	0	141.6	141.9	0.2	27	6	1	0	332.6	323.8	-2.7
4	0	1	0	165.2			28	6	1	0	332.6	323.8	-2.7
5	0	1	0	165.2			29	4	2	0	333.6		
6	1	1	0	171.8	170.0	-1.1	30	4	2	0	333.8		
7	1	1	0	171.8	170.0	-1.1	31	7	0	0	339.8	328.1	-3.6
8	4	0	0	189.7	188.8	-0.5	32	0	0	1	345.1	347.5	0.7
9	2	1	0	190.1	191.2	0.6	33	1	0	1	348.4	350.6	0.6
10	2	1	0	190.1	191.2	0.6	34	2	0	1	358.0	360.6	0.7
11	3	1	0	217.6	214.4	-1.5	35	5	2	0	363.8	354.4	-2.7
12	3	1	0	217.6	214.4	-1.5	36	5	2	0	364.2		
13	5	0	0	238.6	235.0	-1.5	37				377.8	365.0	-3.5
14	4	1	0	251.6	248.1	-1.2	38	7	1	0	377.8	365.0	-3.5
15	4	1	0	251.6	248.1	-1.2	39	0	3	0	379.2		
16	0	2	0	274.4	264.4	-3.8	40				386.0		
17	0	2	0	274.6	264.4	-3.8	41	1	3	0	390.0	379.4	-2.8
18	1	2	0	278.4	280.6	0.8	42	8	0	0	392.4		
19	1	2	0	278.6	280.6	0.8	43	8	1	0	425.8		
20	6	0	0	288.6	281.9	-2.4	44	9	0	0	446.8		
21	2	2	0	290.1	299.4	3.2	45	9	1	0	476.2		
22	2	2	0	290.1	299.4	3.2	46	10	0	0	503.1		
23	5	1	0	290.3	285.0	-1.9	47	10	1	0	529.2		
24	5	1	0	290.3	285.0	-1.9	48	11	0	0	561.5		

Table 24. Microphone location parameters for acoustic survey inside the ATC cylinder and the axial prediction locations of the cross-sectional Data Recovery Meshes (DRMs)

Microphone Locations on Each Radial	Angular Locations Radial 1	Angular Locations Radial 2	Angular Locations Radial 3	Angular Locations Radial 4	Axial Locations All Radials	Axial Prediction Locations of Cross-Sectional DRMs
[in]	[deg]	[deg]	[deg]	[deg]	[in]	
7	0	90	180	270	5	
12	15	105	195	285	17.75	
16.5	30	120	210	300	23.67	
21	45	135	225	315	35.5	
	60	150	240	330	40.57	
	75	165	255	345	47.33	47.33
					56.8	
					71	
					81.14	
					88.75	
					94.67	94.67
					106.5	106.5
					113.6	113.6
					118.33	118.33
					128	

Table 25. Participating modes in the structural modal analysis

Mode Number	Structural Mode	Predicted Frequency	Experimental Modal Damping	Mode Number	Structural Mode	Predicted Frequency	Experimental Modal Damping
[-]	[-]	[Hz]	[-]	[-]	[-]	[Hz}	[-]
1	(2,1)	86.55	0066	17	(3,3)	240.66	0.0074
2	(2,1)	86.98	0.0071	18		250.49	0.01
3	(3,1)	144.22	0.0028	19	(4,1)	258.89	0.0058
4	(3,1)	144.27	0.0060	20	(4,1)	258.90	0.0055
5	x-bending	146.76	0.0089	21	(4,2)	268.17	0.0056
6	y-bending	147.59	0.0079	22	(4,2)	268.19	0.0067
7	torsion	150.55	0.0101	23		279.77	0.01
8		155.06	0.01	24	(4,3)	289.63	0.0059
9	(3,2)	177.56	0.0035	25	(4,3)	289.83	0.0067
10	(3,2)	177.67	0.0089	26		292.21	0.01
11		198.44	0.01	27	(3,4)	313.50	0.0135
12	(2,2)	199.40	0.0115	28	(3,4)	313.58	0.01
13	(2,2)	199.70	0.01	29	(4,4)	323.16	0.01
14		234.54	0.01	30	(4,4)	323.19	0.01
15		238.52	0.01	31	(2,3)	324.98	0.0126
16	(3,3)	240.56	0.0101	32	(2,3)	325.08	0.01

14 FIGURES

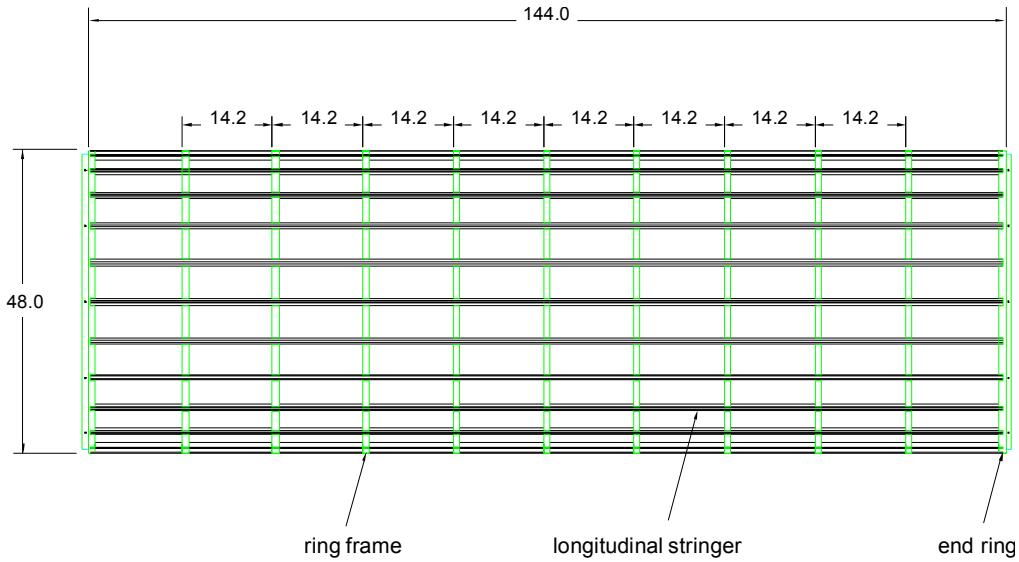

Figure 1. Aluminum Testbed Cylinder (ATC) base configuration (Configuration 1) showing the frames, the stringers and the end rings (all dimensions in inches)

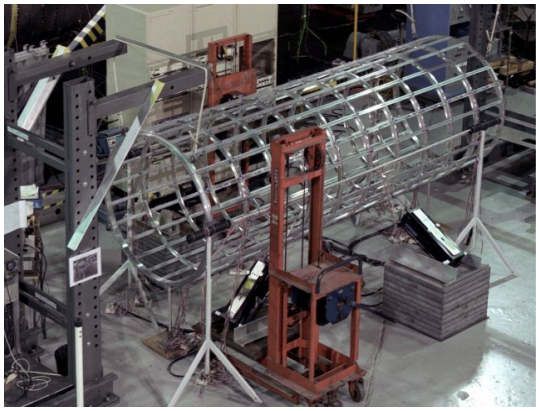

Figure 2. ATC Configuration I

Figure 3. ATC Configuration II

Figure 4. ATC Configuration III

Figure 5. ATC Configuration V

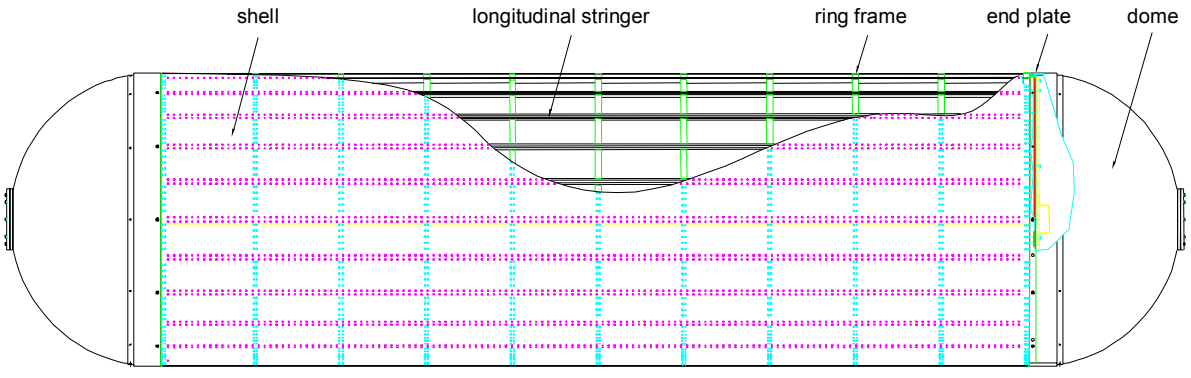

Figure 6. ATC Configuration V showing the shell, stringers, frames, end plates and fiberglass-composite domes

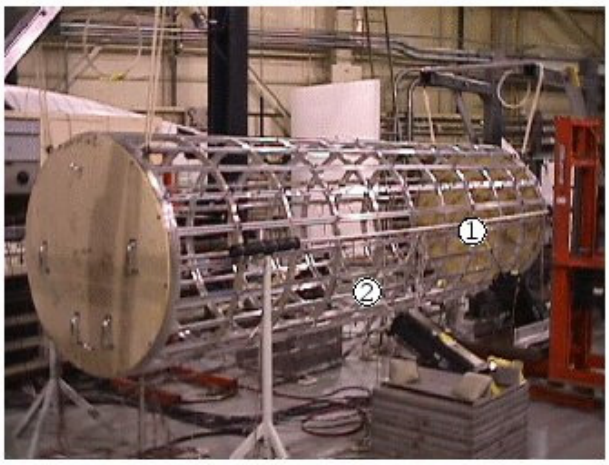

Starboard side: torsional and axial (1) / radial (2)

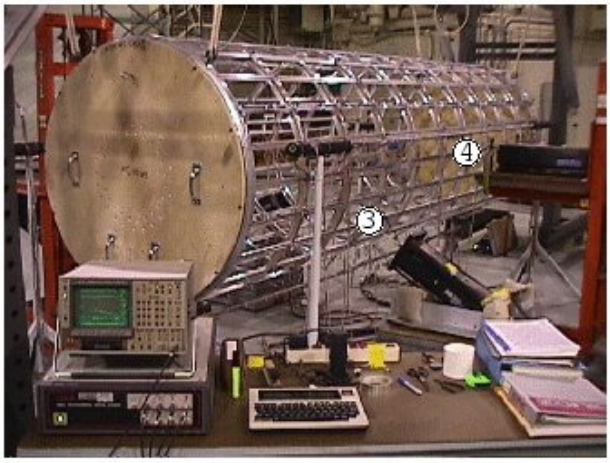

Port side: radial (3) / radial (4 - horizontal)

Figure 7. Shaker excitation locations in Configuration II

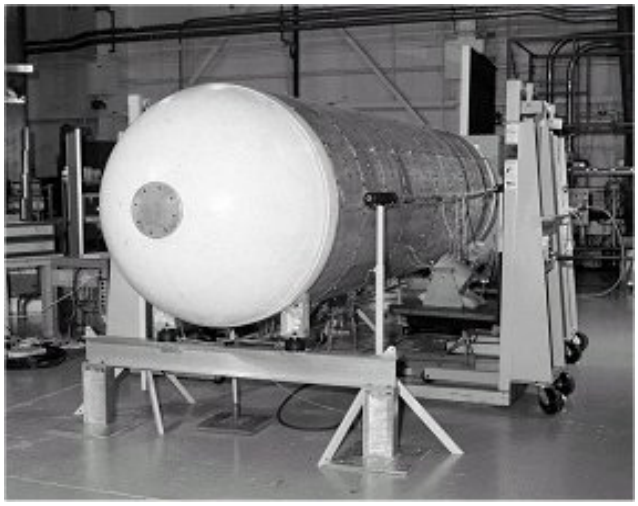

Figure 8. Test setup of ATC Configuration V

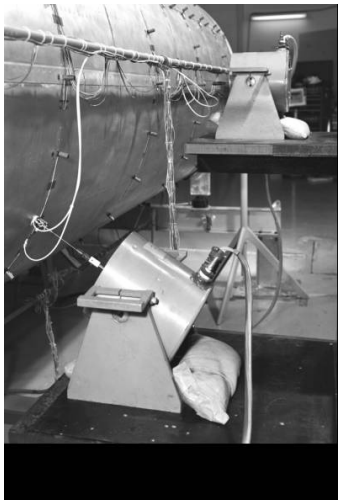

Figure 9. Shaker used for modal testing

Figure 10. Impedance head

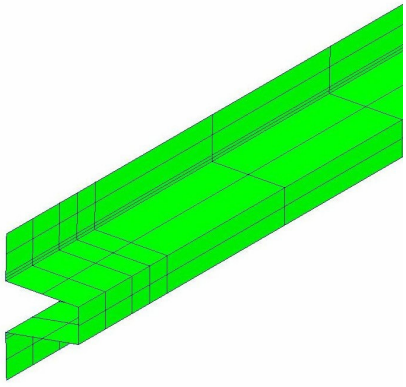

Figure 11. Hat stringer finite element plate model

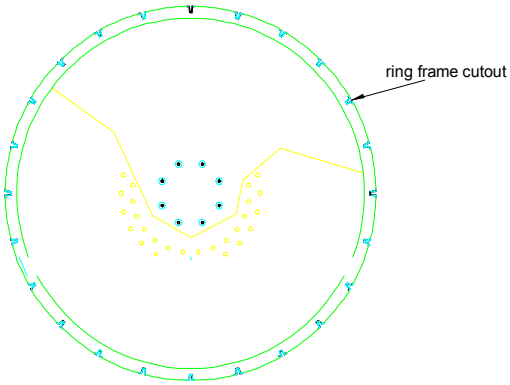

Figure 12. ATC ring frame showing the twenty-four cutouts to accommodate the longitudinal stringers

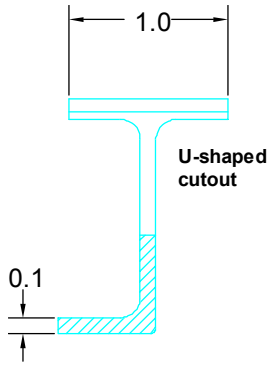

Figure 13. Ring frame "J" cross-section

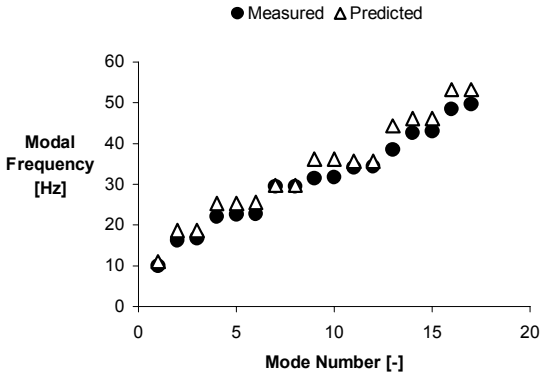

Figure 14. Comparison of seventeen predicted and measured modal frequencies for Configuration I

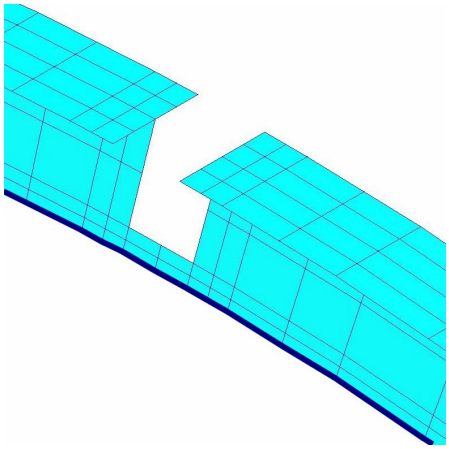

Figure 15. Enhanced hybrid plate-beam ring frame model with double the plate elements and beam elements for the ring frame flanges

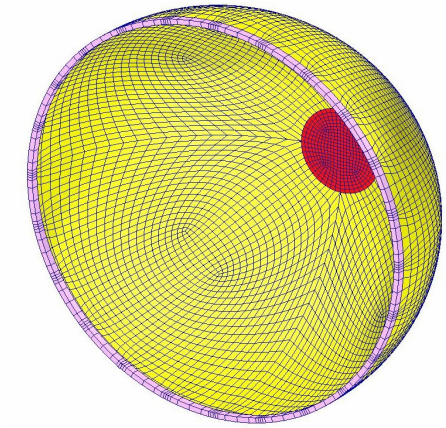

Figure 16. Finite element model showing substructures for the dome, the dome rings and the access plates

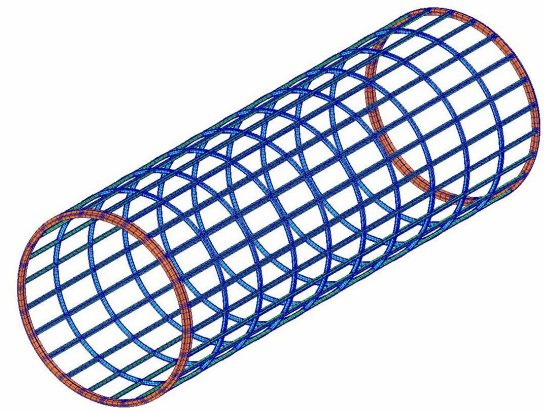

Figure 17. Configuration I finite element model

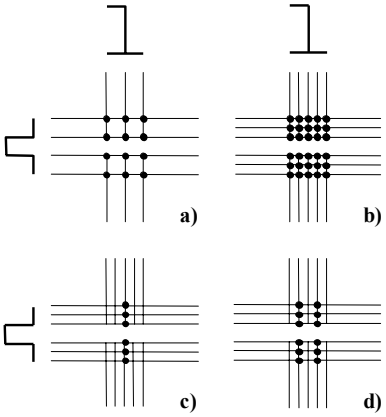

Figure 18. Top view of the hat-section stringer and the J-section ring frame connections showing mutual nodes

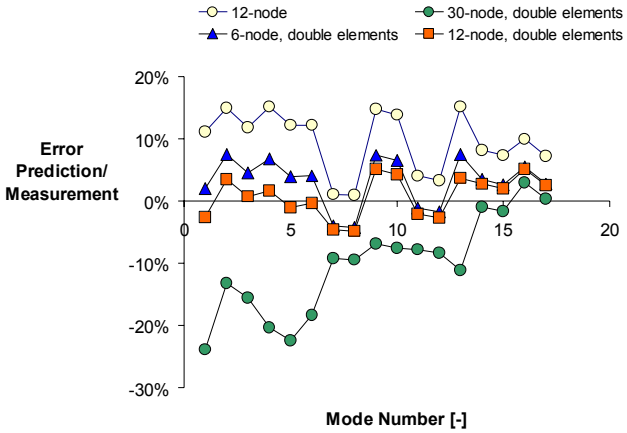

Figure 19. Configuration I modal frequencies prediction/measurement errors

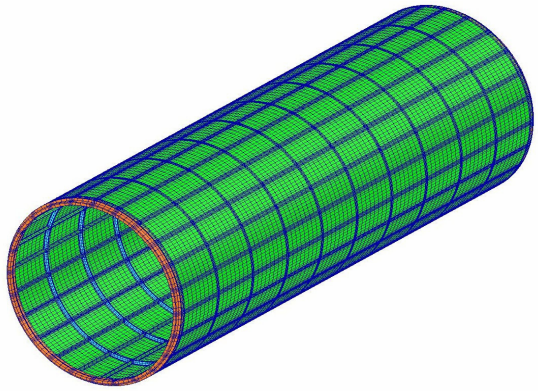

Figure 20. Configuration III finite element model

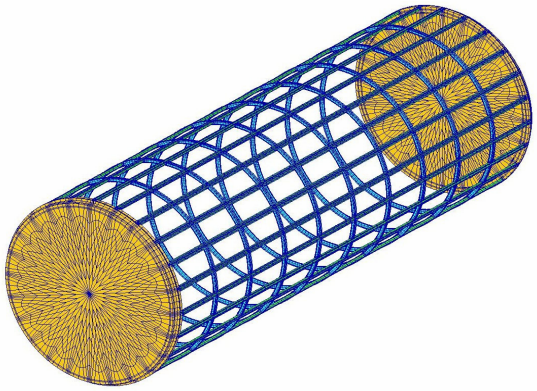

Figure 21. Configuration II finite element model

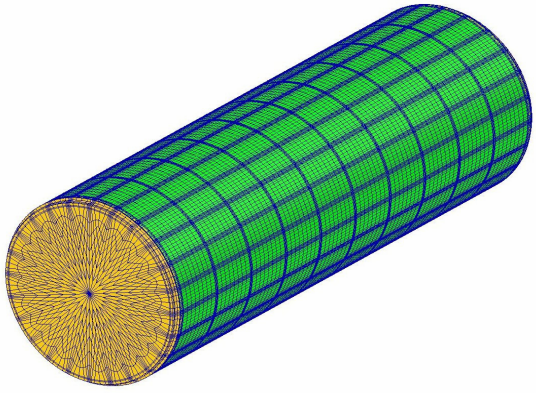

Figure 22. Configuration IV finite element model

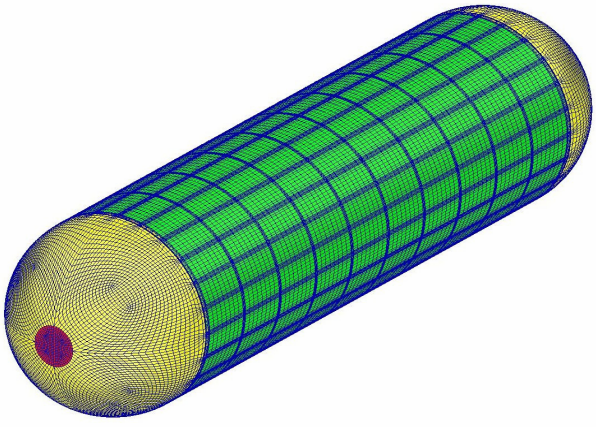

Figure 23. Configuration V finite element model

1. Mode number 1, Frequency 80.4 Hz, Shape: i=2, j=1 circumferential-axial mode (1 of 2)

2. Mode number 4, Frequency 143.2 Hz, Shape: i=3, j=1 circumferential-axial mode (1 of 2)

3. Endcap mode 1, Frequency 156.9 Hz

4. Mode number 8, Frequency 175.4 Hz, Shape: i=3, j=2 circumferential-axial mode (1 of 2)

5. Mode number 6, Frequency 176.2 Hz, Shape: First bending (1 of 2)

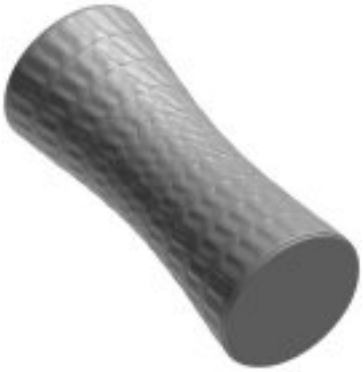

6. Mode number 10, Frequency 180.5 Hz, Shape: First torsion

7. Mode number 11, Frequency 195.4 Hz, Shape: i=2, j=2 circumferential-axial mode (1 of 2)

8. Endcap mode 2, Frequency 217.5 Hz

9. Mode number 14, Frequency 238.7 Hz, Shape: i=3, j=3 circumferential-axial mode (1 of 2)

Figure 24. ATC Configuration IV structural mode numbers, modal frequencies and mode shapes (Table 16)

10. Mode number 16, Frequency 258.7 Hz, Shape: i=4, j=1 circumferential-axial mode (1 of 2)

11. Mode number 18, Frequency 267.6 Hz, Shape: i=4, j=2 circumferential-axial mode (1 of 2)

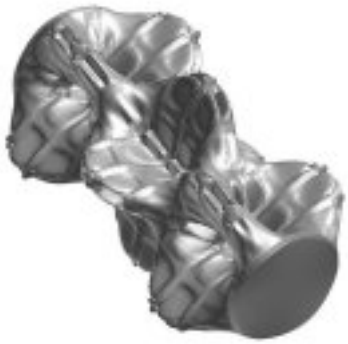

12. Mode number 22, Frequency 289.0 Hz, Shape: i=4, j=3 circumferential-axial mode (1 of 2)

13. Mode number 20, Frequency 312.3 Hz, Shape: i=3, j=4 circumferential-axial mode (1 of 2)

14. Mode number 24, Frequency 321.6 Hz, Shape: Second bending (1 of 2)

15. Mode number 28, Frequency 322.3 Hz, Shape: i=4, j=4 circumferential-axial mode (1 of 2)

16. Mode number 26, Frequency 323.2 Hz, Shape: i=2, j=3 circumferential-axial mode (1 of 2)

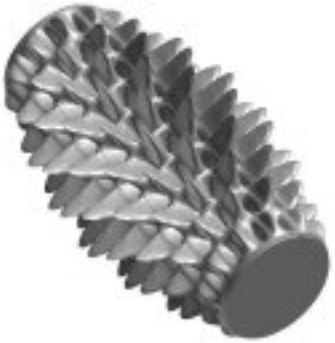

17. Mode number 30, Frequency 348.2 Hz, Shape: First panel mode on i=1, j=1 global

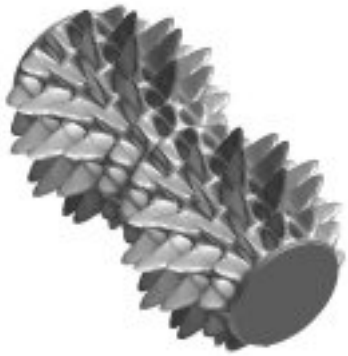

18. Mode number 31, Frequency 351.7 Hz, Shape: First panel mode on i=1, j=2 global

Figure 24 (continued). ATC Configuration IV structural mode numbers, modal frequencies and mode shapes (Table 16)

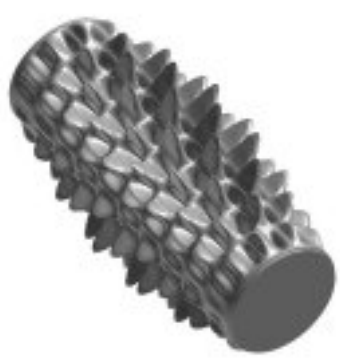

19. Mode number 32, Frequency 352.0 Hz, Shape: First panel mode on i=2, j=1 (1 of 2)

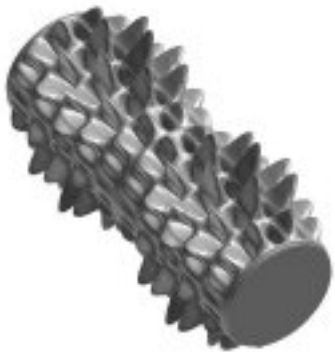

20. Mode number 34, Frequency 355.4 Hz, Shape: First panel mode on i=2, j=2 (1 of 2)

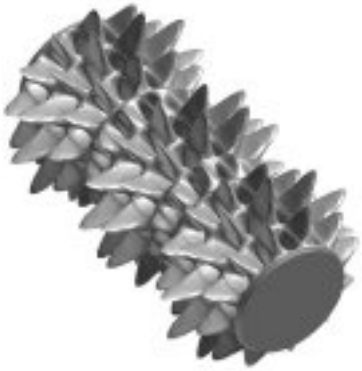

21. Mode number 36, Frequency 357.0 Hz, Shape: First panel mode on i=1, j=3 global

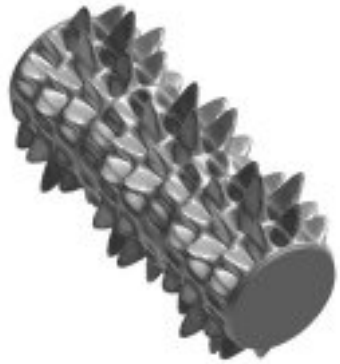

22. Mode number 37, Frequency 360.6 Hz, Shape: First panel mode on i=2, j=3 (1 of 2)

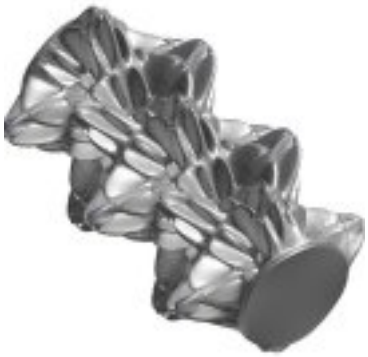

23. Mode number 39, Frequency 361.7 Hz, Shape: i=4, j=4 circumferential-axial mode (1 of 2)

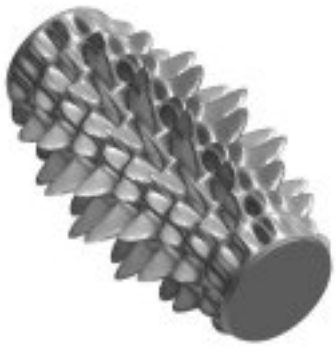

24. Mode number 41, Frequency 362.7 Hz, Shape: First panel mode on i=4, j=1 (1 of 2)

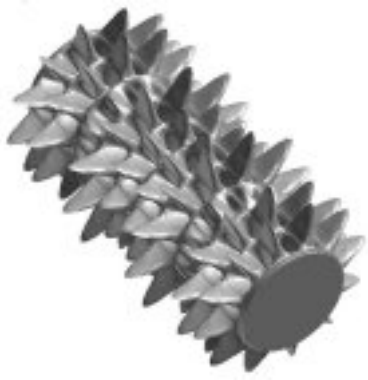

25. Mode number 43, Frequency 363.8 Hz, Shape: First panel mode on i=1, j=4 global

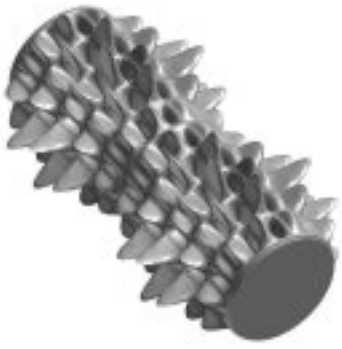

26. Mode number 44, Frequency 366.1 Hz, Shape: First panel mode on i=4, j=2 (1 of 2)

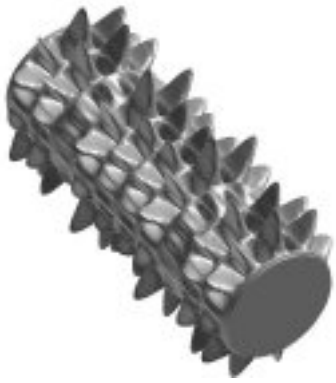

27. Mode number 46, Frequency 367.1 Hz, Shape: First panel mode on i=2, j=4 (1 of 2)

Figure 24 (continued). ATC Configuration IV structural mode numbers, modal frequencies and mode shapes (Table 16)

28. Mode number 48, Frequency 367.8 Hz

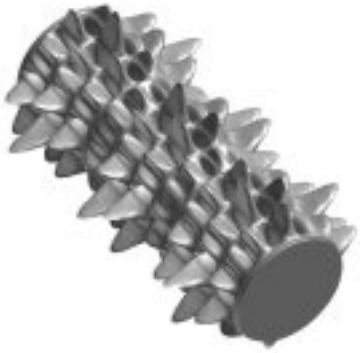

29. Mode number 50, Frequency 370.9 Hz, Shape: First panel mode on i=4, j=3 (1 of 2)

30. Mode number 52, Frequency 371.2 Hz, Shape: First panel mode on i=1, j=5 global

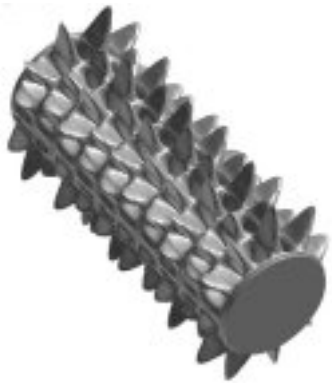

31. Mode number 53, Frequency 374.3 Hz Shape: First panel mode on i=2, j=5 (1 of 2)

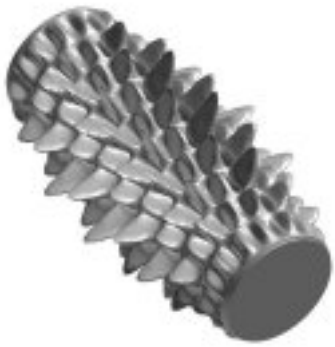

32. Mode number 55, Frequency 376.7 Hz, Shape: First panel mode on i=6, j=1 (1 of 2)

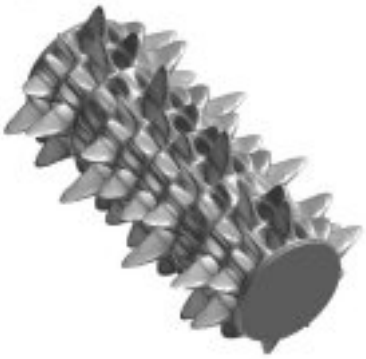

33. Mode number 57, Frequency 376.9 Hz, Shape: First panel mode on i=4, j=4 (1 of 2)

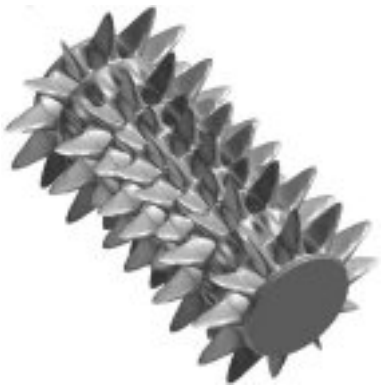

34. Mode number 59, Frequency 378.7 Hz, Shape: First panel mode on i=1, j=6 global

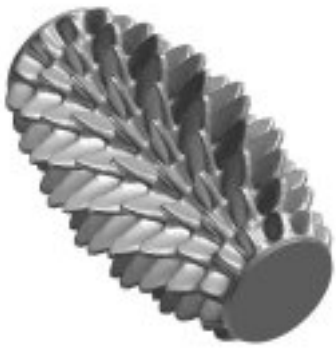

35. Mode number 60, Frequency 379.1 Hz, Shape: First stringer mode on i=1, j=1 global

36. Mode number 61, Frequency 379.6 Hz, Shape: i=3, j=5 circumferential-axial mode (1 of 2)

Figure 24 (continued). ATC Configuration IV structural mode numbers, modal frequencies and mode shapes (Table 16)

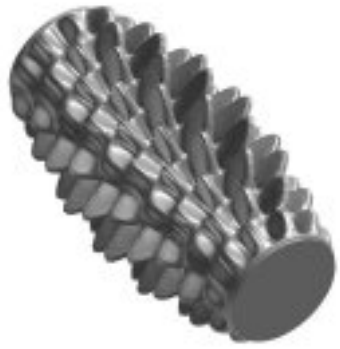

37. Mode number 63, Frequency 381.3 Hz, Shape: First stringer mode on i=2, j=1 (1 of 2)

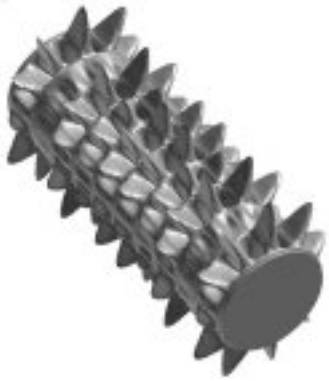

38. Mode number 65, Frequency 381.5 Hz, Shape: First panel mode on i=2, j=6 (1 of 2)

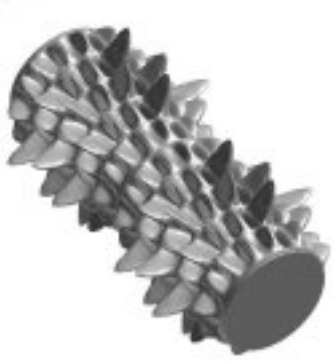

39. Mode number 67, Frequency 381.7 Hz, Shape: First panel mode on i=6, j=2 (1 of 2)

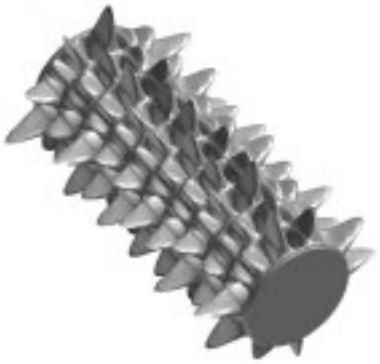

40. Mode number 69, Frequency 383.4 Hz, Shape: First panel mode on i=2, j=7 (1 of 2)

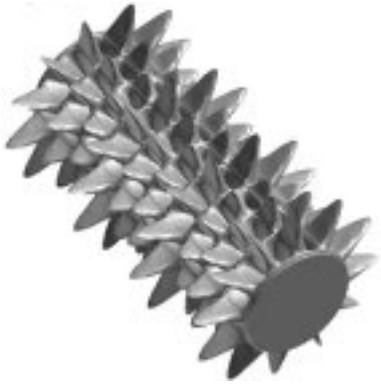

41. Mode number 71, Frequency 385.6 Hz, Shape: First panel mode on i=1, j=7 global

42. Mode number 72, Frequency 386.5 Hz, Shape: i=5, j=1 circumferential-axial mode (1 of 2)

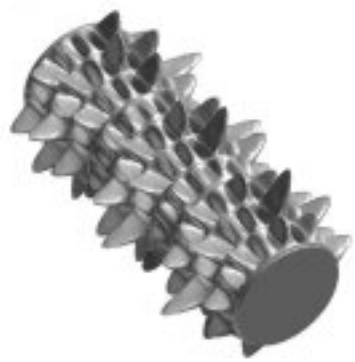

43. Mode number 74, Frequency 387.2Hz

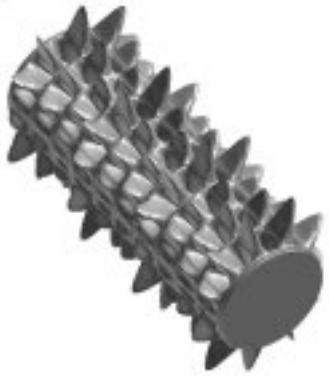

44. Mode number 76, Frequency 388.3 Hz

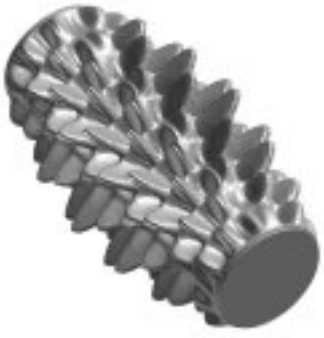

45. Mode number 78, Frequency 388.9 Hz

Figure 24 (continued). ATC Configuration IV structural mode numbers, modal frequencies and mode shapes (Table 16)

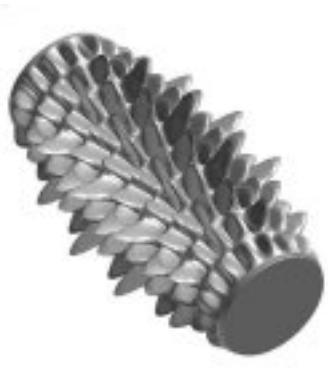

46. Mode number 80, Frequency 389.8 Hz

47. Mode number 82, Frequency 390.0 Hz
Shape: i=5, j=2 circumferential-axial mode (1 of 2)

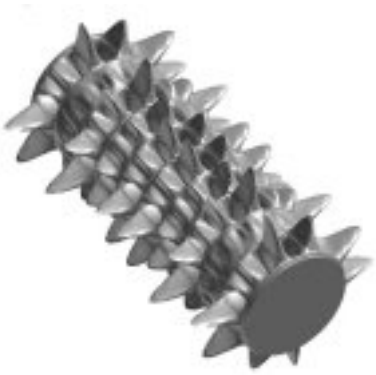

48. Mode number 84, Frequency 390.1 Hz

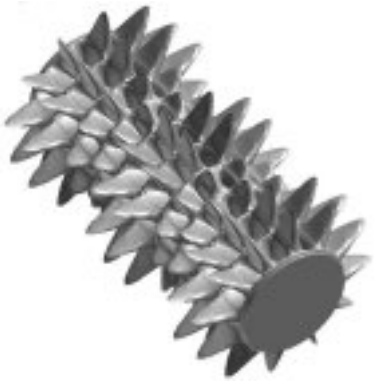

49. Mode number 86, Frequency 391.4 Hz

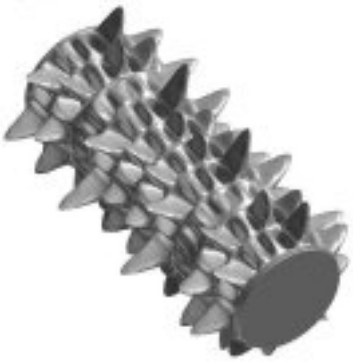

50. Mode number 87, Frequency 392.7 Hz

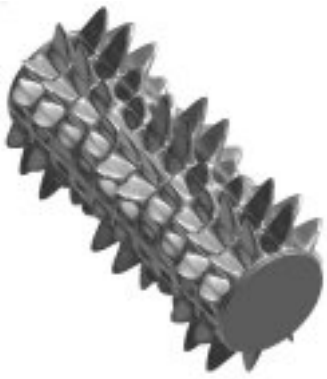

51. Mode number 89, Frequency 393.9 Hz

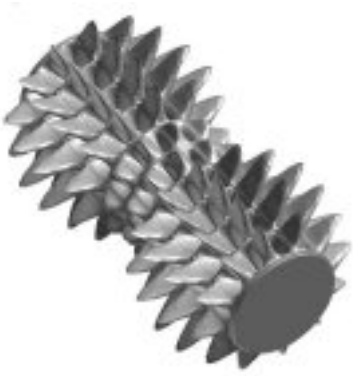

52. Mode number 91, Frequency 395.8 Hz

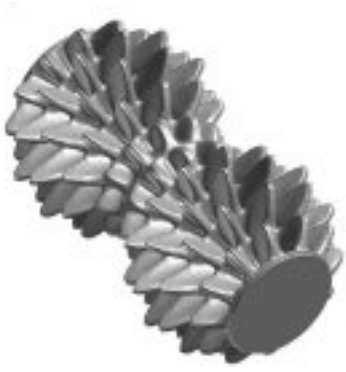

53. Mode number 92, Frequency 396.1 Hz

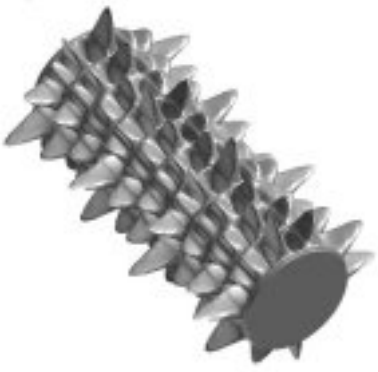

54. Mode number 93, Frequency 396.3 Hz

Figure 24 (continued). ATC Configuration IV structural mode numbers, modal frequencies and mode shapes (Table 16)

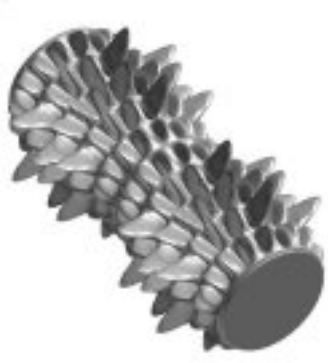

55. Mode number 95, Frequency 397.5 Hz

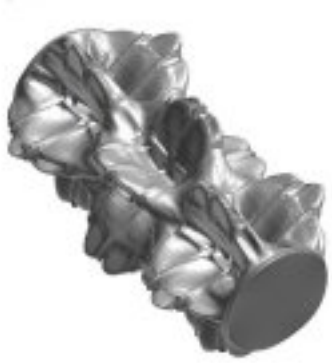

56. Mode number 97, Frequency 398.0 Hz
Shape: i=5, j=3 circumferential-axial mode (1 of 2)

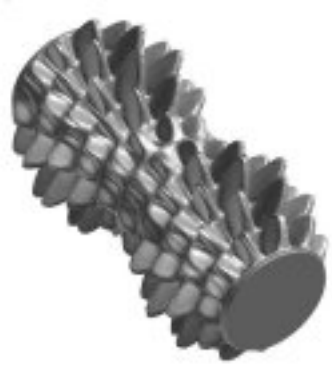

57. Mode number 99, Frequency 398.1 Hz

58. Mode number 101, Frequency 398.2 Hz

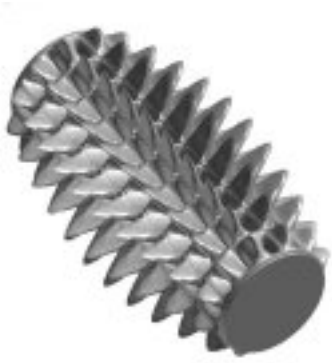

59. Mode number 103, Frequency 398.4 Hz

60. Mode number 104, Frequency 398.4 Hz

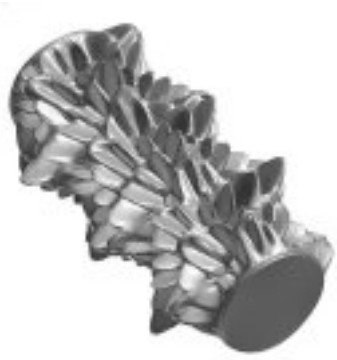

61. Mode number 106, Frequency 399.5 Hz

62. Mode number 108, Frequency 400.9 Hz

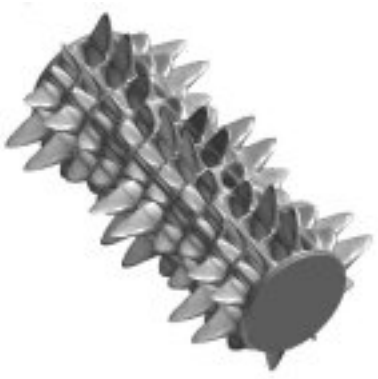

63. Mode number 110, Frequency 401.5 Hz

Figure 24 (continued). ATC Configuration IV structural mode numbers, modal frequencies and mode shapes (Table 16)

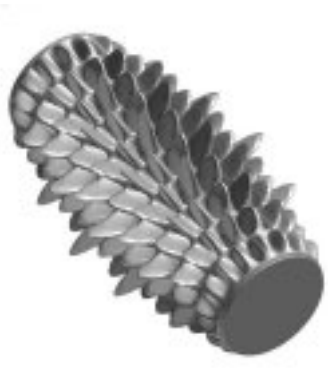

64. Mode number 112, Frequency 402.6 Hz

65. Mode number 114, Frequency 404.1 Hz

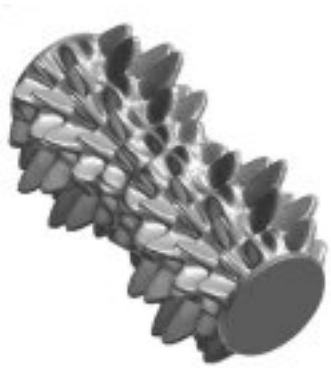

66. Mode number 116, Frequency 405.0 Hz

67. Mode number 118, Frequency 405.6 Hz

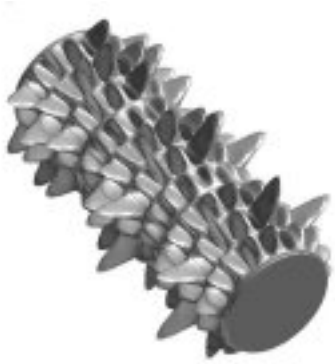

68. Mode number 120, Frequency 405.9 Hz

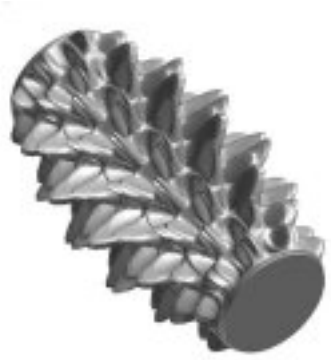

69. Mode number 122, Frequency 406.6 Hz

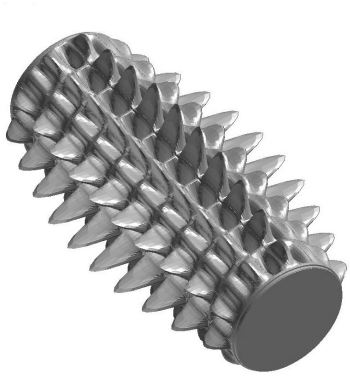

70. Mode number 124, Frequency 408.1 Hz

71. Mode number 126, Frequency 408.5 Hz

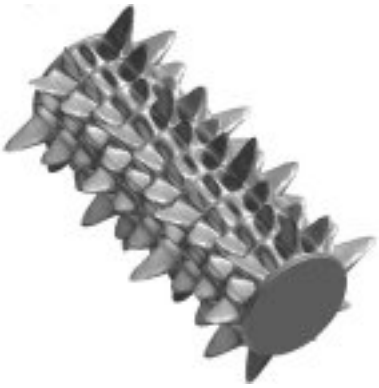

72. Mode number 128, Frequency 409.5 Hz

Figure 24 (continued). ATC Configuration IV structural mode numbers, modal frequencies and mode shapes (Table 16)

1. Mode number 1, Frequency 86.6 Hz
Shape: i=2, j=1 circumferential-axial mode
(1 of 2)

2. Mode number 7, Frequency 144.2 Hz
Shape: i=3, j=1 circumferential-axial mode
(1 of 2)

3. Mode number 4, Frequency 146.8 Hz
Shape: First x-bending

4. Mode number 6, Frequency 150.6 Hz
Shape: First torsion

5. Mode number 15, Frequency 177.6 Hz
Shape: i=3, j=2 circumferential-axial mode
(1 of 2)

6. Mode number 13, Frequency 199.4 Hz
Shape: i=2, j=2 circumferential-axial mode
(1 of 2)

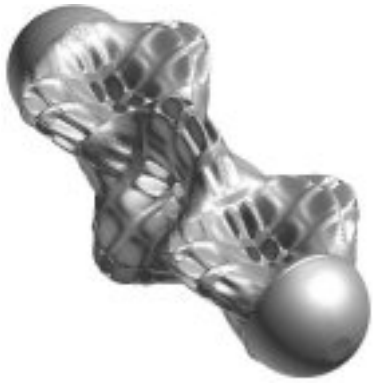

7. Mode number 18, Frequency 240.6 Hz
Shape: i=3, j=3 circumferential-axial mode
(1 of 2)

8. Mode number 25, Frequency 258.9 Hz
Shape: i=4, j=1 circumferential-axial mode
(1 of 2)

9. Mode number 29, Frequency 268.2 Hz
Shape: i=4, j=2 circumferential-axial mode
(1 of 2)

Figure 25. ATC Configuration V with gap, mode numbers, modal frequencies and mode shapes (Table 18)

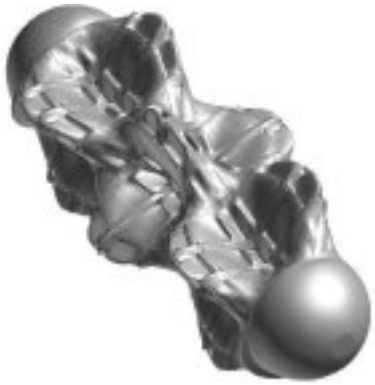

10. Mode number 35, Frequency 289.6 Hz, Shape: i=4, j=3 circumferential-axial mode (1 of 2)

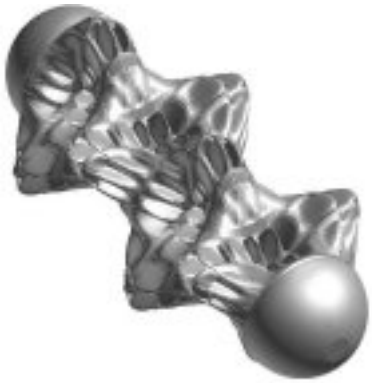

11. Mode number 33, Frequency 313.5 Hz Shape: i=3, j=4 circumferential-axial mode (1 of 2)

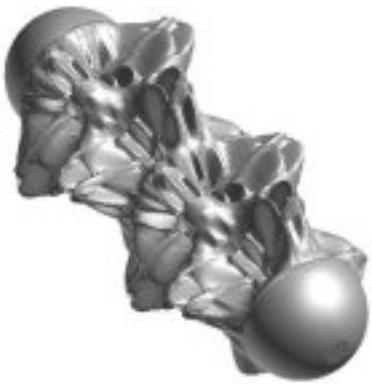

12. Mode number 38, Frequency 323.2 Hz Shape: i=4, j=4 circumferential-axial mode (1 of 2)

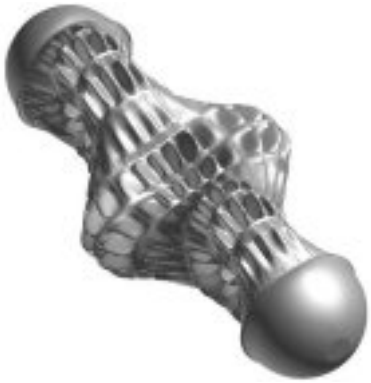

13. Mode number 23, Frequency 325.0 Hz Shape: i=2, j=3 circumferential-axial mode (1 of 2)

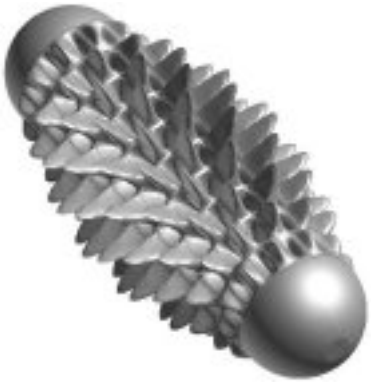

14. Mode number 40, Frequency 348.2 Hz Shape: First panel mode on i=0, j=1 (1 of 2)

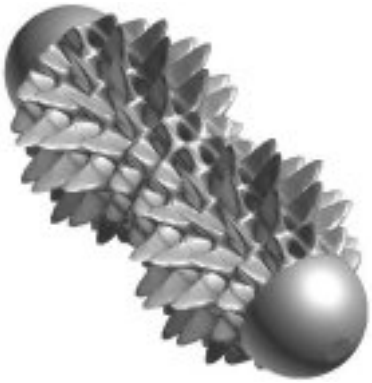

15. Mode number 41, Frequency 351.8 Hz Shape: First panel mode on i=0, j=2 (1 of 2)

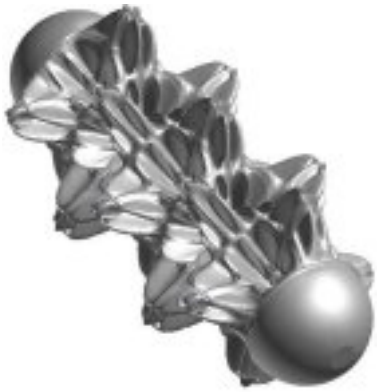

16. Mode number 50, Frequency 362.4 Hz Shape: i=4, j=5 circumferential-axial mode (1 of 2)

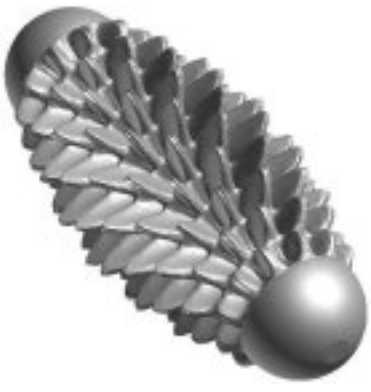

17. Mode number 72, Frequency 379.1 Hz Shape: First stringer mode on i=0, j=1 (1 of 2)

18. Mode number 73, Frequency 380.3 Hz Shape: i=3, j=5 circumferential-axial mode (1 of 2)

Figure 25 (continued). ATC Configuration V with gap, mode numbers, modal frequencies and mode shapes (Table 18)

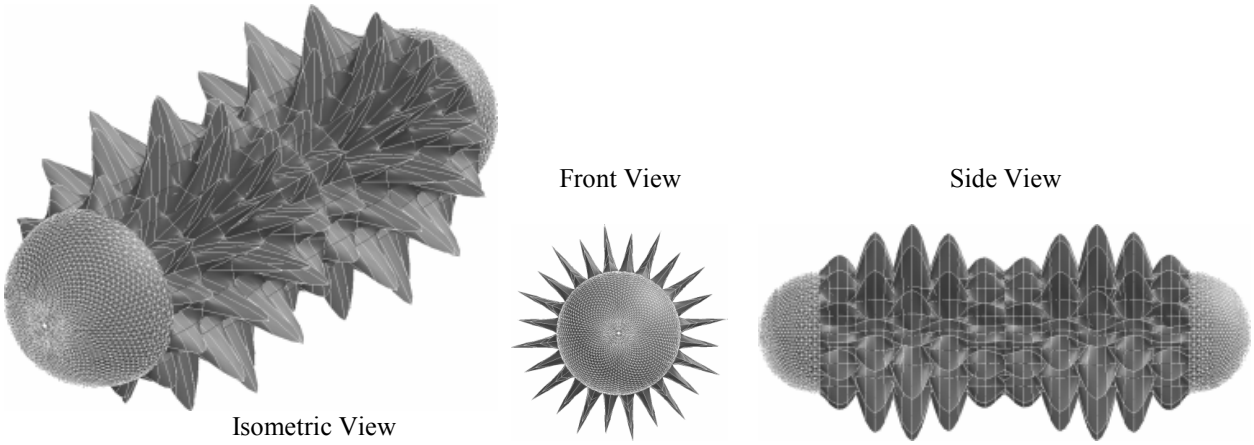

Figure 26. Subpanel mode superimposed on a 0,2 global cylinder mode shape (351.75.47 Hz, Table 18)

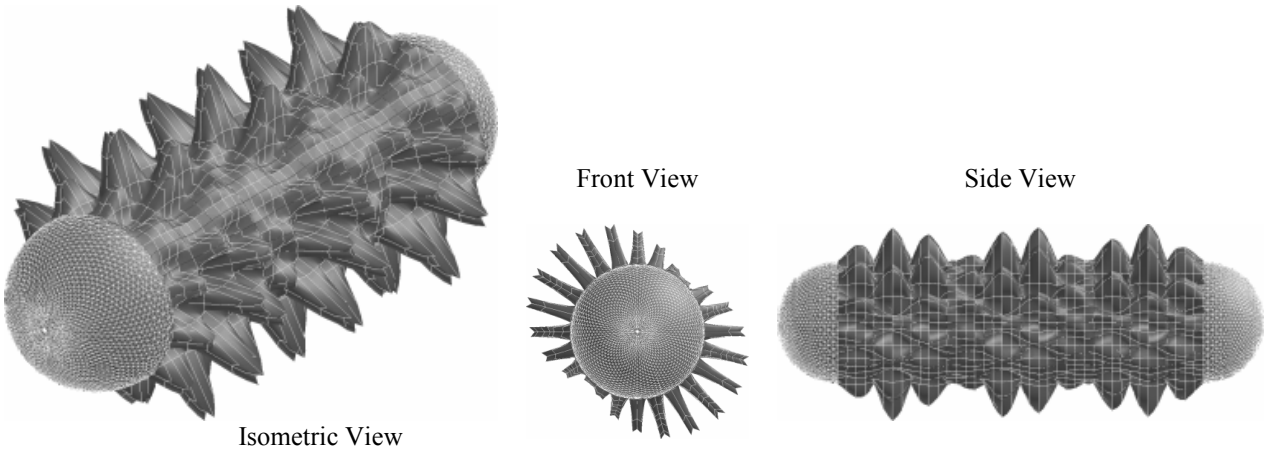

Figure 27. Stringer mode superimposed on a 1,3 global cylinder mode shape

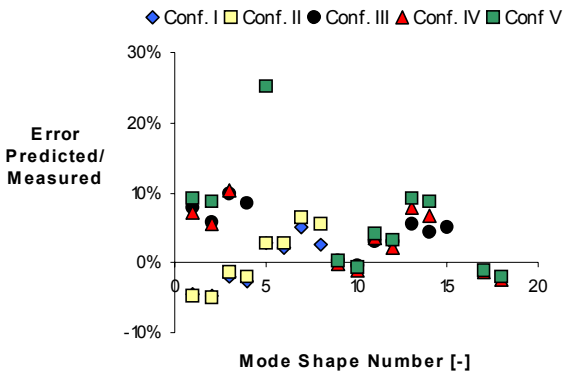

Figure 28. Circumferential-axial modal frequencies prediction/measurement errors

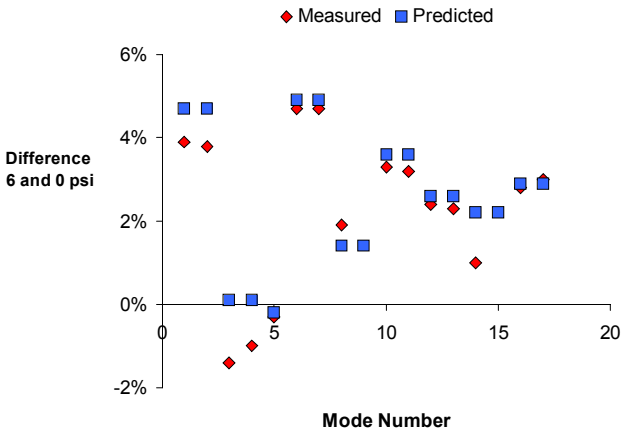

Figure 29. Differences between 6 psi and 0 psi modal frequencies for Configuration VI

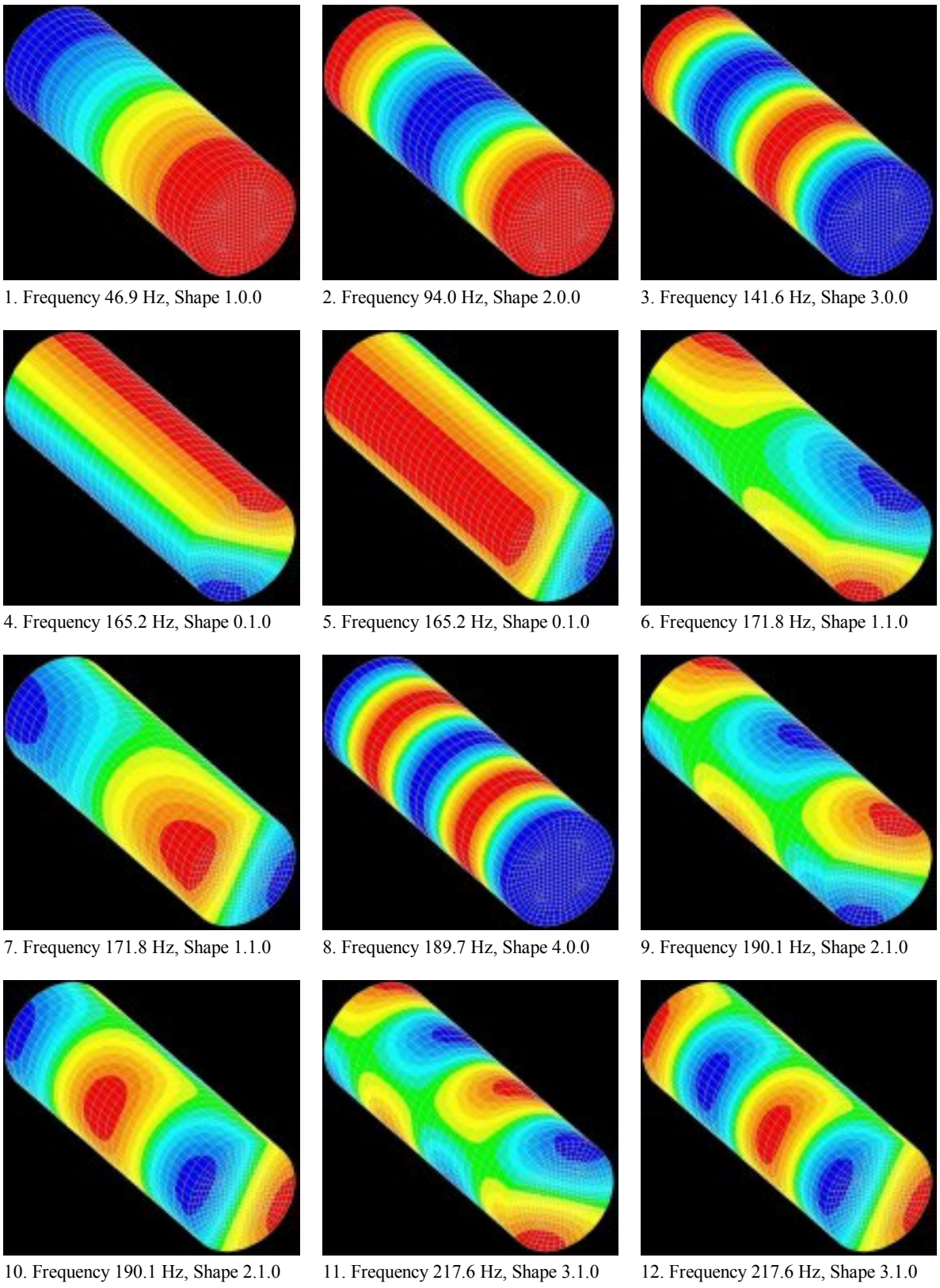

1. Frequency 46.9 Hz, Shape 1.0.0
2. Frequency 94.0 Hz, Shape 2.0.0
3. Frequency 141.6 Hz, Shape 3.0.0
4. Frequency 165.2 Hz, Shape 0.1.0
5. Frequency 165.2 Hz, Shape 0.1.0
6. Frequency 171.8 Hz, Shape 1.1.0
7. Frequency 171.8 Hz, Shape 1.1.0
8. Frequency 189.7 Hz, Shape 4.0.0
9. Frequency 190.1 Hz, Shape 2.1.0
10. Frequency 190.1 Hz, Shape 2.1.0
11. Frequency 217.6 Hz, Shape 3.1.0
12. Frequency 217.6 Hz, Shape 3.1.0

Figure 30. ATC acoustic mode numbers, modal frequencies and mode shapes

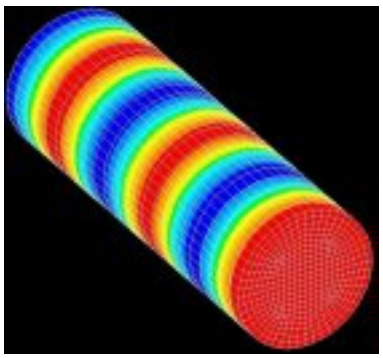

13. Frequency 238.6 Hz, Shape 5.0.0

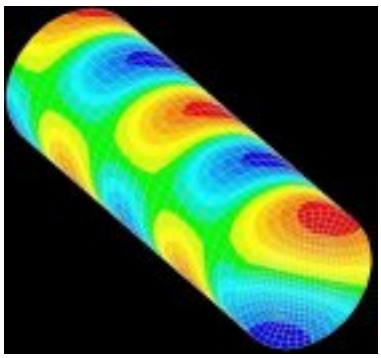

14. Frequency 251.6 Hz, Shape 4.1.0

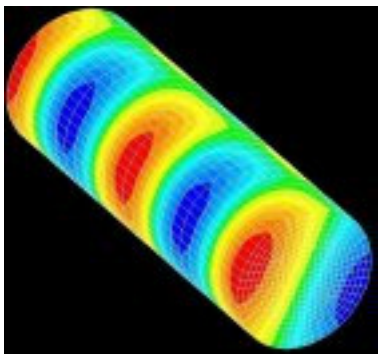

15. Frequency 251.6 Hz, Shape 4.1.0

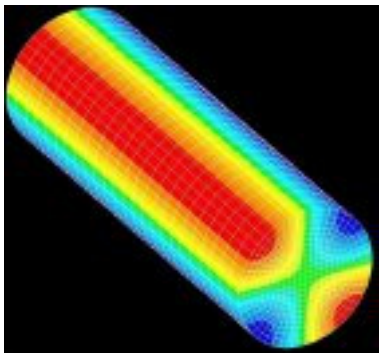

16. Frequency 274.4 Hz, Shape 0.2.0

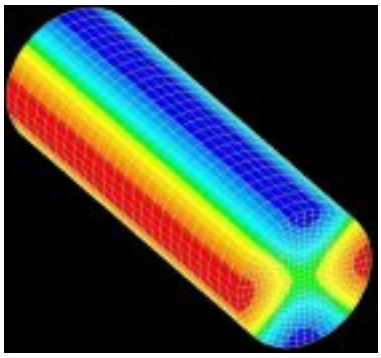

17. Frequency 274.6 Hz, Shape 0.2.0

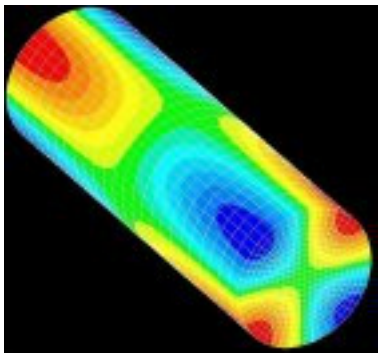

18. Frequency 278.4 Hz, Shape 1.2.0

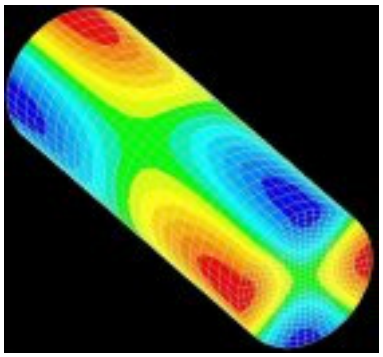

19. Frequency 278.6 Hz, Shape 1.2.0

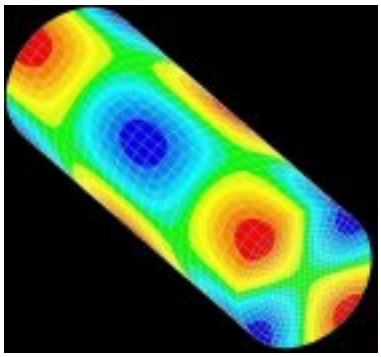

20. Frequency 290.1 Hz, Shape 2.2.0

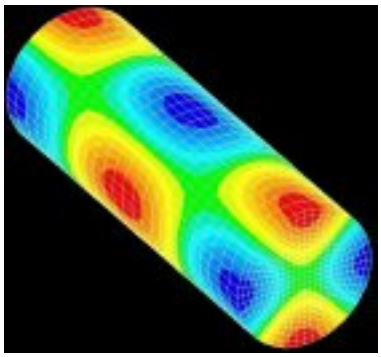

21. Frequency 290.3 Hz, Shape 2.2.0

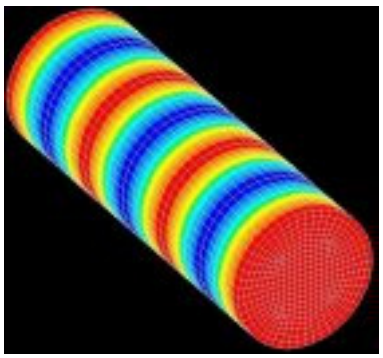

22. Frequency 288.6 Hz, Shape 6.0.0

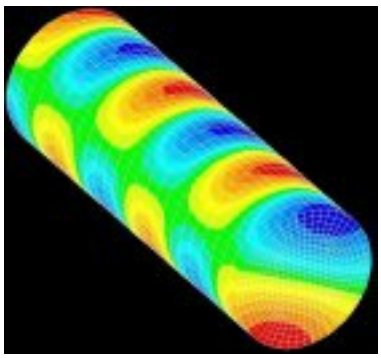

23. Frequency 290.3 Hz, Shape 5.1.0

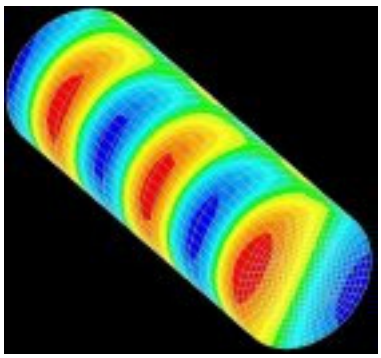

24. Frequency 290.3 Hz, Shape 5.1.0

Figure 30 (continued). ATC acoustic mode numbers, modal frequencies and mode shapes

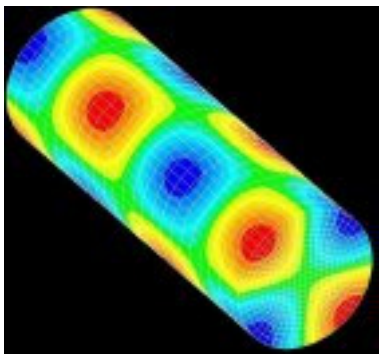

25. Frequency 308.8 Hz, Shape 3.2.0

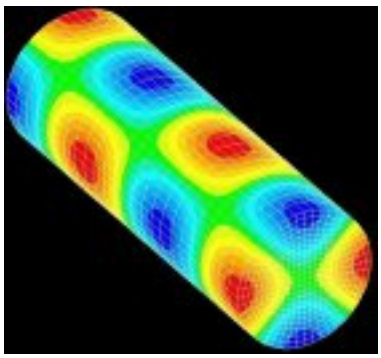

26. Frequency 309.0 Hz, Shape 3.2.0

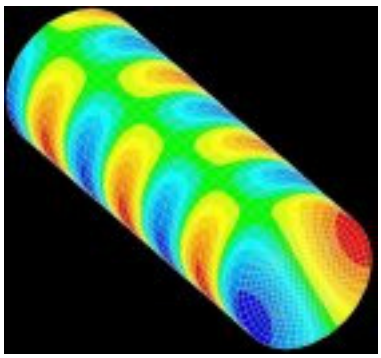

27. Frequency 332.6 Hz, Shape 6.1.0

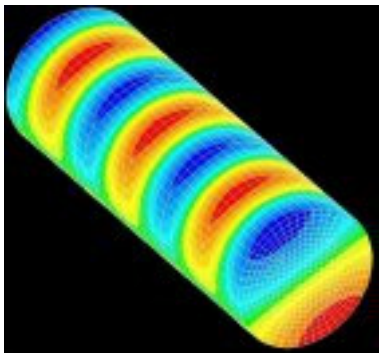

28. Frequency 332.6 Hz, Shape 6.1.0

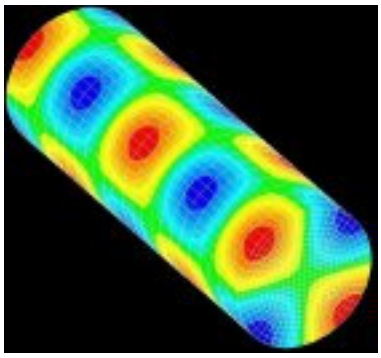

29. Frequency 333.6 Hz, Shape 4.2.0

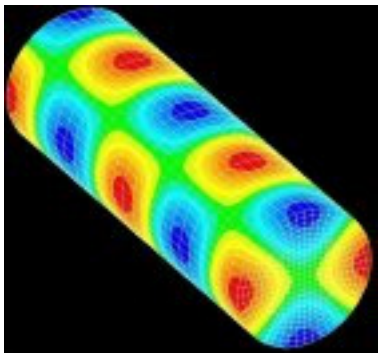

30. Frequency 333.8 Hz, Shape 4.2.0

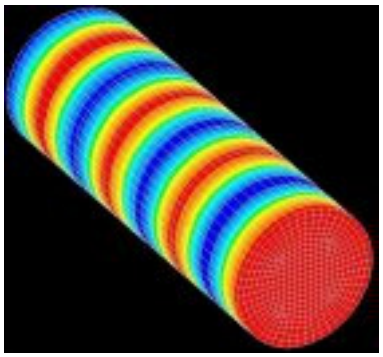

31. Frequency 339.8 Hz, Shape 7.0.0

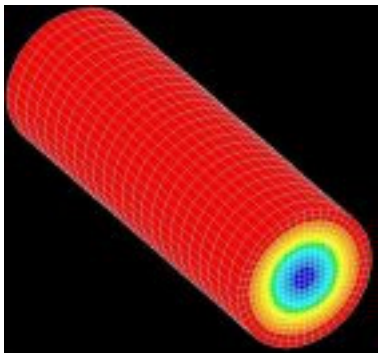

32. Frequency 345.1 Hz, Shape 0.0.1

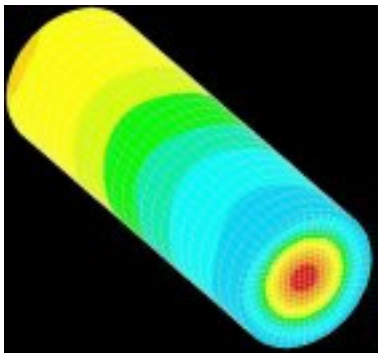

33. Frequency 348.4 Hz, Shape 1.0.1

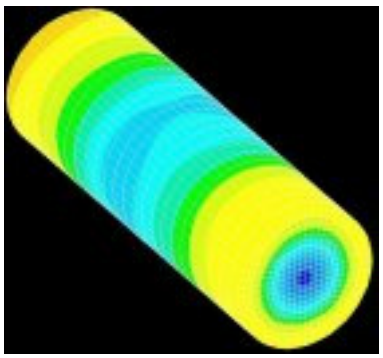

34. Frequency 358.0 Hz, Shape 2.0.1

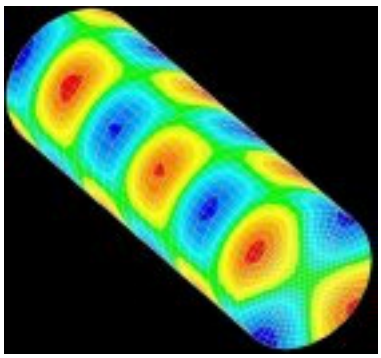

35. Frequency 363.8 Hz, Shape 5.2.0

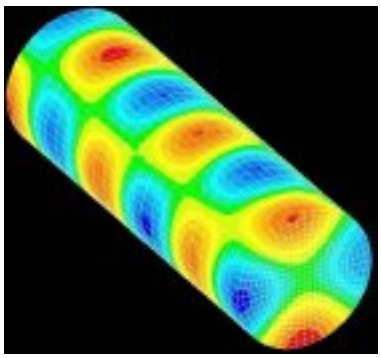

36. Frequency 364.2 Hz, Shape 5.2.0

Figure 30 (continued). ATC acoustic mode numbers, modal frequencies and mode shapes

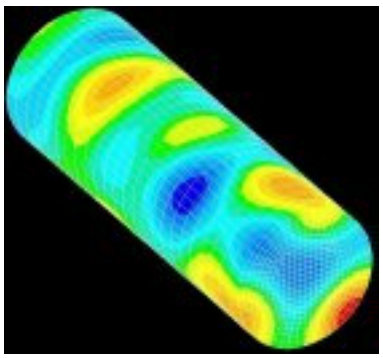

37. Frequency 377.8 Hz

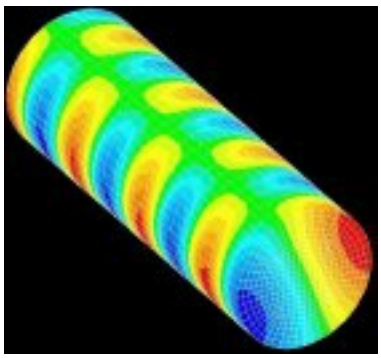

38. Frequency 377.8 Hz, Shape 7.1.0

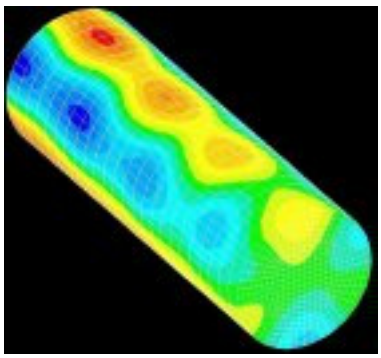

39. Frequency 379.2 Hz, Shape 0.3.0

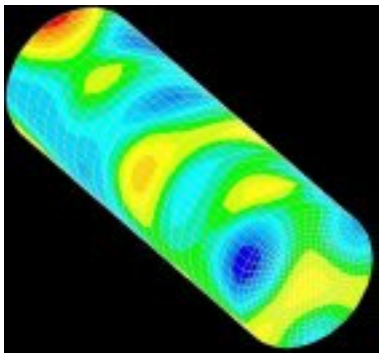

40. Frequency 386.0 Hz

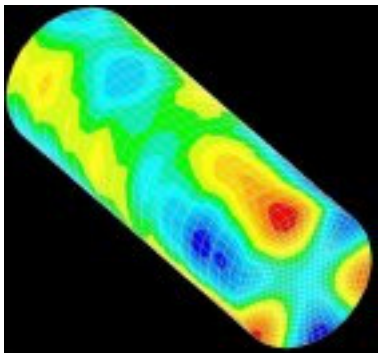

41. Frequency 390.0 Hz, Shape 1.3.0

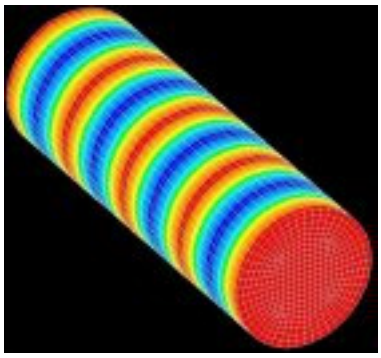

42. Frequency 392.4 Hz, Shape 8.0.0

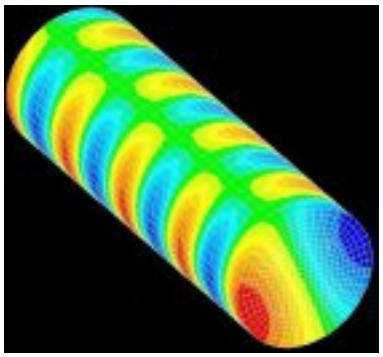

43. Frequency 425.8 Hz, Shape 8.1.0

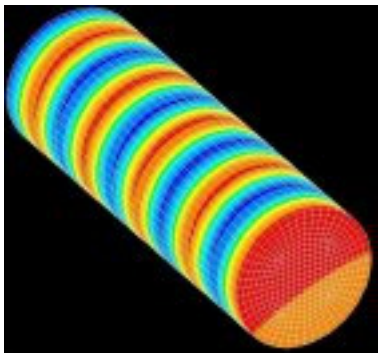

44. Frequency 446.8 Hz, Shape 9.0.0

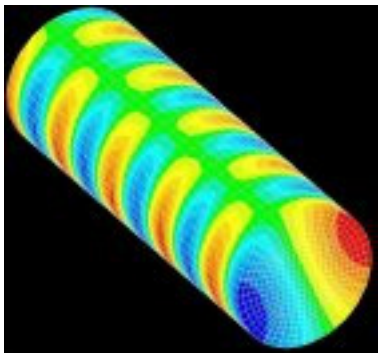

45. Frequency 476.2 Hz, Shape 9.1.0

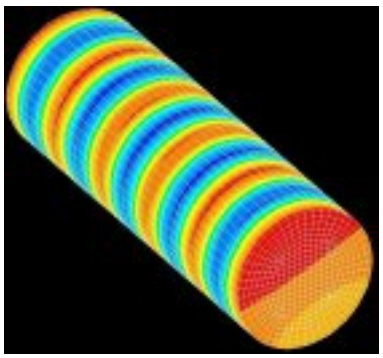

46. Frequency 503.1 Hz, Shape 10.0.0

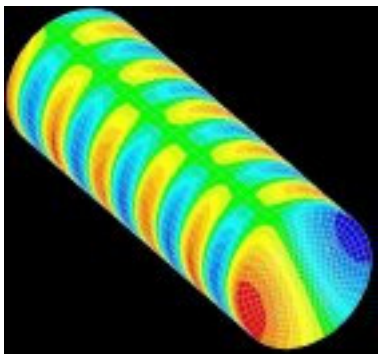

47. Frequency 529.2 Hz, Shape 10.1.0

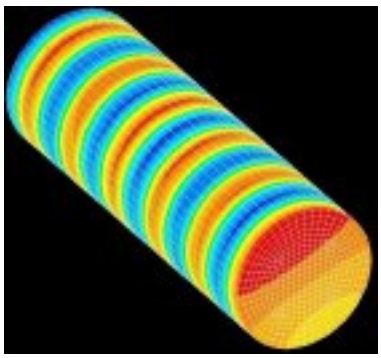

48. Frequency 561.5 Hz, Shape 11.0.0

Figure 30 (continued). ATC acoustic mode numbers, modal frequencies and mode shapes.

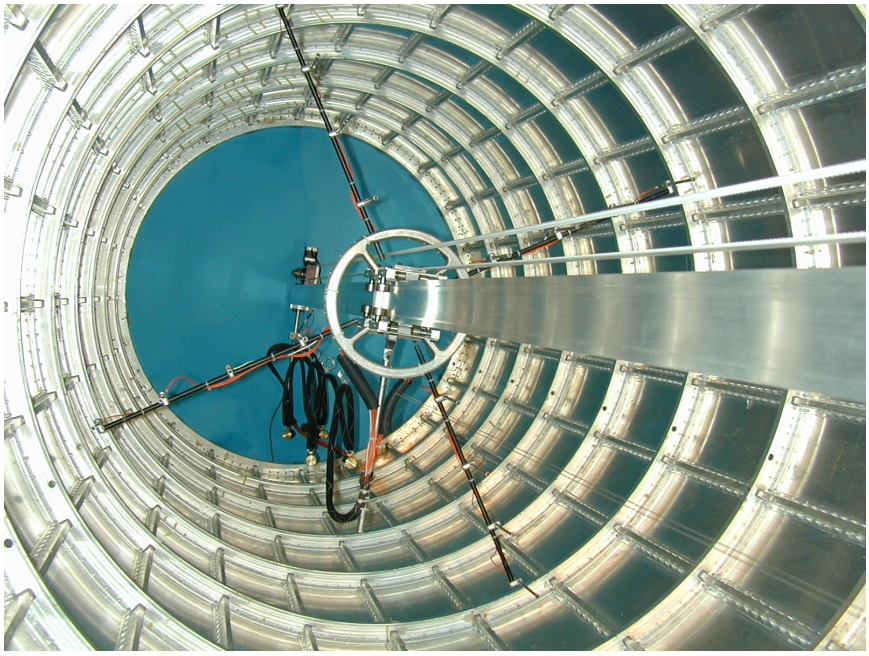

Figure 31. Interior view of ATC showing 16-microphone array mounted on traverse mechanism.

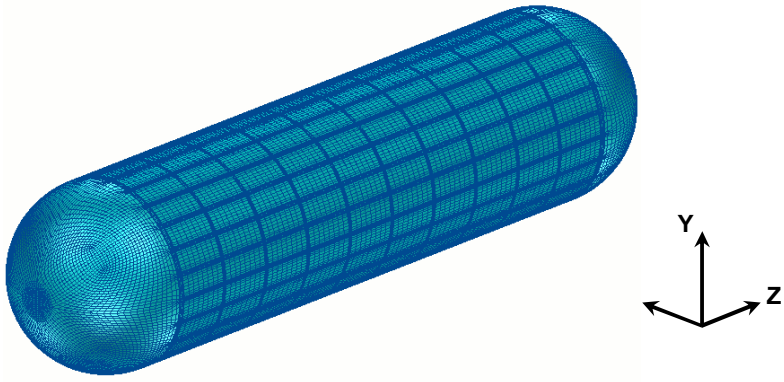

Figure 32. Structural Finite Element (FE) model ATC configuration V.

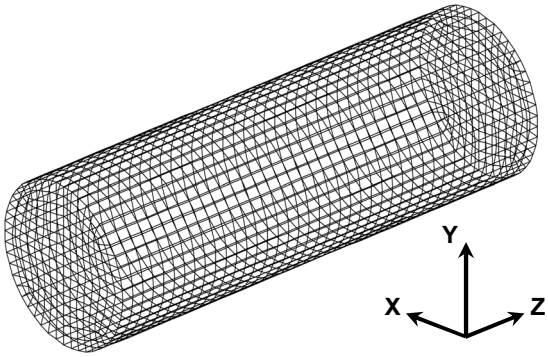

Figure 33. Acoustic Boundary Element (BE) model.

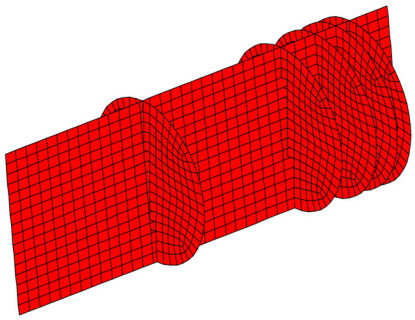

Figure 34. Data Recovery Mesh (DRM).

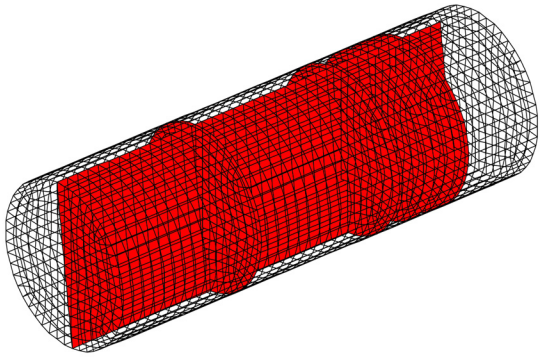

Figure 35. DRM inside the acoustic BE model.

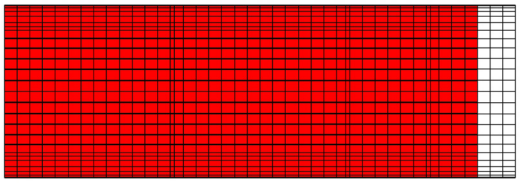

Figure 36. Side view of the DRM inside the acoustic BE model.

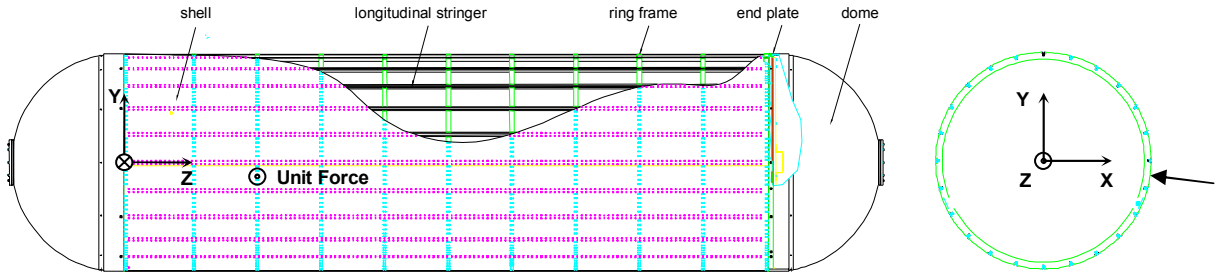

Figure 37. Unit force applied to the ATC configuration V frame at z-coordinate 28.8 inches at a 7.5 degrees angle with the x-axis.

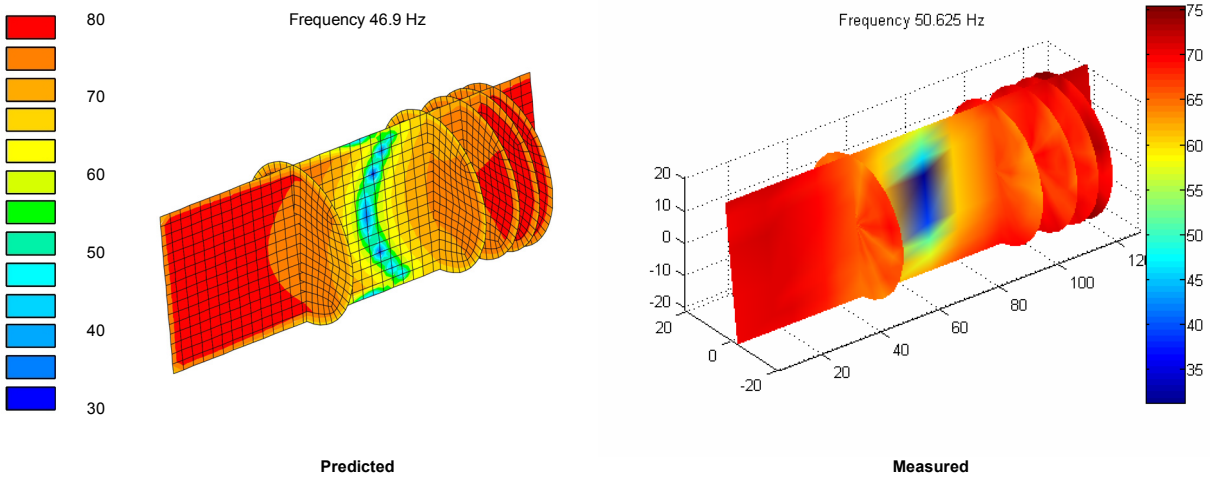

Figure 38. Interior acoustic response due to unit force applied at the (1,0,0) acoustic modal frequency.

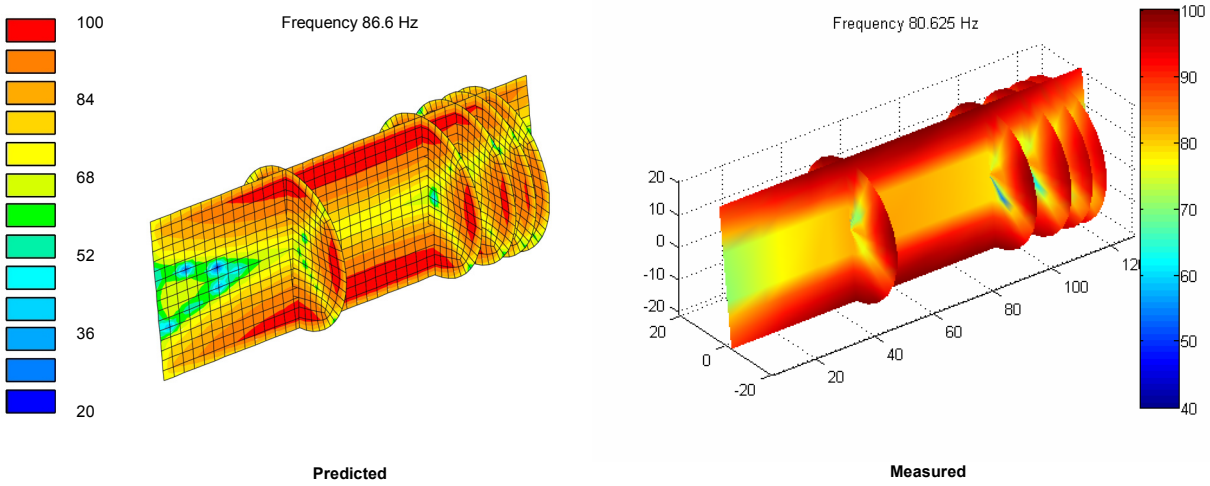

Figure 39. Interior acoustic response due to unit force applied at the (2,1) structural modal frequency.

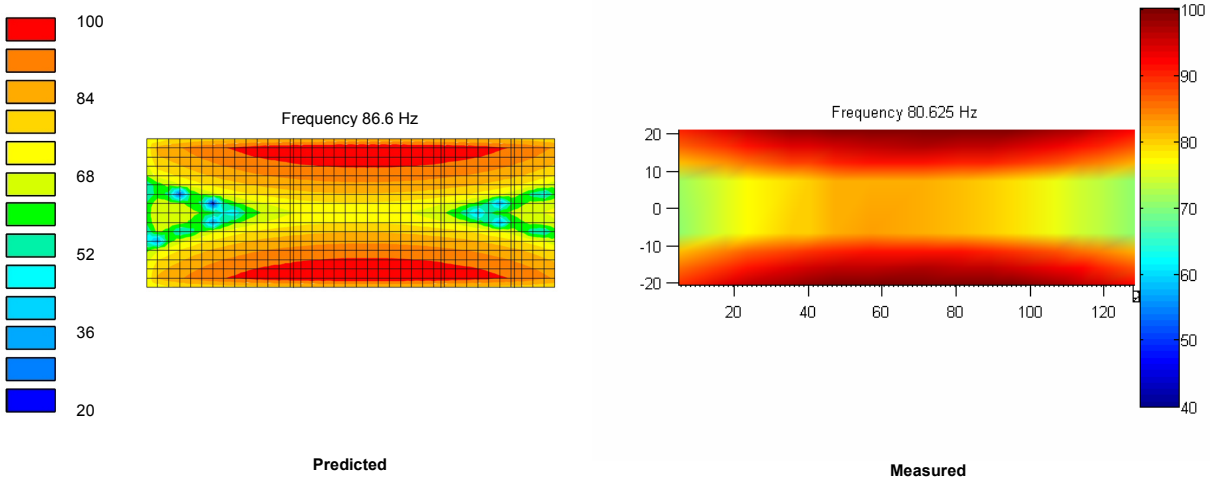

Figure 40. Interior acoustic response due to unit force applied at the (2,1) structural modal frequency (side view).

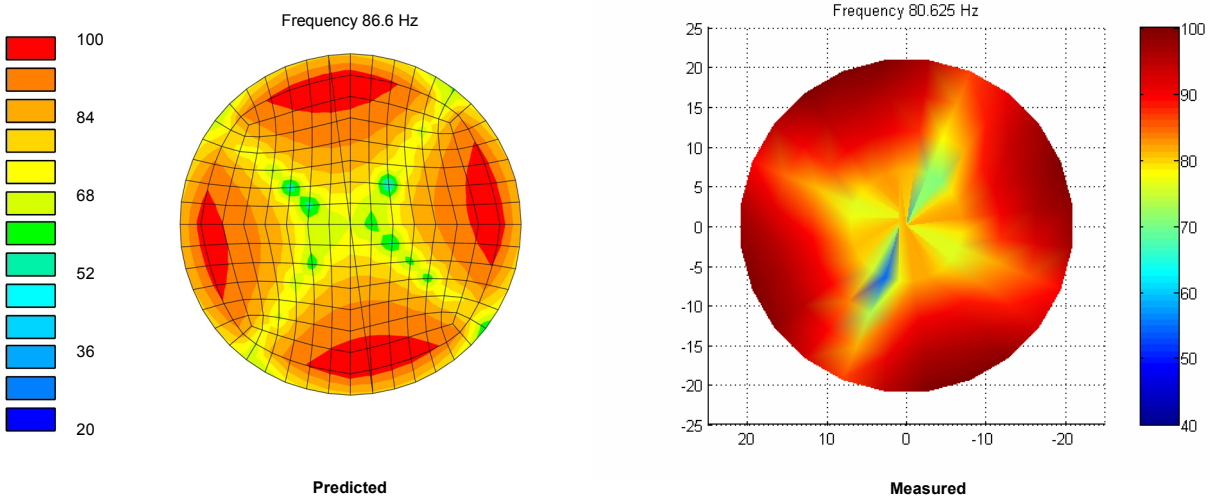

Figure 41. Interior acoustic response due to unit force applied at the (2,1) structural modal frequency (rear view).

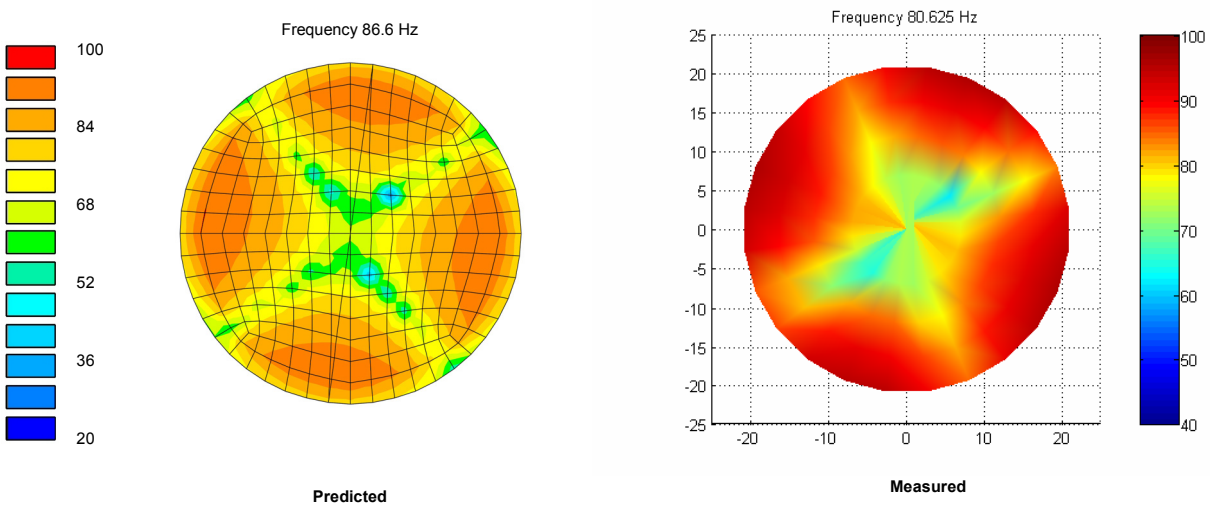

Figure 42. Interior acoustic response due to unit force applied at the (2,1) structural modal frequency (front view).

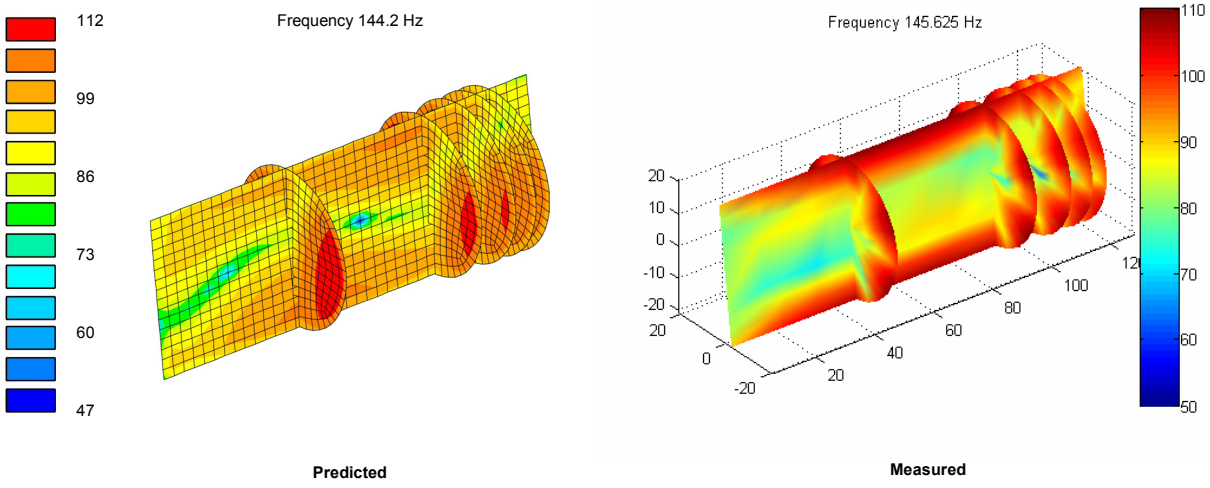

Figure 43. Interior acoustic response due to unit force applied at the (3,1) structural modal frequency.

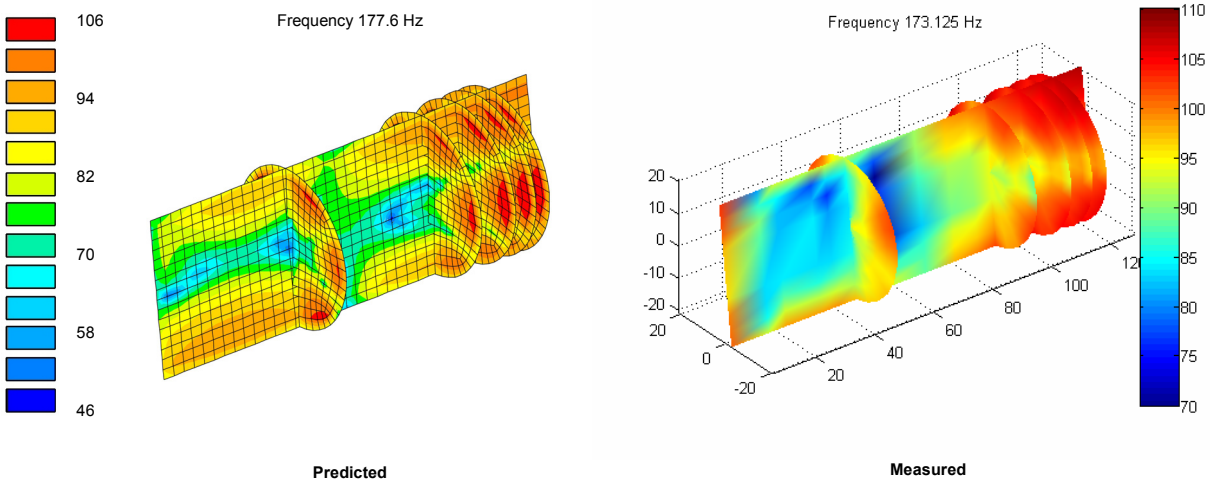

Figure 44. Interior acoustic response due to unit force applied at the (3,2) structural modal frequency.

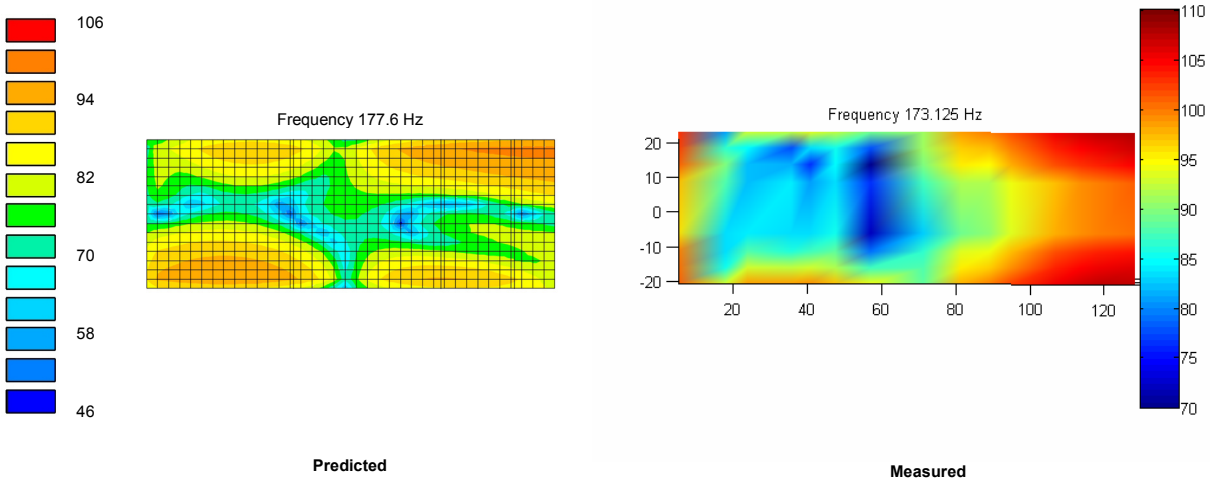

Figure 45. Interior acoustic response due to unit force applied at the (3,2) structural modal frequency (side view).

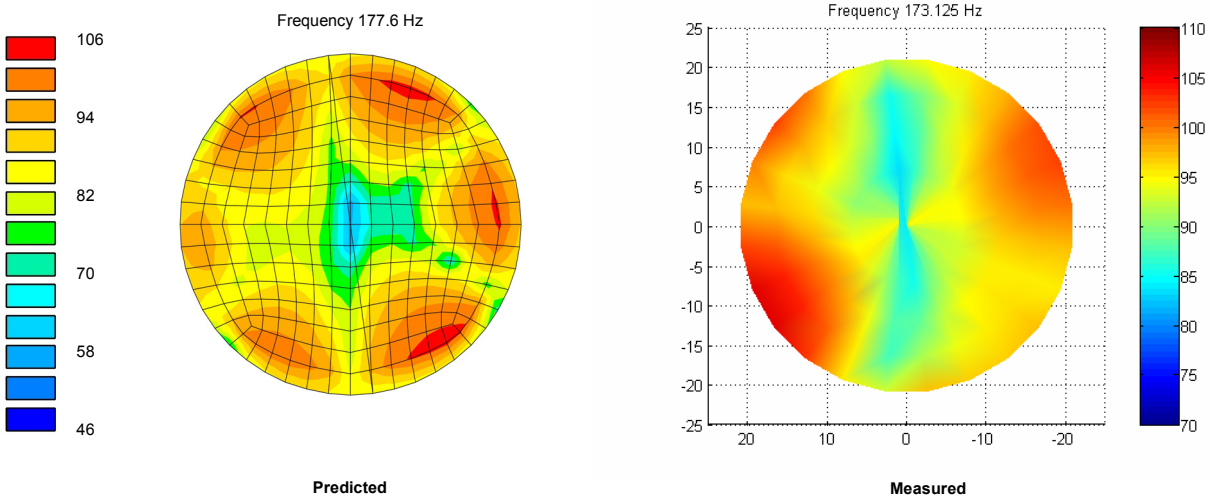

Figure 46. Interior acoustic response due to unit force applied at the (3,2) structural modal frequency (rear view).

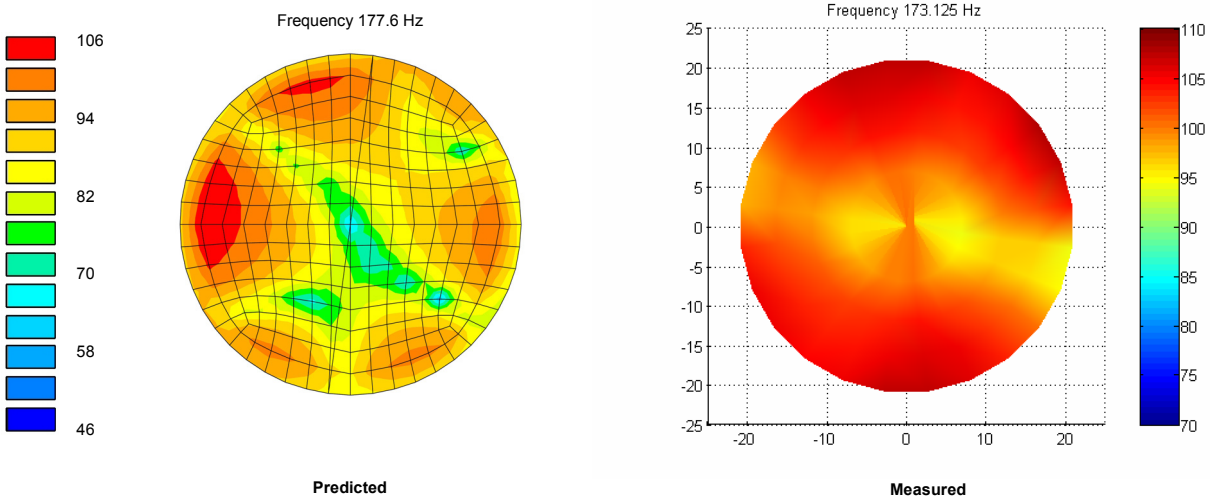

Figure 47. Interior acoustic response due to unit force applied at the (3,2) structural modal frequency (front view).

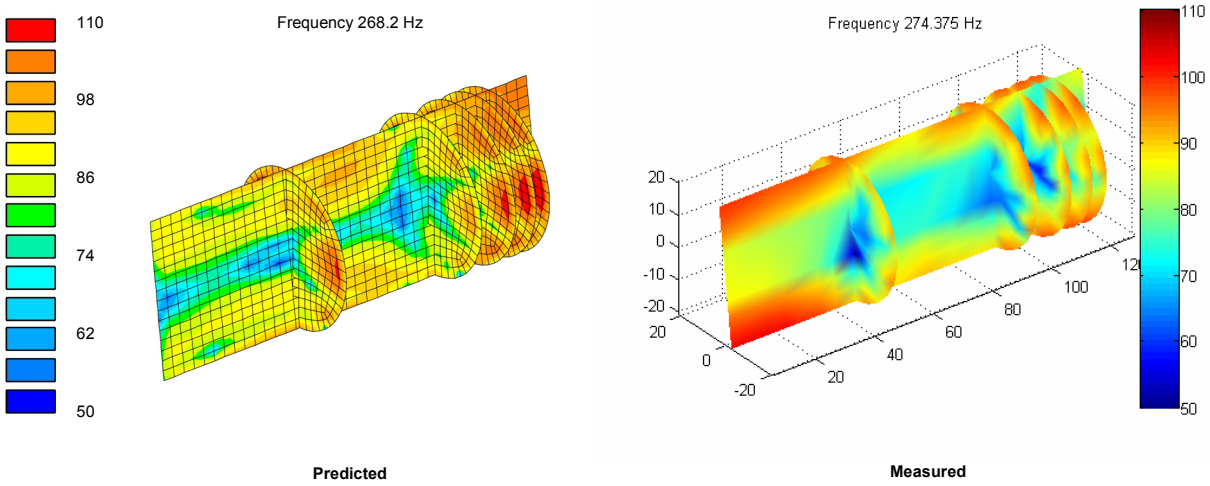

Figure 48. Interior acoustic response due to unit force applied at the (4,2) structural modal frequency.

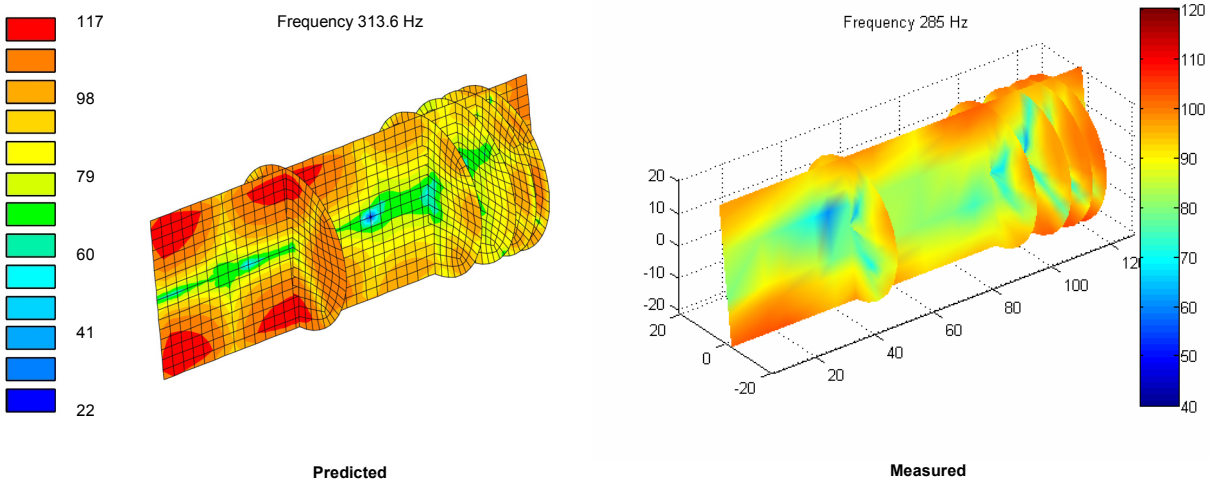

Figure 49. Interior acoustic response due to unit force applied at the (3,4) structural modal frequency.

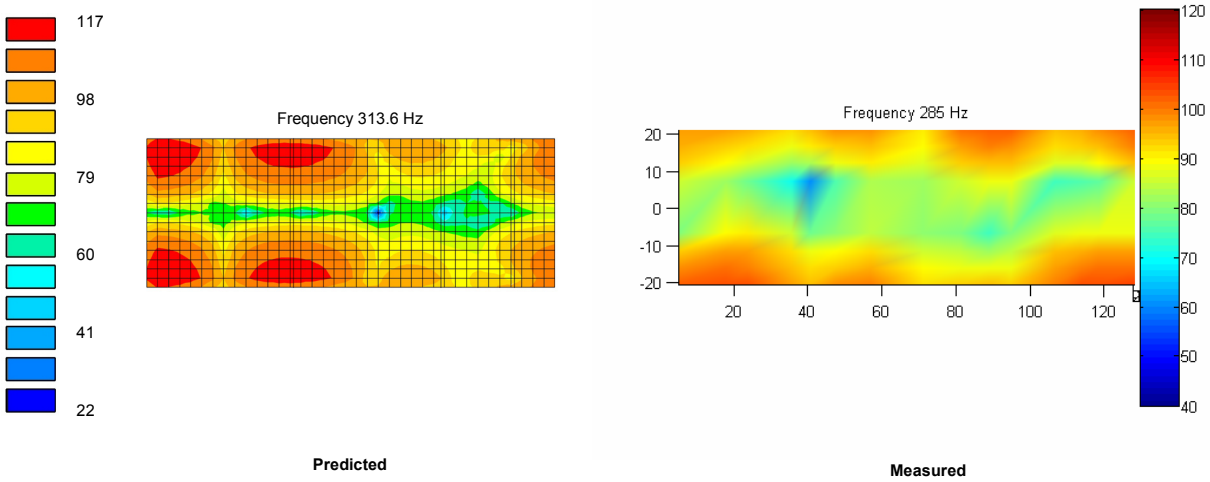

Figure 50. Interior acoustic response due to unit force applied at the (3,4) structural modal frequency (side view).

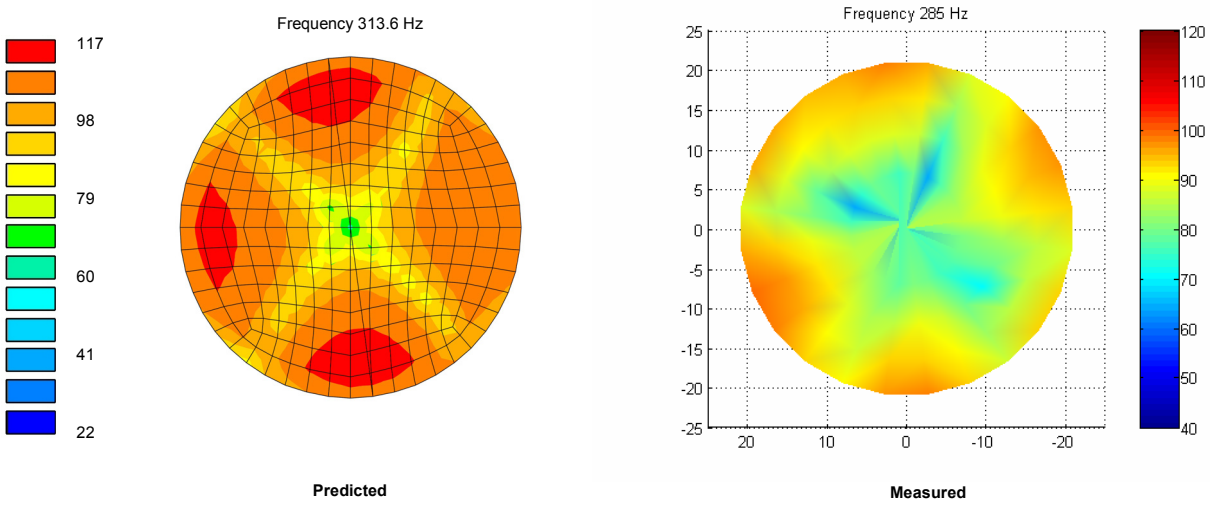

Figure 51. Interior acoustic response due to unit force applied at the (3,4) structural modal frequency (rear view).

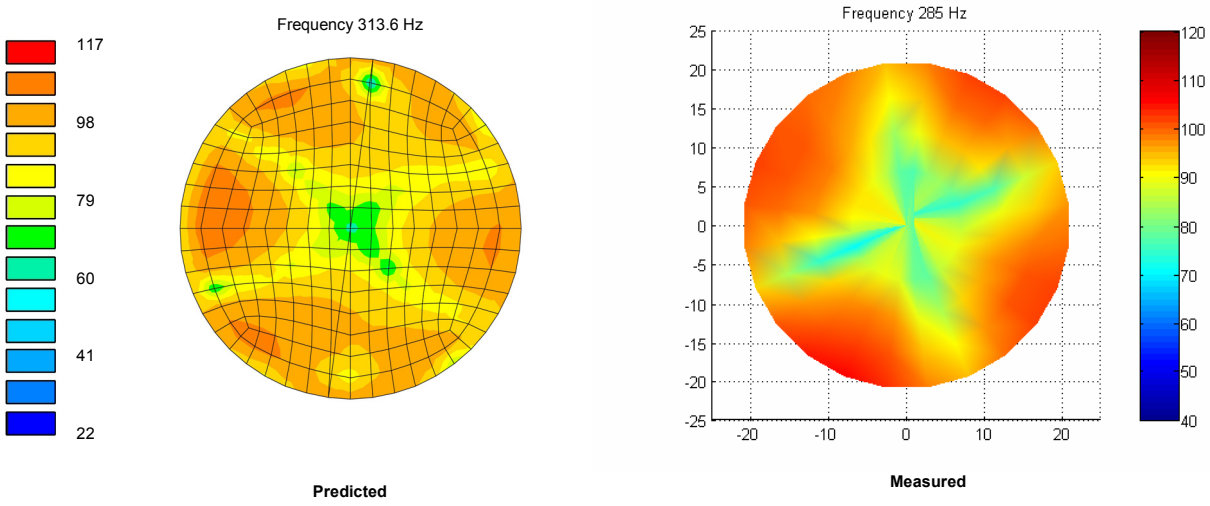

Figure 52. Interior acoustic response due to unit force applied at the (3,4) structural modal frequency (front view).

REPORT DOCUMENTATION PAGE

Form Approved
OMB No. 0704-0188

1. REPORT DATE *(DD-MM-YYYY)*	2. REPORT TYPE	3. DATES COVERED *(From - To)*
01- 03 - 2006	Contractor Report	

4. TITLE AND SUBTITLE

Finite and Boundary Element Modeling of the NASA Langley Aluminum Testbed Cylinder (ATC)

5a. CONTRACT NUMBER

NAS1-00135B

5b. GRANT NUMBER

5c. PROGRAM ELEMENT NUMBER

6. AUTHOR(S)

Grosveld, Ferdinand W.

5d. PROJECT NUMBER

5e. TASK NUMBER

5f. WORK UNIT NUMBER

23-781-10-13

7. PERFORMING ORGANIZATION NAME(S) AND ADDRESS(ES)

NASA Langley Research Center
Hampton, VA 23681-2199

Lockheed Martin Engineering and Sciences
NASA Langley Research Center
Hampton, VA 23681-2199

8. PERFORMING ORGANIZATION REPORT NUMBER

9. SPONSORING/MONITORING AGENCY NAME(S) AND ADDRESS(ES)

National Aeronautics and Space Administration
Washington, DC 20546-0001

10. SPONSOR/MONITOR'S ACRONYM(S)

NASA

11. SPONSOR/MONITOR'S REPORT NUMBER(S)

NASA/CR-2006-214283

12. DISTRIBUTION/AVAILABILITY STATEMENT

Unclassified - Unlimited
Subject Category 71
Availability: NASA CASI (301) 621-0390

13. SUPPLEMENTARY NOTES

Langley Technical Monitor: Richard J. Silcox
An electronic version can be found at http://ntrs.nasa.gov

14. ABSTRACT

The NASA Langley Aluminum Testbed Cylinder (ATC) was designed to serve as a universal structure for evaluating structural acoustic codes, modeling techniques and optimization methods used in the prediction of aircraft interior noise. Finite element models were developed for the components of the ATC based on the geometric, structural and material properties of the physical test structure. Numerically predicted modal frequencies for the longitudinal stringer, ring frame and dome component models, and six assembled ATC arrangements were in good agreement with experimental modal survey data. Finite element modal analyses were performed for 3 psi and 6 psi internal pressurization conditions. Acoustic cylinder modes for the interior of the ATC were calculated with an acoustic finite element model. Frequency transfer functions between a unit force on the structure and the acoustic response inside the ATC cylinder were measured and were compared with predictions based on a boundary element model. Comparisons between predicted and experimental results are presented and discussed.

15. SUBJECT TERMS

Aluminum Testbed Cylinder; Structural Acoustics; Interior Noise Prediction; Finite Element Modeling; Boundary Element Modeling

16. SECURITY CLASSIFICATION OF:			17. LIMITATION OF ABSTRACT	18. NUMBER OF PAGES	19a. NAME OF RESPONSIBLE PERSON
a. REPORT	b. ABSTRACT	c. THIS PAGE			STI Help Desk (email: help@sti.nasa.gov)
					19b. TELEPHONE NUMBER *(Include area code)*
U	U	U	UU	77	(301) 621-0390